

**Evaluation of X-Ray Computed Tomography and Finite Element
Models for Fatigue Experimental Hot Mix Asphalt
Characterization**

by

Magdy Shaheen

A thesis
presented to the University of Waterloo
in fulfillment of the
thesis requirement for the degree of
Doctor of Philosophy
in
Civil Engineering

Waterloo, Ontario, Canada, 2015

© Magdy Shaheen 2015

AUTHOR'S DECLARATION

I hereby declare that I am the sole author of this thesis. This is a true copy of the thesis, including any required final revisions, as accepted by my examiners.

I understand that my thesis may be made electronically available to the public.

Abstract

Fatigue cracking is one of the major distresses of surface hot mix asphalt (HMA) pavement that shorten pavement service life. Under typical Canadian weather conditions, fatigue distress requires frequent and high-cost maintenance and is therefore always a key concern for pavement construction and design engineers. The primary focus of this thesis was the development of an advanced understanding of the mechanisms underlying fatigue resistance in surface HMA materials. The research objectives have been achieved through extensive experimental evaluation, advanced image-based characterization techniques, and three-dimensional (3D) image-based microstructural finite element (FE) modelling. The findings of this study can therefore be considered a guide for the development of HMA that exhibits superior fatigue performance for use in pavement designs that might lead to longer-lasting pavements and enhanced performance.

The experimental work involved an evaluation of the sensitivity of the fatigue resistance of surface HMA mixes to three primary design variables. Aggregate type, binder type, and binder content as well as their interaction have been quantified with respect to their effects on HMA fatigue life, rutting resistance, and stiffness. The objective was to optimize the design by extending fatigue performance while reducing the confounded negative effect on rutting resistance. Two aggregate types were used in the evaluation: Superpave SP12.5 and high friction SP12.5FC2. Two performance graded binders (PG 64-28) were also employed: a modified binder (PG Plus) that meets Ontario Laboratory Standards (LS) specifications and an unmodified binder at two binder levels (optimum and optimum plus 0.5 %). The results show that when a high friction aggregate is used, the value of modifying the binder to produce softer mixes can be compromised due to the irregular shape associated with the texture, which produces stiffer mixes. A slight adjustment to the amount of binder (+ 0.5%) can decrease this effect. Superior HMA fatigue performance was exhibited by the regular 12.5 aggregate and the PG Plus at the optimum binder content plus the additional 0.5 %. This conclusion was reached through the integration of the positive effects of the variables investigated.

The experimental findings also revealed only an insignificant reversible impact on rutting resistance. A high friction aggregate provided a better internal structural characteristic as well as superior rutting resistance and stiffness in the HMA mixes. The use of PG Plus and the addition of 0.5% to the optimum binder content negatively affected HMA stiffness and rutting resistance. However, the levels of rutting resistance for all mixes were acceptable (rut depth < 12.5 mm), even when shear upheave was considered.

Three imaging techniques were utilized for an advanced image-based investigation of HMA characteristics and performance: scanning electron microscopy (SEM), a combination of a simple scanner and Ipas2 software to depict the two-dimensional (2D) internal structure of the test specimens, and nondestructive X-ray computed tomography (CT) for 3D analysis. Aggregate texture was compared using 3D visualization of the SEM images, a technique that provides very high resolution. The rutting resistance of the HMA mixes was investigated using 2D images of the experimentally tested specimens, which involved estimating the number of aggregate contacts, the total contact length, and the Internal Structure Index (ISI). The ISIs measured were effective for capturing changes in the internal HMA structure with respect to aggregate type and asphalt cement content.

A framework was established for employing X-ray CT for the assessment of HMA fatigue damage. The analyses were carried out on asphalt beams in order to quantify the damage created by four-point bending loads. A new algorithm was developed for calculating the thresholding levels of the images acquired before and after testing. The thresholding levels prior to testing were estimated using laboratory air voids. To determine the post-testing thresholding levels, the proposed algorithm matches 16-bit image histograms obtained before and after the testing. This process is implemented only for the portion of the histogram that represents the aggregate colour intensities that remain unchanged during the testing. The results and analysis reveal that the developed technique is a valid method for successfully quantifying and evaluating HMA fatigue damage in large specimens. Because of the high degree of precision they provide, 16-bit images are recommended for this type of analysis. It was found that the distribution of both air voids and damage is non-uniform in asphalt beams and that it varies significantly throughout the length of a single beam as well as from beam to

beam. This study also confirms the effectiveness of X-ray CT for quantifying HMA fatigue damage in asphalt beams following crack propagation.

A microstructural FE model based on 3D X-ray CT images was developed as a means of investigating the effect of asphalt mixture constituents on mechanical responses. The model takes into account the complex 3D geometry, spatial distribution, volume fraction, and mechanical behaviour of each individual component of the asphalt mixture. Three mixture components were modelled: the aggregate, the fine aggregate asphalt matrix (FAM), and the air voids. The primary objective of developing this model was to quantify and enable the visualization of the effect of air voids and the aggregate modulus on the FAM phase, which is the domain in which fatigue cracking initiates and propagates. The results demonstrate that air void distribution and the aggregate modulus have a strong impact on local stress concentrations that occur in the FAM domain. The developed 3D microstructural model has notable potential to enhance HMA design methods.

Acknowledgements

I would like to express deep gratitude to my supervisor, Professor Susan Tighe, as well as my co-supervisor, Professor Adil Al-Mayah, for their guidance, encouragement, and investment in my career. Without their continual support and advice, I would not have had the opportunity to publish and present my work in several professional journals and scientific conferences. I would also like to thank my committee members.

I greatly appreciate the support of the Ministry of Transportation of Ontario in particular, Warren Y. Lee and Imran Basher for funding of this study through the Highway Infrastructure Innovation Funding Program.

I would like to thank the companies that have supplied the materials used in this research, specifically K. J. Beamish Construction and the Dufferin Construction Company.

Thanks are due to the technicians in the Department of Civil and Environmental Engineering at the University of Waterloo for their assistance with the experimental setup: Richard Morrison, Terry Ridgway, Robert Sluban, and Douglas Hirst.

I gratefully acknowledge the help of numerous partners at the Centre for Pavement and Transportation Technology and of those associated with the Norman W. McLeod Chair.

I would like to extend my gratitude to my CPATT colleagues and co-op students who assisted me with the laboratory work for this study. Special thanks go to my friends Amr Said, Amin Hamdi, Doubra Ambaiowei, Laura Bland, Xiomara Sanchez, Marcelo González, and Mohab El- Hakim for their constructive discussions.

Finally, I would like to acknowledge the contribution of the University of Wisconsin Madison, the Modified Asphalt Research Center (MARC), and Professor Emin Kutay for providing the image analysis software used in this research.

Dedication

I wish to dedicate my thesis to my family. I feel special gratitude for all the care and encouragement I have received from my loving mother and father, Neama and Mohamed, who taught me the value of education. I thank my dear sons, Ahmed and Mohamed, for giving me the motivation and inspiration I needed to complete my studies. In appreciation of their endless support, I also extend this dedication to my sisters, brothers, friends, and colleagues.

Table of Contents

AUTHOR'S DECLARATION.....	ii
Abstract.....	iii
Acknowledgements.....	vi
Table of Contents.....	viii
List of Figures.....	xii
List of Tables.....	xv
List of Abbreviations.....	xvi
Chapter 1 Introduction.....	1
1.1 Background.....	2
1.2 Research Objectives.....	4
1.3 Research Hypothesis.....	5
1.4 Research Methodology.....	5
1.5 Organization of the Thesis.....	6
Chapter 2 Literature Review.....	8
2.1 HMA Performance and Experimental Evaluation.....	8
2.1.1 General Overview.....	8
2.1.2 HMA Fatigue Cracking.....	9
2.1.2.1 Experimental Techniques for Determining HMA Fatigue Life.....	10
2.1.3 Dynamic Modulus of HMA.....	11
2.1.4 HMA Rutting.....	12
2.1.5 Effect of HMA Design Variables on Performance.....	14
2.2 Image-Based Analysis.....	16
2.2.1 X-Ray Computed Tomography.....	18
2.2.2 Applicability of X-Ray CT for HMA Characterization.....	19
2.3 Microstructure Finite Element Modelling.....	21
2.3.1 HMA Mechanistic Behaviour.....	22
2.3.1.1 Conversion Material Characterization.....	25
2.3.1.2 Fine Aggregate Matrix Design.....	26
2.3.2 Microstructural FE Modelling Techniques and Findings.....	26
2.4 Summary.....	29
Chapter 3 Research Methodology, Materials, and Testing.....	32

3.1 Research Plan	32
3.2 Task 1 – Literature Review	32
3.3 Task 2 – Design of HMA Laboratory Mixes.....	32
3.4 Task 3 – Testing of HMA Mixes.....	37
3.4.1 Flexural Beam Fatigue Test.....	37
3.4.2 Dynamic Modulus Test	39
3.4.3 Hamburg Wheel Rutting Tester (HWRT)	41
3.4.4 Flow Number Test (FN).....	41
3.4.5 Quantifying HMA Shear Flow	42
3.5 Task 4 – Image Acquisition.....	43
3.5.1 Scanning Electron Microscopy (SEM).....	44
3.5.2 2D Internal Structural Analysis.....	44
3.5.3 X-Ray CT System and Imaging	45
3.6 Task 5 – Development of Image-Based Analysis Frameworks.....	46
3.7 Task 6 – Microstructural Finite Element Model	47
3.8 Task 7 – Conclusions and Recommendations	47
Chapter 4 Optimization of HMA Design for Fatigue Performance	48
4.1 Asphalt Binder Stiffness.....	48
4.2 HMA Fatigue Life Comparison.....	51
4.3 Reverse Impact Analysis	55
4.3.1 HMA Mix Stiffness	55
4.3.2 HMA Mix Rutting Resistance	62
4.3.3 Comparison of Flow Numbers (FN).....	66
4.4 Summary and Conclusions	69
Chapter 5 Development of HMA Image-Based Analysis Frameworks	70
5.1 Demonstration of Aggregate Texture using SEM	70
5.2 2D Imaging Analysis Framework for the Mixtures Tested	71
5.2.1 Sample Preparation.....	73
5.2.2 Image Acquisition and Quality.....	73
5.2.3 Image Processing and Analysis.....	73
5.3 Establishment of Framework to Quantify Fatigue Damage	75
5.3.1 Thresholding for Air Voids and Damage	75

5.3.2 Development of the Analysis Algorithm	76
5.3.3 Scanning and Analysis Framework.....	77
5.4 Summary and Conclusions.....	82
Chapter 6 Image-Based HMA Characterization Results and Discussion	83
6.1 Comparison of Aggregate Texture.....	83
6.2 2D Internal structure analysis of HMA.....	86
6.3 HMA Fatigue Damage	88
6.4 Validation of the Proposed Framework	88
6.5 Case Studies	93
6.5.1 Fatigue test results.....	94
6.5.2 Air void distribution.....	96
6.5.3 Damage characterization.....	97
6.5.4 Crack Detection	100
6.6 Summary and Conclusion	103
Chapter 7 Microstructural Finite Element Modelling of HMA	104
7.1 Components of the HMA Microstructure	104
7.2 Extraction of the Aggregate from the Images.....	104
7.3 Building a Three-Dimensional Microstructural Model.....	107
7.3.1 Phase 1: Identification of Microstructural Components	107
7.3.2 Phase 2: Finite Element Mesh and Boundary Conditions.....	109
7.3.3 Phase 3: Constitutive Model and Material Parameters	109
7.4 Microstructural FE Model Results and Discussion.....	112
7.4.1 Stress and Strain Distributions.....	112
7.4.2 Effect of the Aggregate Elastic Modulus on the Response of the Mixture.....	113
7.4.3 Effect of Air Voids on the Asphalt Mixture.....	116
7.4.4 Effect of Air Voids on the FAM	118
7.5 Summary and Conclusion	121
Chapter 8 Conclusions and Recommendations.....	122
8.1 Conclusions.....	122
8.1.1 Experimental Work	122
8.1.2 Image-Based Analysis.....	124
8.1.3 Microstructural FE Modelling Based on Three-Dimensional X-ray CT Imaging	125

8.2 Advanced Understanding of the HMA Fatigue Mechanism	126
8.2.1 Experimental fatigue life	127
8.2.2 Image-based analysis.....	127
8.2.3 Microstructural FE Modelling.....	128
8.3 Future Work	129
Publications	130
References	131
Appendix A : Experimental Work.....	142
Appendix B : Image-Based Analysis	150
Appendix C : Microstructural FE Modeling	156

List of Figures

Figure 1-1 Variables that affect hot mix asphalt characterization, performance, and design	3
Figure 2-1 Typical fatigue cracking in asphalt pavement	9
Figure 2-2 Typical viscoelastic response of an asphalt mixture (Clyne et al. 2003)	12
Figure 2-3 Rutting in asphalt pavement	13
Figure 2-4 Matrix representation of an $M \times N$ binary image (Cannone Falchetto et al. 2012)	16
Figure 2-5 3D CT image analysis technique (Aragao 2011; Masad et al. 2005; You et al.)	18
Figure 2-6 Stacked X-ray CT images (Dai 2011)	19
Figure 2-7 Mechanical models (a) Maxwell, (b) Kelvin-Voigt, and (c) Burger (Breakah 2009)	23
Figure 2-8 Typical strain versus time relationship for asphalt (Breakah 2009; Lytton et al. 1993)	24
Figure 2-9 Diagram of the traction-separation law (Elseifi et al. 2012)	28
Figure 3-1 Outline of the research methodology	33
Figure 3-2 Aggregate gradations	35
Figure 3-3 Saw cutting of fatigue asphalt beams	38
Figure 3-4 Temperature controlled CPATT flexural beam test setup	39
Figure 3-5 Coring and cutting procedures for the compacted specimen	40
Figure 3-6 CPATT dynamic modulus test setup	40
Figure 3-7 CPATT Hamburg wheel rut tester (HWRT)	41
Figure 3-8 Flow number test setup	42
Figure 3-9 Field and laboratory measurements of HMA rutting depth: (a) total rut depth measured with a rut bar; (b) field measurement of rut depth; (c) transverse surface profile for quantifying shear upheave	43
Figure 3-10 SEM test setup	45
Figure 3-11 CT scanning system and test setup	46
Figure 4-1 Master curves for asphalt binder stiffness (G^*)	49
Figure 4-2 Effects of modification on binder stiffness: (a) at intermediate temperatures; (b) at high temperatures	50
Figure 4-3 Fatigue life and PV values of the HMA mixes	52
Figure 4-4 Master curves for the HMA mixes at 21 °C	56
Figure 4-5 Sensitivity analysis of E^* changes: (a) effect of aggregate type; (b) effect of binder type; (c) effect of binder content	58
Figure 4-6 Dynamic moduli of the HMA mixes at 54 °C for different frequencies	59

Figure 4-7 Relationships between the dynamic moduli of the HMA mixes at 54 °C and a variety of frequencies: (a) effect of aggregate type; (b) effect of binder type; (c) effect of binder content	61
Figure 4-8 HWRT rut depth versus number of load passes	62
Figure 4-9 Rutting depths and rates for the HMA mixes	64
Figure 4-10 Accumulated permanent strain and rates of slope change: (a) SP12.5 FC2 PG 64-28; (b) SP 12.5 PG 64-28	67
Figure 4-11 Boxplot for HMA mix flow numbers	68
Figure 5-1 Illustrations of aggregate texture: (a) shape characteristics (Masad 2007); (b) regular amplitude; (c) irregular amplitude.....	71
Figure 5-2 Aggregate texture for areas 2.3 mm wide (magnification = 50 X): (a) 4.75 mm 12.5FC2 aggregate; (b) 4.75 mm 12.5 aggregate; (c) 2.36 mm 12.5FC2 aggregate; (d) 2.36 mm 12.5 aggregate	72
Figure 5-3 Image preparation and processing methodology	74
Figure 5-4 HMA image histogram of the test sample at middle section	75
Figure 5-5 Image histograms: (a) 8 bit images, (b) 16 bit images.....	77
Figure 5-6 Scanning process and analysis framework	79
Figure 5-7 Matching of two histograms: (a) two histograms before matching; (b) matched parts; (c) error in the matching of the two histograms.....	81
Figure 6-1 Three-dimensional visualization of aggregate texture for 114.4 μm wide samples (magnification = 1000 X).....	84
Figure 6-2 Three-dimensional visualization of aggregate texture for 114.4 μm wide samples (magnification = 1000 X).....	85
Figure 6-3 Number of contacts between aggregate particles in HMA mixes.....	87
Figure 6-4 3D views of 90 mm of an asphalt beam: (a) 3D microstructure (b) 3D air void distribution	89
Figure 6-5 Image histograms of four scans for the same specimen	90
Figure 6-6 Air voids in a sample image slice	90
Figure 6-7 Air void distributions for four scans of the same specimen.....	91
Figure 6-8 3D visualization of air void distributions for the same specimen: (a) Scan 1; (b) Scan 2; (c) Scan 3; (d) Scan 4.....	92
Figure 6-9 Changes in the 3D void distributions for the four scans.....	93
Figure 6-10 Typical reduction in flexural stiffness in asphalt mixtures.....	94

Figure 6-11 S-N curves for four asphalt beams	95
Figure 6-12 Air void distribution in 240 mm length of each asphalt beam	96
Figure 6-13 Air void distributions before and after the fatigue test.....	98
Figure 6-14 Average level of damage in the beams tested	100
Figure 6-15 Effect of the fatigue test on void size distribution: (a) Beam 1; (b) Beam 2; (c) Beam 3; (d) Beam 4	101
Figure 6-16 3D visualization of a HMA crack.....	102
Figure 6-17 2D slices of crack region in asphalt beam.....	102
Figure 7-1 Images of an HMA mixture obtained using X-ray CT: (a) 3D; (b) 2D slice	105
Figure 7-2 Illustration of the steps for extracting aggregate images.....	106
Figure 7-3 3D digital images: (a) aggregate; (b) mixture	107
Figure 7-4 3D visuals of the aggregate sizes in the asphalt beam: (a) > 12.5 mm; (b) 12.5 mm to > 9.5 mm; (c) 9.5 mm to >4.75 mm; (d) 4.75 mm to > 2.36 mm.....	108
Figure 7-5 3D images of the asphalt mixture microstructure: (a) mixture; (b) aggregate; (c) FAM; (d) air voids; (e) FAM without air voids; (f) aggregate and air voids	110
Figure 7-6 Images of the FE model mesh: (a) mixture; (b) aggregate; (c) FAM; (d) FAM cross section	111
Figure 7-7 3D Microstructural response: (a) stress on the aggregate; (b) stress on the FAM; (c) strain on the aggregate; (d) strain on the FAM.....	114
Figure 7-8 Effect of the aggregate elastic modulus on asphalt mixture response.....	115
Figure 7-9 Effect of air voids on the asphalt mixture response: (a) no air voids; (b) 7 % air voids ..	117
Figure 7-10 Effect of air voids on the asphalt mixtures responses: (a) strain in compression; (b) stress in compression	118
Figure 7-11 Effect of air voids on FAM responses: (a) no air voids; (b) air voids.....	119
Figure 7-12 Effect of air voids on the FAM stress: (a) without air voids; (b) with air voids	120

List of Tables

Table 2-1 Description of Numerical Models Developed for the Prediction of HMA Characterization	30
Table 3-1 Aggregate Consensus Properties.....	35
Table 3-2 Binder Properties.....	36
Table 3-3 Volumetric Properties of HMA Mixes at Optimum Binder Content	36
Table 3-4 Laboratory Mix Matrix	37
Table 4-1 Analysis of Variance Fatigue Life Results at N_{f50} on a Log Scale.....	53
Table 4-2 Analysis of Variance for the PV on a Log Scale	53
Table 4-3 Analysis of Variance for E^* at 54 °C and 1 Hz.....	59
Table 4-4 ANOVA Statistical Analysis of HWRT Results.....	63
Table 4-5 Analysis of Variance for HWRT Rut Depth.....	65
Table 4-6 Analysis of Variance for Rutting Rate.....	65
Table 4-7 Grouping Information for the Fisher Method Analysis	66
Table 6-1 Analysis of Variance for Number of Contacts.....	87
Table 6-2 Validation of Analysis	90
Table 6-3 Test Beam Details	94
Table 7-1 Prony Series for the Generalized Maxwell Model (Coleri et al. 2012).....	112

List of Abbreviations

2D	Two Dimensional
3D	Three Dimensional
AASHTO	American Association of State Highway Transportation Officials
CT	Computed Tomography
E*	Dynamic Modulus
FAM	Fine Aggregate Asphalt Matrix
FE	Finite Element
FN	Flow Number
G*	Complex Shear Modulus
HMA	Hot Mix Asphalt
HWRT	Hamburg Wheel Rut Tester
ISI	Internal Structure Index
LS	MTO Laboratory Testing Manual
PG	Performance Graded
PV	Plateau Value
SEM	Scanning Electron Microscopy
VFA	Voids Filled with Asphalt
VMA	Voids in the Mineral Aggregate
δ	Phase angle

Chapter 1

Introduction

Hot mix asphalt (HMA) pavement experiences three major types of distress: fatigue cracking, rutting, and thermal cracking. Cracking produced by fatigue is considered a major load-induced distress mode that affects the surface layer of the HMA. Especially in cold climates, cracks begin as micro-sized fissures that subsequently propagate to a series of interconnected cracks that require frequent maintenance and shorten the life of the pavement. This type of pavement distress has always been a major concern for pavement engineers and managers of pavement networks who seek to design long-lasting pavements that provide enhanced performance. Therefore, recent decades have been marked by significant effort dedicated to improving HMA mix resistance to fatigue cracking by understanding the mechanisms underlying fatigue phenomena. Numerous approaches have been reported in the literature including: (1) modifications to the materials that resist cracking, (2) the employment of new characterization techniques to better understand the performance, (3) the development of new failure criteria, and (4) the establishment of realistic and accurate performance prediction models.

However, the mitigation of asphalt fatigue cracking and the enhancement of fatigue resistance remain challenging issues for the following reasons:

- HMA designs that provide superior fatigue performance may also reduce resistance to other distresses because fatigue is linked with other types of pavement distress, such as rutting.
- Material complexity has led to a lack of effective characterization, which makes it difficult to establish a method that includes all mixture variables and all conditions that affect fatigue performance.
- Predictions of pavement life with respect to fatigue and induced damage are currently achieved through either empirical or mechanistic-empirical approaches. However, evaluating fatigue resistance is still controversial because such methods may be successfully applied only for local conditions and also require continuous calibration.

The focus of the research presented in this thesis was to apply advanced laboratory and image-based characterization methods as a means of providing a more scientific understanding of HMA fatigue mechanisms and subsequent mitigation. The goal is to improve HMA design methods and performance in order to provide long life design while also reducing life cycle costs.

1.1 Background

Asphalt is “a typical multi-phase composite material” (Zhu et al. 2011) that is composed of air voids, binder, and aggregate. The pavement performance is controlled by characteristics of each individual component and the compacted mixture, and these are important factors that affect service life (Kutay et al. 2010), as illustrated in Figure 1-1. The HMA mastic performance, which is composed of fine aggregate and asphalt cement, is governed by a number of constitutive laws pertaining to viscoelastic, plastic, and viscoplastic behaviour (Dai et al. 2006; You et al. 2008b). In addition, its interfacial properties have a substantial effect on HMA characterization and failure mode (Zhu 2013). The microstructure response accounts for the aggregate-to-aggregate local load transition, which significantly affects the stability of the overall structure (Sadd et al. 2004). Similarly, air void content and binder content also have a major impact on HMA performance. This complex nature of asphalt materials creates challenges that impede an understanding of the mechanisms underlying both the occurrence of and resistance to fatigue, rutting and low temperature cracking distress.

An important factor that affects asphalt performance is the fact that combining HMA design variables to produce a mix that mitigates one specific type of distress has an adverse effect on the others. The value of modifying the properties or content of a single component in a mixture may also be compromised when that component is incorporated into other mixtures. For cold regions, in which fatigue is a common distress, an optimum design is expected to extend service life by enhancing fatigue resistance but with a minimum negative impact on rutting resistance and low temperature cracking.

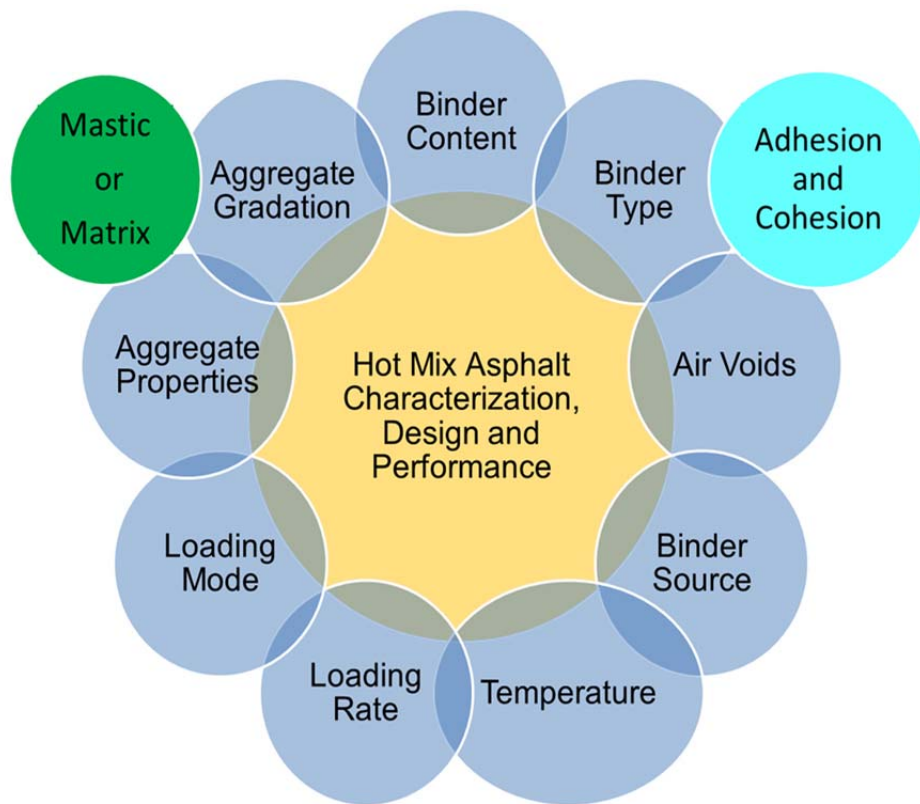


Figure 1-1 Variables that affect hot mix asphalt characterization, performance, and design

The microstructure, or internal structure, of an asphalt mix plays an important role in performance since it deals with gradation, air-void distribution, and mixture packing. While quantification of the effect of the internal structure on the mechanical behaviour of HMA cannot be achieved through experimental work (Zhu et al. 2011), the internal structure can be characterized through image-based analysis (Falchetto 2011). Recent studies have used imaging techniques for acquiring an understanding of the way internal structure influences the performance of a mixture. Two or three dimensional (2D or 3D) image-based asphalt analysis has been employed for characterizing the distribution of the aggregate (i.e., particle contacts, orientation, size distribution) and the air voids in compacted mixtures, as well as for microstructural modelling.

One of the most efficient imaging methods for use with HMA is X-ray computed tomography (CT). This nondestructive technique provides 3D characterization of the internal structure of HMA. It has rarely been applied for the quantification of HMA damage because of challenges related to the complexity of the materials, lack of a standard processing method, and computational cost. The work presented in this thesis involved the development of a framework for employing X-ray CT in order to enable the visualization and quantification of HMA fatigue damage and to provide an understanding of the effect of the internal structure on the overall response behaviour through the integration of X-ray CT and the finite element method (FEM). The resulting microstructural model provides an excellent tool for a fundamental understanding of the effect of microstructural changes on the performance of a mixture.

1.2 Research Objectives

The work presented in this thesis was motivated by three primary goals: to improve HMA fatigue resistance; to acquire an understanding of HMA fatigue using image-based analysis; and to predict HMA response based on consideration of the effect of internal structural components. The specific objectives were as follows:

- Investigate the effect of three HMA design variables that significantly impact HMA fatigue resistance: aggregate type, binder type, and binder content. To optimize the mix design, sensitivity analysis was conducted to evaluate the contribution of each variable, individually and in combination to assess interaction effects on the various HMA mixes.
- Acquire an understanding of the way each individual component affects the results. To this end, the texture of two aggregate surfaces and the stiffness levels of two binders were compared.
- Investigate the applicability of X-ray CT for quantifying damage related to HMA fatigue.

- Employ image-based analysis to acquire an understanding of HMA performance with respect to the characterization of the internal structure.
- Develop a micromechanical image-based finite element (FE) model in order to investigate the effect of changes in the internal structure on performance and stress-strain behaviour.

1.3 Research Hypothesis

The fundamental hypothesis underlying the research is that improving HMA mix design with respect to fatigue resistance results in long-lasting pavements and enhanced performance. The specific assumptions are as follows:

- Effective HMA design that includes modifications to the materials and their combinations leads to significant improvement in fatigue life.
- Improving HMA fatigue resistance mitigates fatigue cracking in pavements and enhances their performance.
- The X-ray CT technique enables the identification of the inner composition of HMA and an assessment of any damage.
- A realistic microstructural model that incorporates a variety of the constitutive laws governing asphalt mix components provides superior predictions of HMA response and performance, which are important for improving asphalt design.

1.4 Research Methodology

The methodology for this research was comprised of three main areas.

- *Experimental work*
Experimental mix matrices were designed to provide superior fatigue resistance without comprising resistance to other distresses such as rutting. The experimental evaluation of the mixtures included four tests: four-point bending, dynamic modulus,

Hamburg wheel rut, and flow number. The binders were also evaluated using the dynamic shear rheometer test in order to construct master curves.

- *Image-based analysis*

Three imaging techniques were employed for an advanced analysis of HMA characteristics and performance. First, scanning electron microscopy (SEM) was used for the aggregate texture investigation. Second, a typical simple scanner and the Ipas2 software were utilized for evaluating the internal HMA structure of samples tested under the wheel path. The X-ray CT was also employed for assessing air void distribution and fatigue damage.

- *Finite element modelling*

FE modelling was used in conjunction with the X-ray CT to develop an image-based model to investigate the effect of the microstructure on the HMA response (e.g., stress and strain) based on the aggregate elastic modulus and the experimentally determined viscoelastic properties of the matrix.

1.5 Organization of the Thesis

This thesis is comprised of eight chapters. The literature review presented in Chapter 2 explains the factors that affect HMA characteristics and HMA experimental and image-based evaluation, and provides a summary of existing micromechanical models. Chapter 3 describes the research methodology and materials; the testing setup and procedures; and specimen preparation, including the use of gyratory and vibratory compactors as well as coring and cutting. The experimental results and analysis detailed in Chapter 4 include an extensive evaluation of the fatigue life, rutting resistance, and stiffness of asphalt mixes as well as the binder performance and master curves. Chapter 5 introduces a scheme for enabling the visualization of the aggregate texture and the characterization of the internal structure, and also presents the algorithm developed for processing the X-ray CT images and quantifying asphalt fatigue damage. The image-based results are presented in Chapter 6: visualization of the aggregate texture, internal structural analysis of the test specimens, and quantification of the damage indicated by the X-ray CT. The development of the image-

based microstructural FE model and the effect of microstructure components on the HMA response are explained in Chapter 7. Chapter 8 includes a summary, the conclusions that can be drawn from the research conducted in order to meet the objectives, and recommendations for future work based on the applicability of the methods developed for this thesis.

Chapter 2

Literature Review

The research presented in this thesis entailed an extensive investigation of the characterization and performance evaluation of hot mix asphalt (HMA). The goal was to provide a precise understanding of the factors that influence HMA fatigue resistance as well as the damage mechanisms involved. To achieve this objective, both traditional experimental work and advanced image-based characterization methods have been employed. The image-based methods provided advanced tools not only for describing the internal structure of the compacted mixture but also for visualizing the texture of the aggregate. The X-ray computed tomography (CT) imaging system has been utilized for quantifying air void distribution and damage in asphalt beams as well as for building the geometry required for micromechanical finite element (FE) modelling. The methods, key findings, and gaps related to the employment of these methods for HMA characterization are summarized in this chapter.

2.1 HMA Performance and Experimental Evaluation

2.1.1 General Overview

HMA is the most widely used type of pavement material in Ontario (TAC 2013). Its primary components are fine and coarse aggregates and asphalt cement. Optional ingredients include modifiers that can be added to the asphalt cement or to the aggregates. The proportion of mineral aggregates in HMA can vary from 84 % to 90 % by volume, the volume of the asphalt cement content typically ranges from 3 % to more than 6 %, and the volume of air voids is generally 3 % to 5 % (NCHRP 2011). An ideal HMA mixture is workable, flexible, impermeable, highly resistant to permanent deformation (rutting) and fatigue cracking and capable of providing a suitable surface texture. Depending on the structure quality and gradation of the aggregate, HMA can be categorized as dense-graded, open-graded, or uniformly graded and as gap-graded or stone-mastic.

HMA is used extensively on highways, airfields, parking lots, and port facilities. It is designed to provide an expected service life with good resistance to cracking and permanent deformation under anticipated traffic loads. Its in-service performance is dependent on the properties of the mixture: workability, stripping resistance, resistance to permanent deformation, fatigue resistance, and durability (TDOT 2011). When these mixture properties are not maintained at adequate levels, HMA can be subject to a variety of forms of distress, such as fatigue cracking and rutting.

2.1.2 HMA Fatigue Cracking

A common physical pavement distress exhibited by HMA is fatigue cracking, and the measurement of the resistance of HMA to fatigue cracking is generally referred to as its fatigue life. The fatigue life of an HMA mixture is defined as the number of repeated load cycles that cause the asphalt mixture to fail at a load level well below the tensile strength of the material (Neto et al. 2009). Repeated traffic loads acting on the surface of flexible pavement induce tensile strains or stresses, which generally occur at the bottom of the HMA due to flexure or bending (Prowell 2010). A crack is usually initiated at the bottom of the asphalt layer when the number of applied load cycles reaches the fatigue life of the HMA (Neto et al. 2009). The crack then grows toward the surface of the pavement and eventually leads to the failure of the entire asphalt layer. Figure 2-1 shows a typical example of fatigue cracking.



Figure 2-1 Typical fatigue cracking in asphalt pavement

The fatigue resistance of HMA pavement is dependent on the thickness and age of the pavement, traffic loading, and the quality of the materials used in the asphalt mixture. Fatigue is not a problem in a well-designed HMA pavement where the tensile strain remains low enough to prevent the propagation of any cracks. However, fatigue cracking can occur in underdesigned HMA pavement due to high tensile strain, with the extent of the cracking being directly correlated to the level of tensile strain. An underdesigned pavement that fails due to fatigue is structurally inadequate for the traffic loading. At low levels of tensile strain (< 70 microstrains), HMA mixtures are characterized by an infinite fatigue life with virtually no damage due to their “healing potential” (Ghuzlan and Carpenter 2002). The fatigue life of HMA pavement is also significantly determined by the stiffness (dynamic modulus) of the asphalt mixture (Adhikari et al. 2009). The Mechanistic-Empirical Pavement Design Guide (MEPDG) suggests that both the tensile strain at a given location and the stiffness of the asphalt layer form the basis for establishing the fatigue life of HMA pavement (Adhikari et al. 2009). El-Hakim (2013) developed an empirical model that employed laboratory results for the calculation of in-situ tensile strain at the bottom of asphaltic layers.

2.1.2.1 Experimental Techniques for Determining HMA Fatigue Life

The literature contains reports of several experimental techniques for conducting fatigue testing of HMA mixtures. Performed under different loading conditions, frequencies, and temperatures, these tests provide dissimilar predictions of the fatigue life of an asphalt mixture. In principle, a fatigue test can be conducted under either stress-controlled or strain-controlled conditions (Neto et al. 2009). In a stress-controlled fatigue test, a constant diametric force is normally applied to a cylinder specimen in order to induce indirect tensile stress; the tensile strain increases under constant loading to the point of failure. In the case of a strain-controlled fatigue test, a specified tensile strain is applied at the bottom of a beam specimen that is usually loaded with a four-point flexure; the repeated load for the specified tensile strain decreases until failure occurs. Most researchers have used a flexural beam setup to conduct HMA fatigue testing (Al-Khateeb and Shenoy 2004; Ghuzlan and Carpenter 2002). In this type of fatigue test, failure is defined according to the number of load cycles that reduce the stiffness of the HMA mixture by 50 %. The failure point of 50 % of the initial

stiffness can be extrapolated based on the linear regression of a Weibull survivor function. The parameter of a Weibull curve can be estimated by plotting the natural logarithm of the loading cycles ($\text{Ln}(N)$) against the natural logarithm of the stiffness ratio ($\text{Ln}(\text{SR})$) according to Equation 1 (Prowell 2010; Tsai et al. 2001).

$$\text{Ln}(-\text{Ln}(\text{SR})) = \text{Ln}(\lambda) + \gamma * \text{Ln}(N) \quad (1)$$

Where

SR = flexural beam stiffness ratio (beam stiffness at cycle i / initial beam stiffness);

N = number of cycles;

γ = shape parameter (unitless); and

λ = scale parameter (unitless).

2.1.3 Dynamic Modulus of HMA

The MEPDG specifies the dynamic modulus as the primary design stiffness parameter for the characterization of HMA mixtures (Olidis and Hein 2004). For interstate and most high-volume highways that necessitate excellent load resistance, the dynamic modulus is used for characterizing asphalt mixtures (Harman 2001). The dynamic modulus varies with temperature (climatic condition), the time rate of loading (traffic conditions), and age (TAC 2013). The dynamic modulus of an asphalt mixture can be determined by conducting laboratory tests in either a stress-controlled or a strain-controlled mode. The typical viscoelastic response of an asphalt mixture is shown in Figure 2-2. Regardless of the test mode, the dynamic modulus can be calculated as the stress amplitude divided by the strain amplitude and represents the absolute value of the complex modulus, as expressed by Equation 2:

$$|E^*| = \frac{\sigma_0}{\varepsilon_0} \quad (2)$$

The dynamic modulus test enables the $|E^*|$ values of different HMA mixtures to be obtained experimentally at a variety of loading rates and temperatures and has been recommended as a means of ensuring the reliable performance of Superpave asphalt mixture

(NCHRP 2002). The method is compatible with the Standard Specifications for Performance Graded Asphalt Binder, has a direct tie to the MEPDG, provides the input parameters necessary for structural analysis, and offers a rational means of establishing performance criteria for asphalt mixtures (Harman 2001; Pellinen and Witczak 2002).

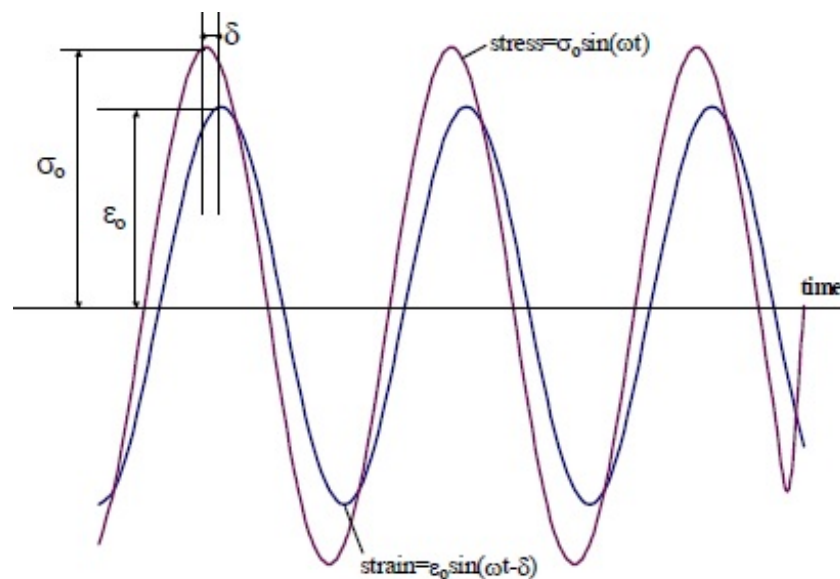


Figure 2-2 Typical viscoelastic response of an asphalt mixture (Clyne et al. 2003)

The time-temperature superposition principle can be used for constructing an HMA master curve if the measured values are shifted horizontally from the measured temperature to the chosen reference temperature. A shift factor can be calculated as the ratio of two frequencies or times at both temperatures (Chen 2011; Witczak and Bari 2004).

2.1.4 HMA Rutting

Another common physical HMA pavement distress is rutting, also called permanent deformation, which is typically a permanent surface depression that develops in the wheel path of the pavement as a result of traffic loads as shown in Figure 2-3. According to the MEPDG, HMA rutting can be classified as vertical compression and depression with shear upheavals (NCHRP 2004).



Figure 2-3 Rutting in asphalt pavement

Rutting can occur in either the HMA layers or the lower subgrade layers, or in both. This type of pavement distress has been studied intensively using conventional laboratory methods, in which mix ranking and rut depth are the parameters measured. However, a number of parameters have not been effectively investigated using these conventional methods: the effect of the internal structure and the quantification of the impact on rutting performance of mix variables such as aggregate type. Evaluation of these factors would provide an enhanced understanding of the HMA matrix and its associated impact on rutting performance.

Rutting is usually caused by insufficient compaction during the construction of the pavement, surface wear from chains and studded tires, inadequate stability of the asphalt mixture, improper mix design, or pavement whose structural capacity is deficient. One-dimensional HMA densification creates vertical compression rutting that occurs in the form of a depression without any accompanying hump. In contrast, rutting that takes the form of a depression with accompanying shear upheavals occurs because of the lateral flow of the HMA, which is usually observed in the top 100 mm of the pavement surface (Uzarowski 2006). In most cases, HMA pavement rutting is caused by a combination of densification and shear-related deformation (NCHRP 2002).

Laboratory testing using a variety of devices is very useful for predicting HMA rutting resistance. The Asphalt Pavement Analyzer (APA), the Hamburg Wheel Rut Tester

(HWRT), the French Laboratory Rutting Tester (FLRT), and repetitive creep testing as well as measurements of static creep, flow time, and the flow number are all employed for evaluating HMA rutting performance (Li et al. 2014; Rushing and Little 2013; Tayfur et al. 2007; Uzarowski et al. 2006). All current methodologies focus on the evaluation of macroscopic performance based on measurements of the densification of HMA mixes under cyclic loading. However, shear upheave, aggregate packing, segregation, and any internal structural properties cannot be easily studied using these conventional devices.

2.1.5 Effect of HMA Design Variables on Performance

HMA fatigue life is influenced by the aggregate type, aggregate gradation, asphalt cement content, and air voids (Harvey and Tsai 1996; Prowell 2010). Aggregate morphology (i.e., angularity, texture, and shape) has a noticeable influence on HMA performance (Ahlich 1996; Masad 2003; Sun et al. 2012; Wang et al. 2013). Masad et al. (2001) conducted a study to establish the relation between HMA performance and fine aggregate shape characteristics, such as form, angularity, and texture. They found that shape and texture correlate well with HMA performance. Aggregate surface texture varies from one source to another whereas other shape characteristics match well when aggregate is obtained from different quarries with similar crushing processes (Bessa et al. 2014). The *Designated Sources for Materials* (DSM) manual, from the Ministry of Transportation, Ontario (MTO), specifies the aggregate sources for HMA mix design and construction. According to this manual, the high-friction coarse and fine aggregates (FC2) obtained from crushed bedrock have been selected from dolomitic sandstone, trap rock, diabase, andesite, meta-arkose, meta-gabbro, or gneiss (OPSS1003). For an HMA surface course layer, the aggregate can be either 12.5 or 12.5FC2, which have different frictional characteristics. The effect of frictional characteristics on HMA performance therefore requires investigation.

Based on the findings of Prowell (2010); Tangella et al. (1990), binder stiffness and air voids have a greater influence on the fatigue life of HMA than other factors such as aggregate properties. Neto et al. (2009) reported that the type of asphalt cement influences asphalt stiffness, and thus the fatigue life of the HMA mixture. In recent years, several

modifiers, such as polymers, have been incorporated into asphalt binders in order to improve performance at both low and high temperatures (Kanitpong and Bahia 2005; Teymourpour and Bahia 2014; Yildirim 2007). Modified binders have a significant effect on HMA fatigue life. Mixes made with a styrene-butadiene-styrene (SBS) modified binder have been found to exhibit greater fatigue resistance than those containing an unmodified binder (Prowell 2010). With an optimal binder-modification process, stiffness might be improved so that the asphalt can sustain a load at a specific temperature without compromising stiffness at other temperatures. The findings of several studies highlighted the ineffectiveness of traditionally measured parameters, such as the shear modulus (G^*) and the phase angle (δ), with respect to evaluating fatigue performance, especially for modified binders (Hintz et al. 2011). A modified binder that meets additional specifications is known as PG Plus (Bahia and Faheem 2007). However, satisfying these additional requirements does not guarantee a full explanation of performance in the case of a particular aggregate type or specific binder content. This limitation means that the benefits of the modification process may be negated when an inappropriate aggregate is incorporated into the mixture.

Another key factor that significantly influences fatigue life is binder content. Harvey and Tsai (1996) reported that HMA fatigue resistance substantially increases with lower air voids and higher asphalt content. A high level of binder content sacrifices internal friction between the aggregate particles so that the load is transferred by the asphalt cement rather than by the aggregate (Tayfur et al. 2007). The degree of this effect may vary depending on the type of binder or aggregate. The fatigue life of asphalt mixes can be extended by integrating an optimal specific mixture of binder type, aggregate, and binder content.

Both fatigue cracking and rutting are linked with different mix variables and with the stiffness of the asphalt mixture. Fatigue life increases with a low dynamic modulus at low temperatures, whereas rutting resistance increases with a high dynamic modulus at high temperatures (Tighe et al. 2007). A certain amount of mineral filler is beneficial for increasing fatigue life and rutting resistance; however, excessive filler content increases both fatigue cracking and rutting (Al-Suhaibani et al. 1992; NCHRP 2006). An additional factor is that excessive asphalt cement content in the binder is not conducive to rutting resistance

(Neubauer and Partl 2004). For these reasons, obtaining HMA mixtures that simultaneously offer the required levels of both fatigue life and rutting resistance is often challenging.

2.2 Image-Based Analysis

Digital images can be expressed as a two-dimensional function $f(x,y)$ that signifies the color intensities at points (x, y) , where x and y refer to spatial coordinates that can be presented in the form of matrices. An image is composed of small elements called pixels that have specific locations and intensity values (Gonzalez et al. 2004). In 8-bit greyscale images, the pixel intensity varies from 0 to 255 for black and white, respectively. Figure 2-4 shows the pixel matrix of a binary image, where a value of 0 represents a black pixel and 1 indicates a white pixel. The distribution of colour intensity in image pixels is usually represented as a histogram, a statistical form that provides a simple and effective method of revealing regions and colour variations in an image.

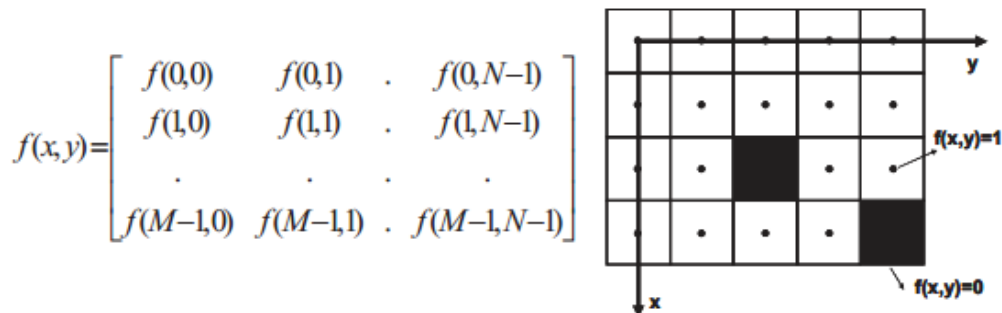


Figure 2-4 Matrix representation of an $M \times N$ binary image (Cannone Falchetto et al. 2012)

Image-based analysis can be implemented in three steps: acquisition, processing, and analysis (Masad and Kutay 2012). Images can be acquired in either two or three dimensions (2D or 3D). For 2D image acquisition, digital cameras, microscopes, and scanners have been used for capturing asphalt images. In the image-processing step, a set of operations or algorithms (e.g., filtration and thresholding) are applied in order to separate out each

individual component, such as aggregate and voids. The processed image is then analyzed in order to quantify the properties of each component, such as shape or geometry.

An imaging technique is an effective tool for identifying the internal structure of asphalt mixes (Falchetto 2011) using contrast improvement, thresholding, and edge identification (Zezelew and Papagiannakis 2007a). The captured image is processed in a greyscale, in which each pixel is assigned a number that varies from 0 (black) to 255 (white). One of the most important approaches to image segmentation is thresholding, which is applied in order to split the image composition through the selection of greyscale levels. Zezelew et al. (2007a) implemented two essential stages for calculating HMA volumetric properties: thresholding and pre-processing to enhance the greyscale image. They were then able to quantify the percentage of aggregate, mastic, and air voids in the mix.

The applicability of image-based techniques for characterizing the HMA microstructure has been investigated in previous studies (Sefidmazgi et al. 2012; Yue and Morin 1996). Some researchers have focused on the measurement of the morphological properties, or shape, of the aggregate, such as angularity and textures, while others have concentrated on the correlation of these parameters with HMA performance (Coenen et al. 2012; Kuo and Freeman 2000; Masad 2003; Masad 2007; Masad et al. 2001; Moaveni et al. 2014; Wang et al. 2013). New software (Ipas2) has been developed for analyzing the HMA internal structure from images in order to quantify aggregate contacts, segregation, and orientation (Coenen et al. 2012). This software was used for the 2D microstructure characterization of a regular asphalt mixture in a study conducted by Sefidmazgi et al. (2012). Their objective was to develop representative image-based indices to characterize the influence of the internal structure on HMA rutting measurements obtained by flow testing. A good correlation was observed between the indices developed and the asphalt flow numbers. However, this research was conducted on mixtures prior to testing; there is a strong demand for the examination of the internal structure of loaded samples. A viable avenue of investigation is the integration of an image-based technique with experimental work to be applied for both conventional and advanced analysis of the effect of a number of parameters, such as aggregate and binder types, on HMA rutting resistance.

2.2.1 X-Ray Computed Tomography

X-ray CT, a non-destructive technique that can be used for 3D image acquisition, has recently been applied more extensively for use with civil engineering materials (Wang et al. 2001). A 3D X-ray CT system is illustrated in Figure 2-5. The sample is placed between the X-ray source and a detector. The X-ray waves penetrate the sample to obtain 2D cross-sectional images. The ratio of the X-rays that reach the detector to the total X-rays sent from the source indicates the greyscale value.

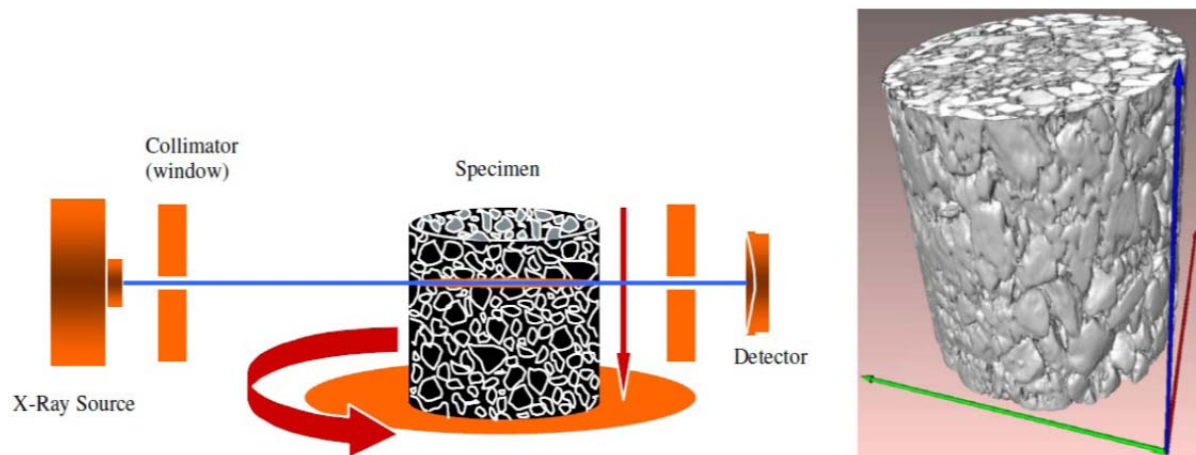


Figure 2-5 3D CT image analysis technique (Aragao 2011; Masad et al. 2005; You et al.)

Once the 2D images have been acquired and processed, image slices are then combined through a process called reconstruction in order to build a 3D model of the object (Dai 2011; Wang et al. 2001). As shown in Figure 2-6, 2D sections of the specimen obtained using the X-ray CT technique can be stacked to establish a 3D cylindrical macrostructure. In this case, the images are represented as small cubes called voxels.

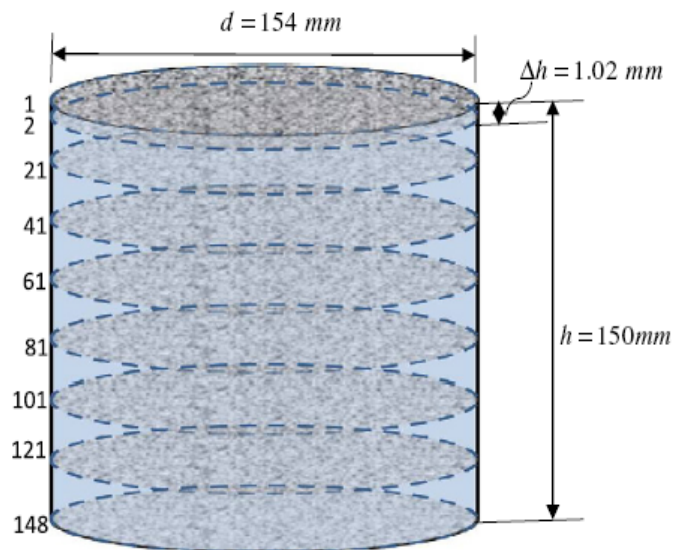


Figure 2-6 Stacked X-ray CT images (Dai 2011)

2.2.2 Applicability of X-Ray CT for HMA Characterization

Encouraging outcomes have been obtained using X-ray CT for computational simulation and for describing the interior structure of asphalt concrete mixtures (Gopalakrishnan et al. 2007). Image-based modelling has been employed for simulating HMA performance, with realistic model geometry being obtained from 2D and 3D images (Dai 2011; Liu and You 2009; You et al. 2012; You et al. 2008a; You et al.). This technique also enables an investigation of the effects of HMA microstructure components, such as air voids and aggregates, because the mechanical behaviour of each individual component can be defined separately. These models can thus be considered more realistic than ones obtained using conventional methods, which are based on the assumption that asphalt is a single homogeneous body.

Yue and Morin (1996) successfully applied a 2D digital image-processing procedure for the investigation of the orientation of coarse aggregates in asphalt mixes. The images were obtained from vertical and horizontal cross-sectional cutting planes of cylindrical asphalt samples. Four compaction methods were studied with the use of a Marshall compactor and a Superpave gyratory compactor (SGC) for obtaining laboratory samples

along with a vibratory steel roller and a multi-integrated roller (AMIR) for procuring cored samples. The study found that the aggregate gradation and shapes as well as the compaction methods influence aggregate orientation in both horizontal and vertical cross sections. The SGC can also simulate the roller compaction in the paving process, while the conventional laboratory Marshall compactor cannot. In pavement stress analysis, performance modelling should take the orientation of the structure of the aggregate particles into account because of its contribution to the anisotropic properties of the mixes.

Masad et al. (1999) characterized the inner composition of asphalt samples compacted using two types of equipment: an SGC and a linear kneading compactor (LKC). Air voids plus aggregate orientation and contact were the focus of their analysis. Contact refers to the number of contact points between coarse aggregate particles. The authors found that the SGC provided better orientation and less aggregate contact than the LKC. They also analyzed the distribution of air voids with both compaction methods and observed that both techniques resulted in an irregular distribution of the air voids, which were concentrated at both the top and the bottom of the SGC but only at the bottom of the LKC.

With respect to internal HMA structure, X-ray CT has been used for quantifying the air void distribution and for characterizing the aggregate skeleton in a compacted mixture (Hu et al. 2015; Kutay et al. 2010; Masad and Kutay 2012; Wang et al. 2001; Zelelew and Papagiannakis 2007a). Air void distribution is influenced by the gradation of the aggregate, the type of compactor, and the level of compaction (Masad et al. 2002; Masad et al. 1999; Tashman et al. 2002; Thyagarajan et al. 2010). The aggregate skeleton is differentiated according to the organization of particles in the mixture, identified based on such features as contact points, orientation, segregation, packing, and gradation. In some research, HMA gradation has been calculated based on 2D and 3D images (Kutay et al. 2010; Masad et al. 1999; Moon et al. 2015). Yue and Morin (1996) were able to quantify aggregate orientation in both laboratory and field-compacted samples. Kutay et al. (2010) developed an advanced algorithm for processing 3D images in order to successfully compute the size, location, contact points, and orientation of the aggregate particles.

X-ray CT represents an effective tool for analyzing changes in the internal structure of a material as a result of damage (Masad et al. 2003), with 2D and 3D images already having been employed for such analyses (Elseifi et al. 2011; Hassan et al. 2014; Hu et al. 2015; Muniandy et al. 2014). Elseifi et al. (2011) used X-ray CT in order to quantify the damage produced by dynamic modulus and flow tests. Their results revealed insignificant damage in the dynamic modulus specimens but notable heterogeneous damage in the flow test specimens, especially in the middle third of the specimen's height. Hassan et al. (2014) attempted to characterize the specimen damage resulting from uniaxial compression and indirect tensile fatigue tests. Crack properties were analysed for an area 40 mm wide that extended the entire thickness of the specimens. Hu et al. (2015) studied the influence of high-temperature deformation on the morphology and distribution of air voids and aggregate particles. All of these prior studies were conducted either on small test specimens with low resolution or with a focus on the damage resulting from deformation tests. Until now, the technique had not previously been used for quantifying fatigue damage in large asphalt beam specimens at higher resolutions. Research was thus required in order to characterize changes in the 3D microstructure that result from asphalt fatigue tests, particularly with respect to the flexural mode, in order to provide an understanding of the mechanisms involved in this common type of pavement distress and its mitigation.

2.3 Microstructure Finite Element Modelling

. Finite element (FE) modelling has been employed in several studies as a means of predicting the HMA response and providing an understanding of the behaviour of this material (Dai et al. 2006; Dai and You 2007; Dai and You ; You et al. 2012) .

The traditional approach to building an HMA FE model is based on the geometry of the macrostructure, in which the mix is defined as a homogeneous material. This approach produces only limited accuracy because it relies on one constitutive law and ignores the complex internal geometry. The HMA microstructure comprises three phases: aggregate, mastic or matrix (fine aggregate and binder), and air voids. These phases can be included in a microstructural FE modelling approach that enables an accurate characterization of the pavement response under a variety of loading conditions (Dai et al. 2006).

To construct a micromechanical FE model that defines the behaviour of each phase, two primary types of input are required: the three microstructure phases and the constitutive model. Recent studies of asphalt microstructural modelling have employed three approaches to incorporating the aggregate structure as separate phases in the geometry (You et al. 2013): (1) idealized aggregate shapes (Collop et al. 2007; Collop et al. 2006; Dai 2010), (2) real aggregate shapes acquired from images (You et al. 2012), and (3) randomly generated shapes (Liu and You 2009).

2.3.1 HMA Mechanistic Behaviour

In general, asphalt can be characterized using a number of models: elastic, plastic, viscoelastic, and viscoelastoplastic. Modelling of linear elastic or viscoelastic behaviour and of viscoplastic behaviour would be appropriate for low and high temperatures, respectively (Breakah 2009; Onyango 2009; Uzarowski et al.). The viscoelastic response can be represented by models of Maxwell, Kelvin-Voigt, and Burgers components, as shown in Figure 2-7.

The selection of a constitutive law is of considerable importance in the analysis of engineering problems (Uzarowski 2006). When the temperature and loading rate change, HMA mechanical behaviour can also change. Elastic or linear viscoelastic behaviour appears at fast loading rates while plastic, viscoplastic, or nonlinear viscoelastic behaviour is evident at slow loading rates. This effect is also dependent on corresponding temperatures, in addition to loading rates. For accurate HMA response prediction, the properties of the materials should be carefully identified for a wide range of temperatures, stress amplitudes, and strain rates (Onyango 2009).

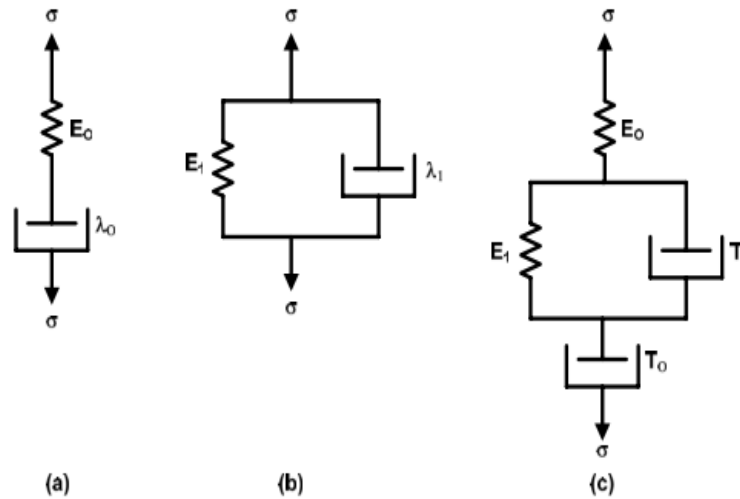


Figure 2-7 Mechanical models (a) Maxwell, (b) Kelvin-Voigt, and (c) Burger (Breakah 2009)

The generalized Maxwell model (GMM), which is represented as a series of springs and dashpots, appropriately captures the response of viscoelastic elements (Sun et al. 2013). The relaxation modulus of the GMM can be expressed as a Prony series, which is a mathematical representation that incorporates viscoelasticity into FE analysis through the application of curve fitting, as shown in Equation 3.

$$E(t) = E_e + \sum_{i=1}^k E_i e^{-t/\rho_i} \quad (3)$$

Where

$E(t)$ = the relaxation modulus;

E_e = the equilibrium modulus;

E_i = the elastic modulus of the i^{th} spring;

$$\rho_i = \frac{\eta_i}{E_i};$$

η_i = the viscosity coefficient ; and

k = the number of Maxwell elements.

The typical strain versus time curve for asphalt is comprised of four components (Masad et al. 2003; Onyango 2009; Uzarowski 2006):

- Elastic strain, ϵ_e , which is recoverable and time-independent;
- Viscoelastic strain, ϵ_{ve} , which is recoverable and time-dependent;
- Plastic strain, ϵ_p , which is irrecoverable and time-independent; and
- Viscoplastic strain, ϵ_{vp} , which is irrecoverable and time-dependent.

These four stages are illustrated in Figure 2-8 and can also be expressed by Equation 4.

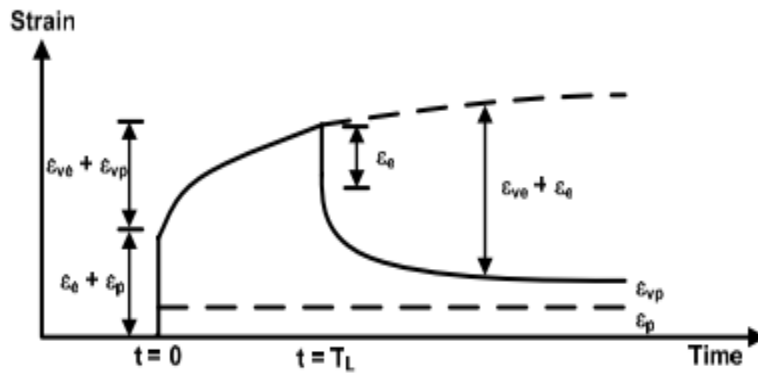


Figure 2-8 Typical strain versus time relationship for asphalt (Breakah 2009; Lytton et al. 1993)

$$\epsilon_{\text{total}} = \epsilon_e + \epsilon_p + \epsilon_{ve} + \epsilon_{vp} \quad (4)$$

In numerous studies, including those by Dai and You (2007) and Elseifi et al. (2012), viscoelastic behaviour was used in HMA or mastic modelling based on a Prony series representation of the GMM available in ABAQUS software. Viscoplastic behaviour can be represented by a power law, which is often employed in this type of modelling (Sun et al. 2013). Other studies have suggested more sophisticated models, such as combining a number of constitutive laws to obtain an enhanced response. However, the large number of parameters required has prevented the widespread application of this method.

2.3.1.1 Conversion Material Characterization

Park and Schapery (1999) developed an interconversion methodology for obtaining a relaxation modulus $E'(t)$ from the dynamic modulus $|E^*|$, which can be converted to a relaxation modulus using Equations 5 to 8. The HMA creep compliance can be obtained from Equation 9.

$$E'(\omega) = |E^*(\omega)| \cos(\phi(\omega)) \quad (5)$$

$$E'(t) = \frac{1}{\lambda'} E'(\omega) \quad (6)$$

$$\lambda' = \Gamma(1-n) \cos\left(\frac{n\pi}{2}\right) \quad (7)$$

$$n = \frac{d \log E'(\omega)}{d \log \omega} \quad (8)$$

$$D(t) = \frac{\sin(n\pi)}{n\pi E(t)} \quad (9)$$

Where

$E'(\omega)$ = the storage modulus;

Γ = the gamma function;

n = the slope of $\log(E'(\omega))$ versus $\log(\omega)$ obtained at each point of reduced frequency;

$E'(t)$ = the relaxation modulus; and

$D(t)$ = creep compliance.

Jeong et al. (2006) conducted a study in order to verify the accuracy of the interconversion of HMA viscoelastic characterization. Creep compliance was determined by converting the dynamic modulus to the relaxation modulus. Their study revealed that the conversion method can predict creep compliance. However, inconsistencies were observed, and some predictions failed to fit within a 95 % prediction interval. The authors interpreted

this result as having been affected by the high degree of constant stress associated with the creep test that was used in the study. Creep compliance or complex modulus tests can be used for describing asphalt creep compliance (Kim et al. 2008). In microstructural modelling, the viscoelastic behaviour of the mastic can be defined based on these properties.

2.3.1.2 Fine Aggregate Matrix Design

Design of sand-asphalt mortars or a fine aggregate matrix (FAM), which is composed of fine aggregate and asphalt mastic, represents a research gap that should be addressed to achieve a precise relation to the mixture characteristics (Izadi et al. 2011). Yin et al. (2011) determined the mechanical properties of FAM based on a uniaxial compression test. Their samples were prepared with the same aggregate gradation as an asphalt mixture that passes a 2.36 mm sieve. The FAM was prepared by mixing the aggregate and binder at 150 °C with 14.96 % binder content. The hot FAM was then poured into a cylindrical mold measuring 50 mm in both diameter and height. A similar method was followed by You and Buttlar (2004), but the binder percentage was 14.4 % and the sample dimensions were 75 mm in diameter and 165 mm in height. Wang et al. (2011) designed a matrix composed of a binder and an aggregate smaller than 2.36 mm by calculating the coating thickness. This method assumes that the asphalt cement coats the aggregate evenly with a constant thickness (Meininger 1992). Izadi et al. (2011) determined the FAM binder content from the total binder weight in the HMA minus the binder absorbed by the coarse aggregate.

2.3.2 Microstructural FE Modelling Techniques and Findings

Microstructure FE modelling can be achieved using a 2D or a 3D microstructure. The complex modulus and phase angle results of 2D and 3D of HMA modelling show the micromechanical FE model to be a promising tool for HMA characterization. In this type of model, the aggregate and matrix have been defined as elastic and viscoelastic materials, respectively (Dai 2011). Most previous studies have been conducted using 2D images. The techniques, procedures, and analysis applied are summarized in the following paragraphs.

Sadd et al. (2004) used ABAQUS to develop a 2D network framework FE model in order to represent the transfer of internal forces between the aggregate particles in the

asphalt. The network can be considered an equivalent to the actual asphalt microstructure and was composed of two-node elements with three degrees of freedom at each node. The model was able to simulate compression and indirect tension (IDT) tests. A comparison of the model results with the experimental data revealed a good match. This approach demonstrated an internal analysis that differs significantly from that provided by conventional modelling and provides clarification of the characterization of asphaltic materials. However, it fails to distinguish among the microstructural components.

Dai et al. (2006) developed a micromechanical 2D FE model in ABAQUS that measures the response at different loading rates and whose validation is planned through future experimental work. The model geometry was constructed using Matlab code, and the constitutive law governing the mastic was generated as a combination of the Maxwell viscoelastic model and Chaboche's plastic model. This constitutive model was included in the ABAQUS model by incorporating a user-defined subroutine for which a code was written to enable the implementation of the complex behaviour of the material.

A micromechanical FE framework was developed by Dai and You (2007) in order to predict the dynamic modulus and creep stiffness of asphalt. The model was constructed based on 2D scanned images of the microstructure. The aggregate and mastic subdomains were meshed into three-node triangular elements. The aggregate and mastic were defined as elastic and viscoelastic, respectively. The aggregate modulus was assumed to be 55.5 GPa, but the mastic properties were determined experimentally. Marginal predicted values were obtained, and the authors recommended using 3D models to incorporate the contacts between the aggregate and the FAM.

You et al. (2012) developed a 3D FE model based on X-ray CT images of aggregate and mastic that had varied properties. The aggregate was defined as an elastic material with a modulus and Poisson's ratio of 25 GPa and 0.25, respectively. The mastic was modelled as having viscoelastic, viscoplastic, and viscodamage (i.e., rate dependent and damage propagation) behaviour. A number of parameters from previous studies were integrated as a means of expressing this distinctive behaviour. The effects of these parameters were studied by simulating triaxial tests for different loading conditions and modes. A creep test was also

simulated. This research was the first related to the use of 3D imaging with a variety of loading conditions and with determined parameters for defining the coupled nonlinear-thermo-viscoelastic, thermo-visco-plastic, and thermo-viscodamage model. However, in this model, the mastic was assumed to be fully connected with the aggregate, and air voids were not included. This oversight can be considered a significant weakness because air voids are known to have a substantial impact on pavement structure and overall response (TAC 2013).

The traction-separation law has been used for modelling the aggregate-mastic interaction. This law formulates the linear elasticity (Hossain and Tarefder 2012) that represents debonding between two surfaces. Its expression is based on strength (T_0), stiffness (K), and cohesive fracture energy (Γ_c). According to this law, the initiation of failure occurs at point (δ_0, T_0) and then propagates from δ_0 to δ_c , as depicted in Figure 2-9.

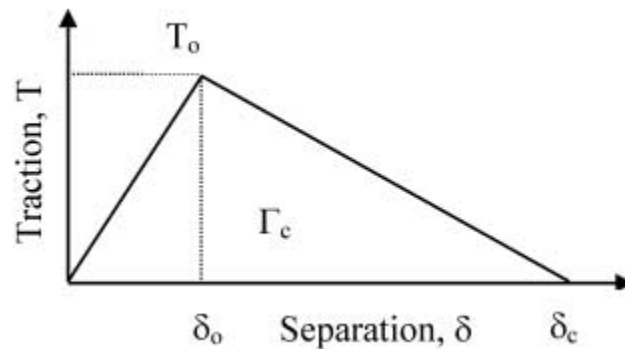


Figure 2-9 Diagram of the traction-separation law (Elseifi et al. 2012)

Hossain and Tarefder (2012) estimated the adhesive and cohesive damage to the HMA between the aggregate and the mastic using a 2D continuum homogeneous model. They focused on the damage propagation that occurred at the interface for a variety of loading rates. Their interface model was based on the traction-separation constitutive law. The mastic was defined as an elastic material with moduli of 5000 MPa and 1875 MPa for dry and wet conditions, respectively. For the ABAQUS parameters, the ultimate interface strength and stiffness for both shear and tension were adopted from another study involving a pull-off test, which measures the bond between two surfaces and can be used for determining the amount of mastic-aggregate adhesion in asphalt.

Table 2-1 summarizes the significant work conducted with respect to the numerical modelling of HMA. Most of the models were focused on the aggregate and the mastic but not their interaction, and the effect of air voids was ignored. The majority of researchers employed X-ray CT with FE modelling only in order to simulate and predict creep and the dynamic modulus.

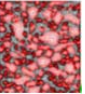
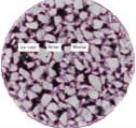
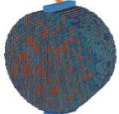
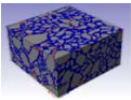
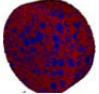
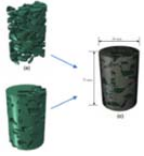

Dynamic modulus and creep tests also constituted the basis of most previously reported image-based micromechanical models. A comparison of 2D and 3D image-based models revealed that 3D models accurately capture the predicted HMA response. Limited research has been conducted with respect to predicting HMA characterization using a 3D microstructure due to the complexity and high computational cost associated with producing a precise 3D microstructural shape (You et al. 2013). Also, these models have not been used for fatigue prediction. As the table indicates, neither the impact of the morphology of the microstructure nor the effects of any changes have been adequately addressed in previously developed 3D FE models.

2.4 Summary

This chapter has presented a review of the literature related to HMA characterization and performance evaluation based on experimental HMA assessment, image-based methods, and microstructural numerical modelling. The review reveals the complexity of HMA as well as the challenges associated with the design of long-life pavement which is cost effective. In addition, typical characterization tools available are inadequate for providing an understanding of the performance impact of changes in the microstructure and design variables, information that would lead to improved design methods.

A specific adjustment to HMA composition can produce an enhanced mix that might combat one particular form of distress but compromise one or more other types. The motivation for this study was therefore to provide HMA mix designs that offer enhanced fatigue performance, which is a common distress encountered in pavement, while at the same time determining how to minimize any adverse impact on HMA rutting resistance and stiffness.

Table 2-1 Description of Numerical Models Developed for the Prediction of HMA Characterization

Reference	Predicted Characterization	Model Geometry	Aggregate Behaviour	Mastic Behaviour	Interaction	Air Voids	Imaging Method	Example
(Dai and You 2007)	Complex modulus and creep stiffness	2D	E=55.5 GPa	Linear viscoelastic	No (perfect bond)	No	Scanner	
(Mo et al. 2008)	Raveling resistance	2D	E=55.5 GPa	Viscoelastic model	No(perfect bond)	No	X-ray	
(Wang 2008)	Indirect tensile and dynamic modulus	3D	Elastic modulus	Viscoelastic models	No	No	X-ray	
(Coleri et al. 2012)	Shear modulus	2D and 3D	E= 75 GPa	Linear viscoelastic	perfect bond	Yes	X-ray CT	
(Dai 2011)	Dynamic modulus	2D and 3D	E=55.5 GPa	Linear viscoelastic	No, perfect bond	Yes	X-ray CT	
(You et al. 2012)	Uniaxial compression, tension, and repeated creep recovery	3D	E=25 GPa	Viscoelastic–viscoplastic–viscodamage model	No	No	X-ray CT	
(You et al. 2013)	Repeated creep-recovery test	3D	E=25 GPa	Viscoelastic–viscoplastic–viscodamage model	NO	No	X-ray CT	

Although the published reports indicate that significant effort has been dedicated to HMA characterization and fatigue evaluation, the mechanisms involved in and the mitigation of fatigue are still in question. This problem exists not only because of the complex composition of the HMA material and its distinctive mechanistic behaviour but also due to a lack of scientific characterization and subsequent analysis. A valuable opportunity is the application of X-ray CT as a nondestructive tool that can directly interpret and quantify HMA fatigue damage. The research is directed at this significant gap in the literature and involves the first attempt to use X-ray CT for the assessment of fatigue damage in asphalt beams subjected to a four-point bending load. This research offers a unique approach to the usage of high-resolution scanning of large asphalt specimens for characterization.

The literature review revealed that a key factor in real-image 3D microstructural modelling not previously addressed was the effect of changes in the microstructure with respect to the predicted response. The review also demonstrated a further need and existing gap in 3D microstructural models with respect to the incorporation of realistic mix variables for the determination of the prediction of response, which can lead to improvements in HMA design and associated performance.

Chapter 3

Research Methodology, Materials, and Testing

3.1 Research Plan

The research plan includes a series of tasks designed to achieve a comprehensive realistic and accurate HMA characterization using experimental laboratory based testing, advanced image-based tools, and analytical modeling. The research has been conducted to provide insight into HMA fatigue behaviour using both materials-based approaches and characterization techniques. The overall research methodology is presented in Figure 3-1, and the tasks described in the following sections have been completed to test the research hypothesis and to achieve the research objectives.

3.2 Task 1 – Literature Review

The goal of the initial task was to evaluate the current state-of-the-art in the respect to fatigue performance and HMA design. Emphasis was given to the investigation of reports related to the experimental evaluation of HMA mix performance and fatigue and rutting resistance. Previous use of image-based analysis and its applicability for the characterization of each individual component of HMA mixtures have been summarized. Studies that describe the use of FE models for HMA characterization and the application of X-ray computed tomography (CT) for obtaining accurate model geometry have also been reviewed.

3.3 Task 2 – Design of HMA Laboratory Mixes

The experimental program was designed to facilitate the investigation of the effect of aggregate type, binder type, and binder content on HMA fatigue life as well as on stiffness and rutting resistance. The calculation of the effects of these main factors and their interaction were included in a full factorial experimental design. Two aggregate types were used: high friction aggregate Superpave SP12.5 FC2 and Superpave SP12.5, which were obtained from the source recommended by the Ministry of Transportation Ontario (MTO) *Designated Sources for*

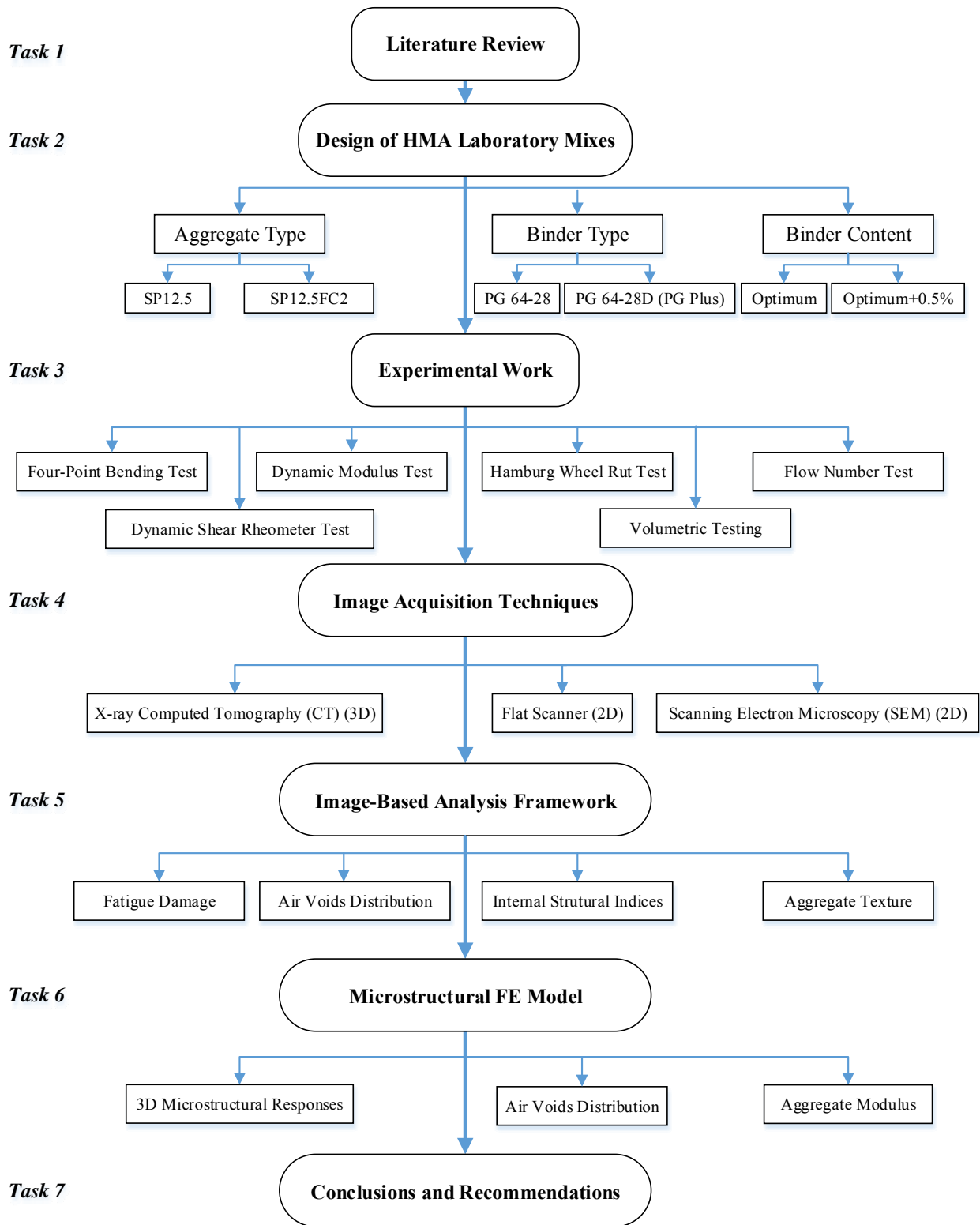


Figure 3-1 Outline of the research methodology

Materials (DSM) manual as described in the Ontario Provincial Standards and Specifications (OPSS1003 2013). The 12.5FC2 aggregate was meta-gabbro and gneiss rock. The two aggregates were selected because they provided different surface characteristics, namely, texture and frictional properties.

To offset the effect of variability in the mixes, the aggregate gradations were very similar for both aggregate types, as shown in Figure 3-2. Table 3-1 gives the consensus properties of the aggregates. Two binders with the same performance grade (PG 64-28) were used: one neat and one modified. The modification process was implemented by incorporating styrene-butadiene-styrene (SBS) to meet the PG Plus binder specifications stipulated in Ontario Laboratory Standards LS-299: the specification for determining the fracture properties of asphalt cement binders based on the double-edge notched tension (DENT) test for fatigue resistance (Hesp 2006). In this case, the modified binder was softer than the unmodified binder to provide enhanced fatigue resistance for the same performance grade. The binder properties are listed in Table 3-2. In line with the ultimate goal of improving HMA fatigue life, two levels of binder content were used: optimum and optimum plus 0.5%. This approach was adopted so that both binder types could be effectively evaluated, along with their interaction with the aggregate, and so that changes in the optimum binder content resulting from variability in the HMA design could also be taken into account.

The design, preparation, and testing of the mix were all carried out in the Centre for Pavement and Transportation Technology (CPATT) laboratory at the University of Waterloo in Canada in conjunction with the MTO. The mixes were designed to meet the Superpave^{MT} method requirements. The volumetric properties of the HMA mix design at the optimum binder content can be seen in Table 3-3. The differences in optimum binder content are relatively smaller for mixes comprised of the same aggregate type or the same binder type. However, the effect of binder content on the performance of each mix was investigated in this study.

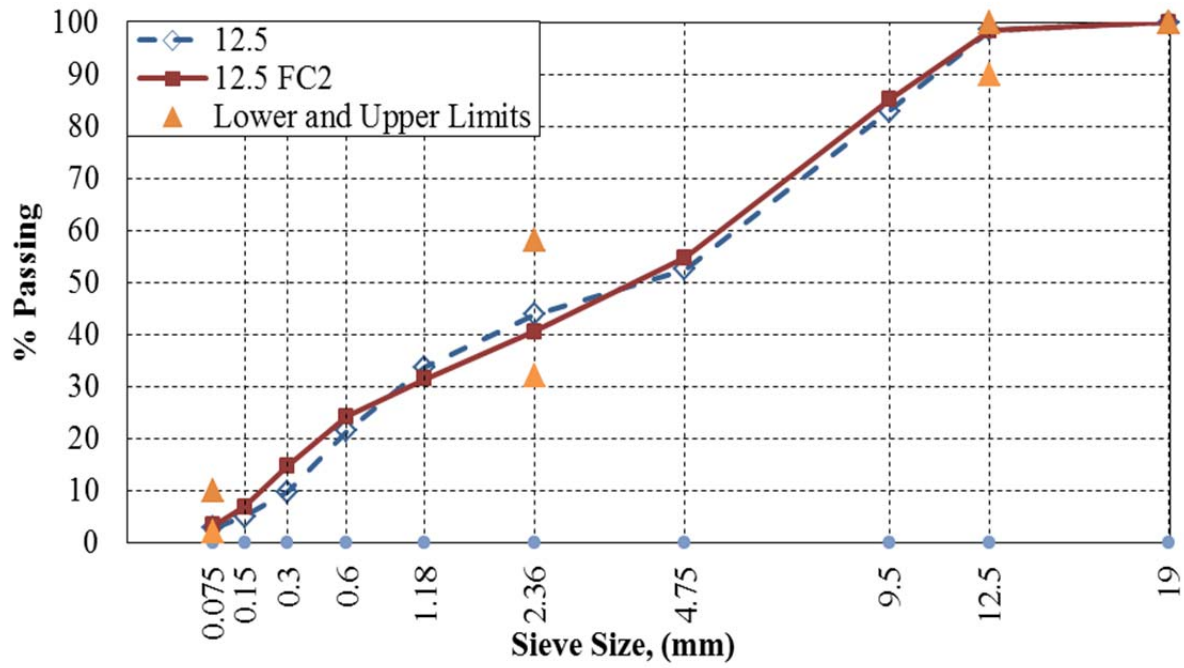


Figure 3-2 Aggregate gradations

Table 3-1 Aggregate Consensus Properties

Aggregate Test	SP12.5	SP12.5 FC2
Aggregate bulk specific gravity	2.898	2.79
Fine aggregate angularity, %	46.3	50.3
Coarse aggregate angularity, %	100	100
Sand equivalent, %	81	80
Flat and elongated particles, %	3.5	0.6

Table 3-2 Binder Properties

Binder Type	PG 64-28	PG 64-28 D (PG Plus)
Tests on the Original Binder:		
Rotational Viscosity @ 135 °C, Pa.s	0.533	0.713
Flash Point, °C	282	> 285
Dynamic Shear, G*/sin δ @ 64 °C, kPa	1.55	1.08
Tests on the RTFO Residue:		
Dynamic Shear, G*/sin δ @ 64 °C, kPa	4.11	2.27
DENT:		
δ _o CTOD, 15 °C, average, mm	-	13.2
MSCR :		
Average % Recovery @ 58 °C, at 3.2 kPa	-	52.1
Non-recoverable Creep Compliance @ 58 °C at 3.2 kPa	-	0.8
PAV:		
Creep Stiffness, MPa	163	96
m-value @ 60 s	0.308	0.361
G*sin δ @ 22 °C (kPa)	3010	1393

Table 3-3 Volumetric Properties of HMA Mixes at Optimum Binder Content

Property	SP12.5 PG64-28	SP12.5 PG64-28D	SP12.5FC2 PG64-28	SP12.5FC2 PG64-28D
Optimum binder percentage, (AC %)	5.20	4.90	5.00	5.05
Voids in mineral aggregate, VMA %	16.33	16.48	15.26	15.10
Voids filled with asphalt, VFA %	76.41	75.00	72.25	74.83
Dust to effective binder ratio	0.66	0.75	0.73	0.71

Eight different HMA mixes were investigated to accommodate the design combinations explained above; Table 3-4 identifies the HMA design matrix labels.

Table 3-4 Laboratory Mix Matrix

Mix Type	Aggregate Type	Binder type
SP12.5 PG 64-28 (opt.)	SP 12.5	PG 64-28
SP12.5 PG 64-28 (opt.+0.5)		
SP12.5 PG 64-28 D (opt.)		PG 64-28 D
SP12.5 PG 64-28 D (opt.+0.5)		
SP12.5FC2 PG 64-28 (opt.)	SP 12.5FC2	PG 64-28
SP 12.5FC2 PG 64-28 (opt.+0.5)		
SP12.5FC2 PG 64-28 D (opt.)		PG 64-28 D
SP12.5FC2 PG 64-28 D (opt.+0.5)		

SP: Superpave mix gradation; PG: performance grade asphalt cement

3.4 Task 3 – Testing of HMA Mixes

This task entailed evaluating the performance of the mixes listed in Table 3-4 using the following test methods:

- Flexural beam fatigue test
- Dynamic modulus test
- Hamburg wheel rut test (HWRT)
- Flow number (FN) test

The HMA shear flow that occurred during the HWRT tests was quantified manually at the end of each test. Binder stiffness was evaluated using a dynamic shear rheometer (DSR) to obtain data, which were then employed in the construction of master curves.

3.4.1 Flexural Beam Fatigue Test

To determine the fatigue life of the HMA mixes, a four-point flexural beam test was performed using a Cox & Sons fixture in an Interlaken hydraulic testing system located in the CPATT

laboratory. The test was carried out in accordance with the procedure given in AASHTO-T 321 (2007)-T321. The specimens were compacted using an Asphalt Vibratory Compactor (AVC). After compaction, the specimens were sawn as shown in Figure 3-3. The specimens were prepared with a length, width, and height of 380 mm, 63 mm, and 50 mm, respectively, and with air voids of $7\% \pm 1\%$. In this test, four replicates of the asphalt beam specimen were employed for each mix. In a four-point bending frame, the test beams were subjected to repeated flexural loading at a frequency of 10 Hz. The deflection level (strain level = 700 microstrains) was selected to allow the specimen to undergo a minimum of 10,000 load cycles before its stiffness was reduced to at least 50 % of the initial stiffness. The test was performed at a temperature of $20 \pm 0.5\text{ }^{\circ}\text{C}$ in a controlled chamber. A typical CPATT laboratory setup for the fatigue test is shown in Figure 3-4.



Figure 3-3 Saw cutting of fatigue asphalt beams

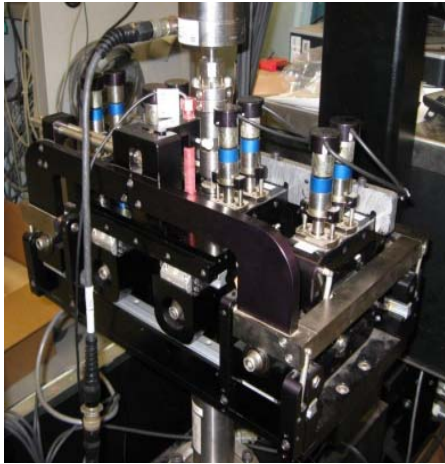


Figure 3-4 Temperature controlled CPATT flexural beam test setup

3.4.2 Dynamic Modulus Test

The dynamic modulus ($|E^*|$) of the HMA mixes was measured in accordance with (AASHTO-TP 62-07 2007). For a full evaluation of the stiffness of the HMA mixes, five temperatures (-10 °C, 4 °C, 21 °C, 37 °C, and 54 °C) were used in this study. At each temperature, the moduli were measured under six frequencies (0.1 Hz, 0.5 Hz, 1.0 Hz, 5.0 Hz, 10.0 Hz, and 25 Hz). A cylindrical sample measuring $\text{Ø}150 \text{ mm} \times 170 \text{ mm}$ high was compacted using a Superpave gyratory compactor (SGC) and was then cored and trimmed to $\text{Ø}100 \text{ mm} \times 150 \text{ mm}$ high, as shown in Figure 3-5. The test was carried out on three replicate specimens using an MTS machine. The specimens were compacted at target air voids of $7 \% \pm 0.5 \%$. The E^* of the different asphalt mixtures was tested using the CPATT materials testing system as shown in Figure 3-6.



(a) Coring of the test specimen



(b) Cored specimen



(c) Trimming the cored specimen

Figure 3-5 Coring and cutting procedures for the compacted specimen



Figure 3-6 CPATT dynamic modulus test setup

3.4.3 Hamburg Wheel Rutting Tester (HWRT)

The HWRT was performed in order to evaluate the rutting resistance of the HMA mixtures. The test was carried out in accordance with AASHTO T 324-04, Standard Test Method for HWRT of Compacted HMA (AASHTO-T 324 2008). The test setup for the rutting test is shown in Figure 3-7. For this research, three replicates were used for each mix. The samples were compacted using an SGC with a height of $62 \text{ mm} \pm 2 \text{ mm}$ at air voids of $7 \% \pm 1 \%$. The specimens were tested with solid steel wheels in wet conditions at $50 \text{ }^\circ\text{C}$. Linear variable differential transformers (LVDTs) were used for ascertaining the depth of the impression under the wheel in order to determine the rutting depth. A data acquisition system was used for measuring the amount of permanent deformation at least every 25 passes at the beginning of the test and after each 250 passes towards the end of the test.



Figure 3-7 CPATT Hamburg wheel rut tester (HWRT)

3.4.4 Flow Number Test (FN)

The FN test was used for further investigation of the permanent deformation exhibited by the HMA mixes. This test has been recommended as a supplementary test for evaluating the tertiary

flow of HMA mixes (Witczak 2007). The test involved the use of the MTS machine to apply a 0.1 sec haversine repeated load with a 0.9 sec rest period. The samples tested for dynamic modulus were also used for the FN test. All of the tests were carried out on two replicates using an unconfined loading mode at a temperature of 54 °C and under a stress level of 207 kPa (30 psi). The test was terminated when either 10,000 cycles or 5 % percent of the permanent strain was reached (Dongré et al. 2009). The FN was calculated using the Francken's model. This model has been found to be effective for both modified and unmodified mixes and for mixes that do not exhibit tertiary flow (Ameri et al. 2014). The FN test setup is shown in Figure 3-8.



Figure 3-8 Flow number test setup

3.4.5 Quantifying HMA Shear Flow

To capture more effectively the impact of the aggregate and binder contribution on the rutting resistance of the HMA mixes used in this study, the shear upheave on the rut sides was

quantified manually. As shown in Figure 3-9 (a), the total rut depth was measured using a rut bar, or straight edge, and a calliper with an accuracy of 0.01 mm. This technique simulates the manual method of measuring rut depth in the field, as shown in Figure 3-9 (b). The laboratory rut depth was represented by the depression that formed in the surface of the original samples after the test was run. It was measured using linear variable differential transformers (LVDTs) and was designated the HWRT rut depth for the purposes of the analysis. The difference between the laboratory HWRT and the total rut depth, also known as shear or lateral creep, was then quantified, as illustrated by the transverse surface profile shown in Figure 3-9 (c).



Figure 3-9 Field and laboratory measurements of HMA rutting depth: (a) total rut depth measured with a rut bar; (b) field measurement of rut depth; (c) transverse surface profile for quantifying shear upheave

3.5 Task 4 – Image Acquisition

The focus of this task was to measure HMA characteristics that cannot be established with conventional laboratory tests, such as those related to changes in the internal structure that occur during experimental tests. The following three image techniques were employed for further analysis of the experimental results:

- Scanning Electron Microscopy (SEM): This technique was used to visualize the texture of the two aggregate surfaces.

- Digital scanner: This equipment was employed to identify aggregate characteristics in the compacted mixture, such as contact points and orientation.
- X-ray CT imaging system: The images collected by the system were used to quantify the air void distribution and fatigue damage in the tested samples.

3.5.1 Scanning Electron Microscopy (SEM)

The SEM scanning facilitated the visualization of the surface texture of the aggregate particles. Aggregates sizes of 9.5 mm, 4.75 mm, and 2.36 mm were chosen from the coarse and fine aggregates. The latter two sizes were selected because the high frequency of their occurrence in the mixtures qualified them as representative samples. The 9.5 mm size was chosen to represent coarse aggregate particles. For both the high friction 12.5FC2 and the 12.5 aggregate, three particles from each size were scanned. The areas of interest and the aggregate particles to be imaged were determined randomly. The scanning conditions were similar for all scans (i.e., acceleration voltage and working distance). To provide enhanced visualization of the aggregate surface, two magnification levels were selected: 50 and 1000. The aggregate particle setup for the SEM scanning is shown in Figure 3-10.

3.5.2 2D Internal Structural Analysis

A scanner was used for capturing the asphalt images after the sample had been cut under the wheel pass at three locations. A framework was created in order to obtain representative two-dimensional (2D) digital images of the HWRT samples. The goal of developing this framework was to acquire an understanding of HMA rutting susceptibility through the use of image analysis for the characterization of the internal structure.

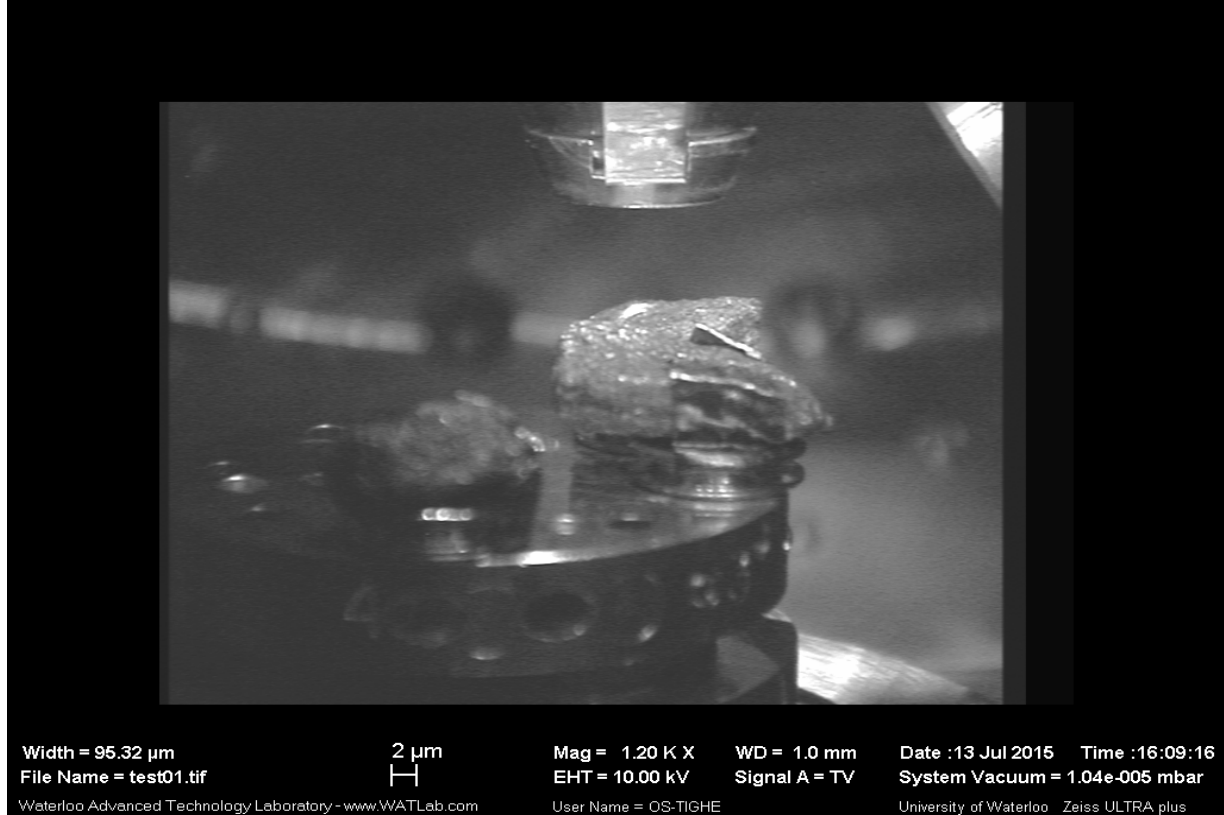


Figure 3-10 SEM test setup

3.5.3 X-Ray CT System and Imaging

The microfocus X-ray CT system at the University of Waterloo was used for scanning the beams. The sample setup and system components are shown in Figure 3-11. The beams were placed vertically between the X-ray source and the detector. Each part involved multiple scans, with the sample rotated 360° to capture 1000 images for each scan. A high resolution of 98 microns per pixel was used in this study.

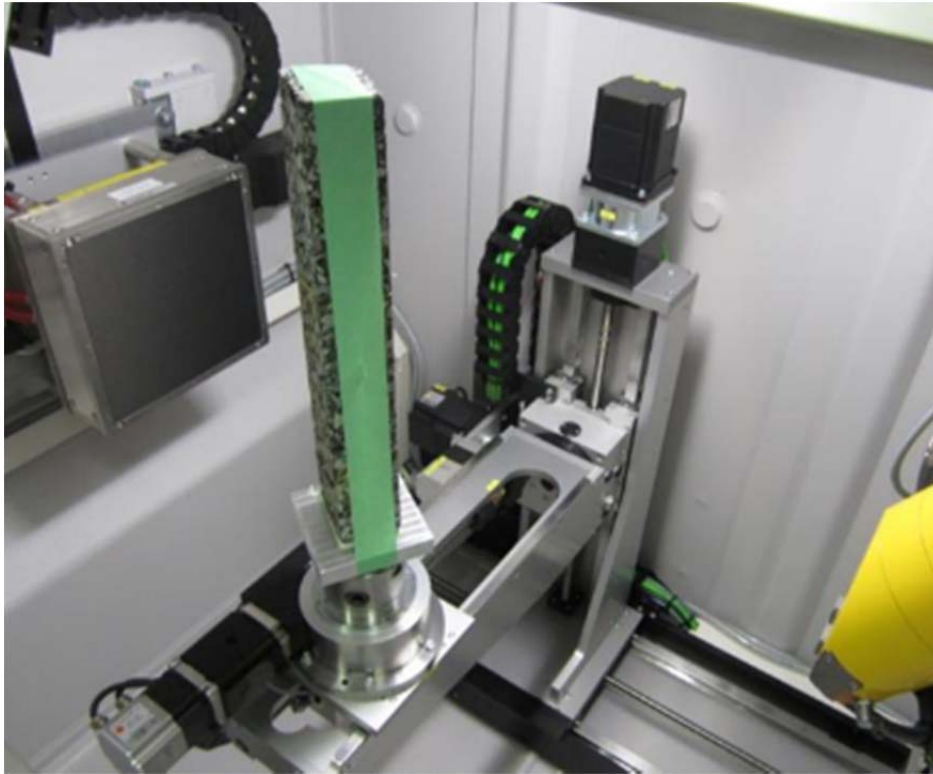


Figure 3-11 CT scanning system and test setup

3.6 Task 5 – Development of Image-Based Analysis Frameworks

This task involved the establishment of three frameworks for the effective analysis of the images acquired from the completion of Task 4. The first framework includes the steps for 3D visualization and a comparison of aggregate texture. The second framework, which was developed in order to obtain representative 2D digital images for the HWRT samples tested under the wheel pass, involves image processing and analysis as well as the measurement of the internal structural indices. The third framework employs the X-ray CT results for the quantification of HMA fatigue damage. It enables the scanning and analysis of asphalt beams subjected to a four-point bending load and then prepared for high-resolution imaging. For analysis purposes, an algorithm was designed that automatically quantifies the extent of the post-test damage to the beam based on the voxel intensities of the 16-bit aggregate images obtained when the same beams were scanned twice.

3.7 Task 6 – Microstructural Finite Element Model

The ABAQUS finite element package was used for the task of establishing 2D and 3D finite element (FE) models based on analysis of the digital images obtained from the completion of Task 5 in order to predict the HMA response, taking into account the heterogeneity of the asphalt concrete mixtures. The primary goal of the FE model analysis is to evaluate the effect of the aggregate and voids on the performance of the HMA. This model incorporated aggregate, fine aggregate asphalt matrix (FAM), and air voids and included consideration of the viscoelastic material properties of the asphalt cement. The elastic modulus and Poisson's ratio of the aggregate were assumed to be 25 GPa and 0.25, respectively (You et al. 2013) .

Two scenarios were used for examining effect of air voids and aggregate modulus on the FAM mechanical responses. In the first, FAM responses were measured in the mixture, while in the second FAM was considered as a separate phase.

3.8 Task 7 – Conclusions and Recommendations

This task summarizes the findings of this study, the data analysis and discussion, highlighting the benefits of incorporating image-based techniques in general, and 3D X-ray CT in particular, for HMA characterization. A further component of this task was to compile recommendations for improving and updating HMA design in order to enhance performance.

Chapter 4

Optimization of HMA Design for Fatigue Performance

The specific objective of the work presented in this chapter was to investigate the effect of three hot mix asphalt (HMA) design variables namely aggregate type, binder type, and binder content that significantly impact HMA fatigue resistance. To optimize the design, sensitivity analyses were conducted in order to evaluate the contribution of each variable, both separately and in combination, based on four-point bending tests of the individual mixes. To acquire an understanding of the way each individual component affects the results, the stiffness levels of the two binders were compared. The impact of all of these optimized variables on HMA stiffness and on rutting resistance was also examined.

4.1 Asphalt Binder Stiffness

To enable a full comparison of the stiffness of the neat and modified binders, the DSR was used for conducting a temperature frequency sweep test. Plates with diameters of 25 mm and 8 mm were employed in the test, which was performed at three high temperatures (46 °C, 58 °C, and 70 °C) and three intermediate temperatures (10 °C, 22 °C, and 34 °C). Master curves at 22 °C were constructed using RHEA software, as shown in Figure 4-1. Similar viscoelastic trends were observed for both binders but with slightly different behaviour. The figure indicates that, at each frequency, the modified binder is softer than the neat binder. The reduction in stiffness at a low frequency or a high temperature is relatively similar to that at a high frequency or low temperature, but more pronounced changes can be observed at intermediate frequencies. Further investigation is required to assess the effect of such reductions in binder stiffness on HMA mixture fatigue resistance.

The effect of binder modification at the various temperatures is quantified in Figure 4-2(a) and (b), which provides a comparison of the G^* values obtained for both binders at the same frequency and temperature. It can be seen that the stiffness reduction varies with temperature changes, with the modified binder exhibiting the greatest reduction in stiffness: a 65 % decrease at 34 °C (Figure 4-2a). The values were computed from the slope of the relation of G^* when the

intercept was set to zero at the same frequency for both binders. The smallest reduction (approximately 43 %) was observed at temperatures of 10 °C and 70 °C (Figure 4-2a and b). These results relatively indicate the enhanced fatigue performance of the modified binder compared to the unmodified one. This binder may produce mixes with an improved fatigue resistance and a slightly reduced rutting performance. However, binder stiffness cannot provide a good assessment of the changes in the performance of both binders that would result from varying the aggregate type and binder content. Therefore, an examination of the development of the mixture is necessary for the optimization of asphalt mix design.

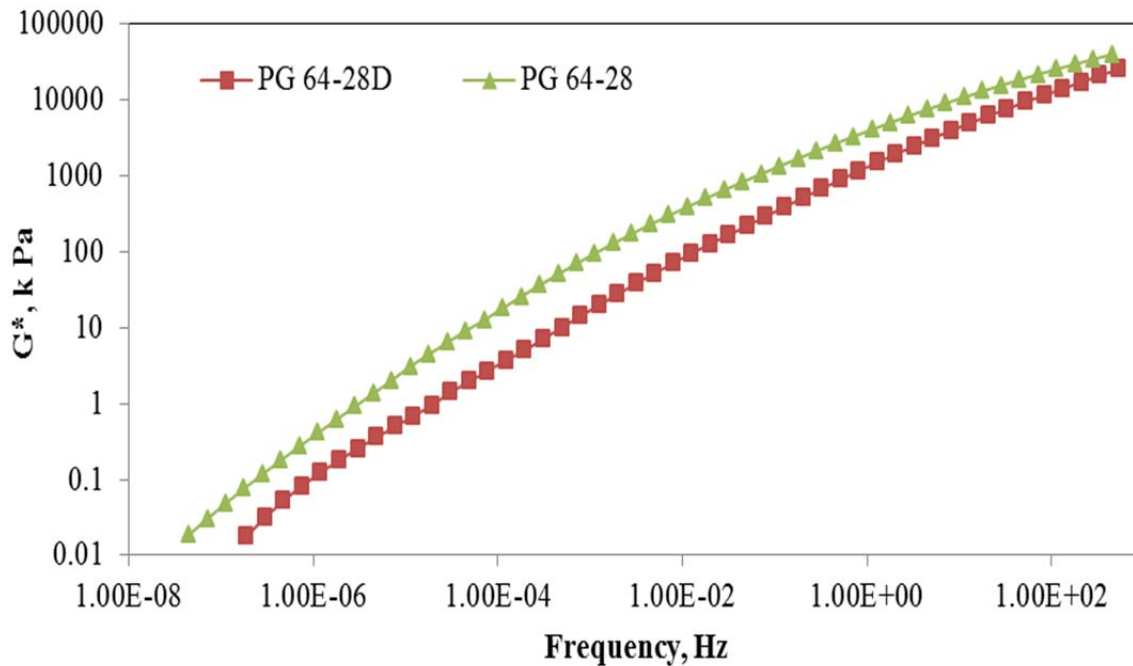


Figure 4-1 Master curves for asphalt binder stiffness (G^*)

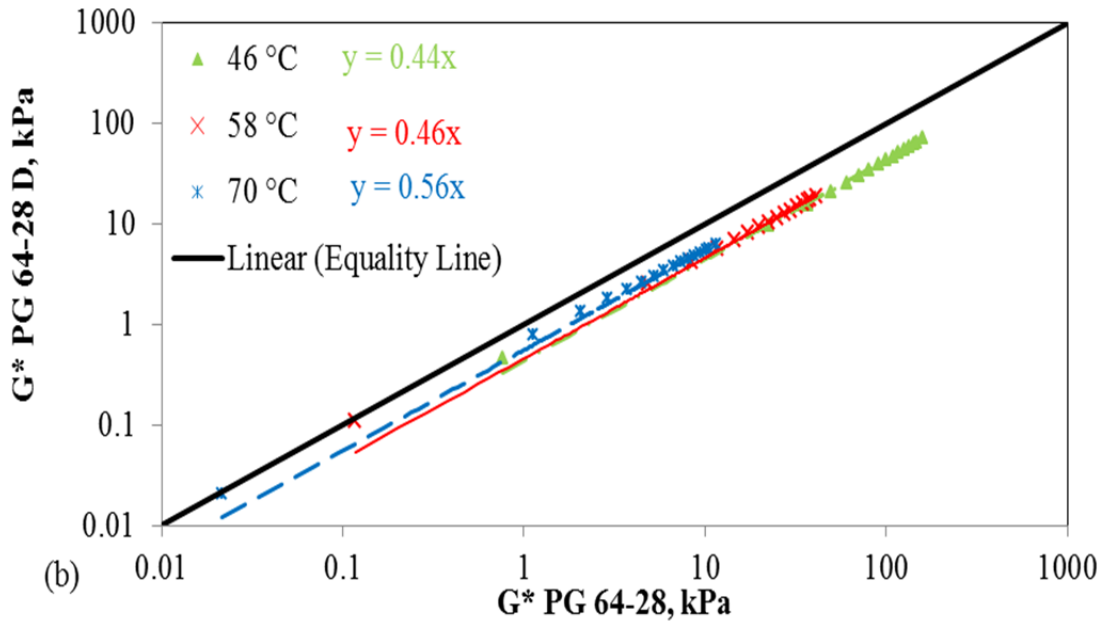
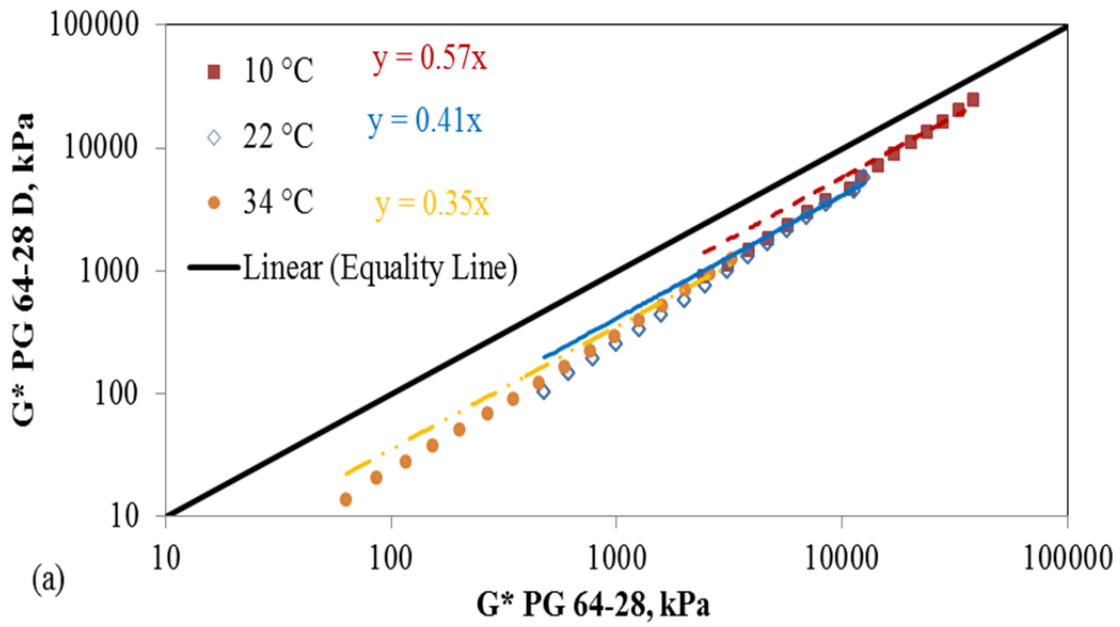


Figure 4-2 Effects of modification on binder stiffness: (a) at intermediate temperatures; (b) at high temperatures

4.2 HMA Fatigue Life Comparison

This section presents the results of the assessment of the effects of aggregate type, binder, and binder content on HMA fatigue life. Two approaches were used for comparing the fatigue performance of the HMA mixes: the stiffness approach and the plateau value (PV) approach. In the stiffness approach, the fatigue life is the number of the cycle at which the specimen reaches 50 % reduction stiffness (N_{f50}) compared to the initial value. The PV concept was introduced by Ghuzlan and Carpenter (2006) as a new fatigue failure criterion. The PV is the ratio of dissipated energy (RDE) at which no significant change occurs between two loading cycles. This approach is a distinct failure approach for evaluating damage to asphalt mixtures independently of the testing conditions (i.e., materials properties and loading conditions) (Shen et al. 2006); it is believed to be more precise for modified mixes. The following formula was used for calculating the PV (Carpenter and Shen 2006); it defines the relation between the PV, the 50 % loss in stiffness, and the dissipated energy (DE) degradation curve.

$$PV = \frac{1 - \left(1 + \frac{100}{N_{f50}}\right)^f}{100} \quad (10)$$

Where

PV= Plateau value

N_{f50} = Number of cycles to a 50 % reduction in stiffness

f = Slope of the regression of the loading cycles and the DE relation

Analysis of variance (ANOVA) at a 95 % confidence interval was used for obtaining a statistical assessment of the influence of the investigated variables on HMA fatigue life using both the stiffness and PV approaches, as listed in Tables 4-1 and 4-2. Both approaches produced consistent analysis results. The effects of all factors and their interactions were statistically significant (p -value < 0.05) except for the interaction between binder type and aggregate type. These findings confirm the substantial impact of binder content and binder type on the fatigue life. The interaction of binder type, binder content, and aggregate type was also shown to be

statistically significant, which is an indication of the importance of integrating these three variables to maximize performance.

Figure 4.3 presents the results of the fatigue test obtained using the two approaches. In general, a similar ranking can be observed for both approaches. For example, mixes for which the stiffness approach indicated a higher fatigue life exhibited lower levels of damage when characterized using the PV method. It can be seen that the 12.5 mixes exhibited a significantly higher fatigue life than the high friction aggregate (12.5FC2). The range of improvement varied from 2.5 to 4.6 times, depending on the binder type and its content. This improvement might be attributed to the smooth aggregate texture, which produces mixes with lower stiffness (Masad 2007).

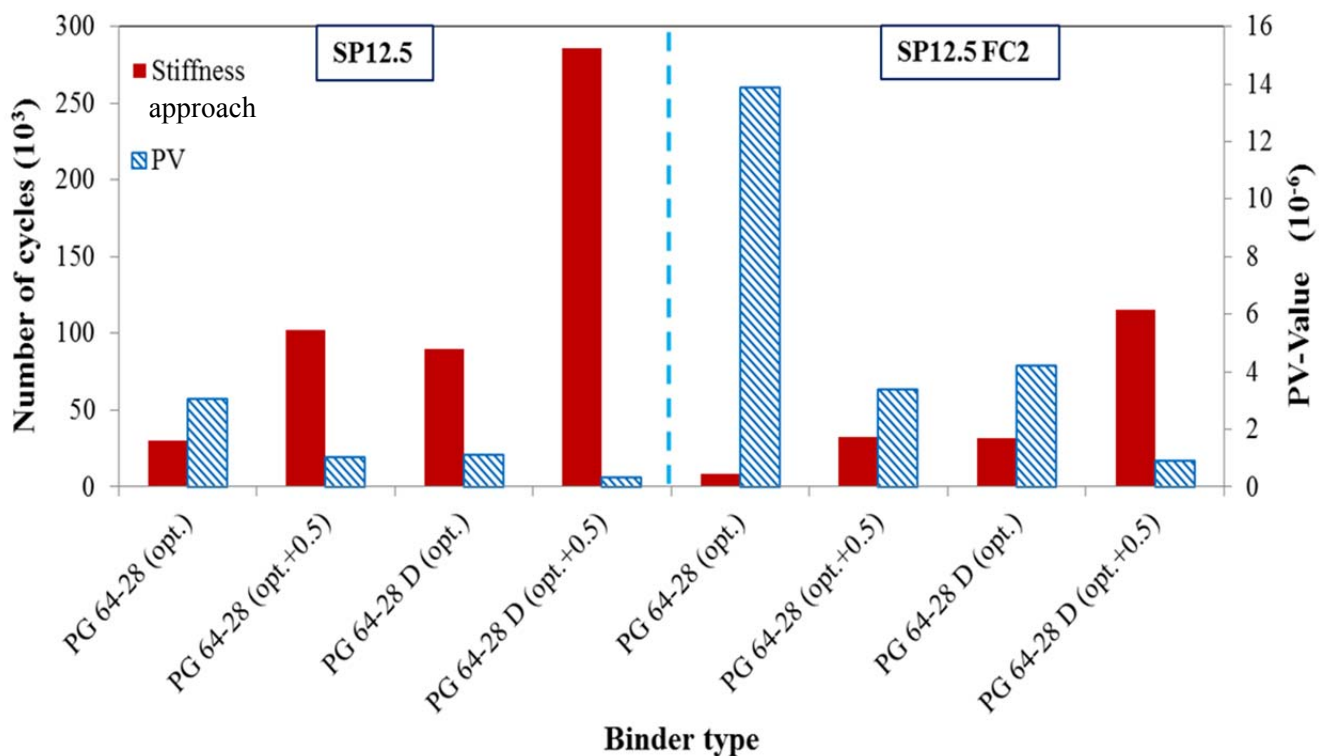


Figure 4-3 Fatigue life and PV values of the HMA mixes

Table 4-1 Analysis of Variance Fatigue Life Results at N_{f50} on a Log Scale

Source	DF	Seq SS	Adj SS	Adj MS	F	P	S*
Main Effects	3	7.7	7.7	2.6	15.1	0	Yes
Aggregate Type	1	1.6	1.6	1.6	9.4	0.005	Yes
Binder Type	1	3.1	3.1	3.1	18.4	0	Yes
Binder Content	1	3.0	3.0	3.0	17.6	0	Yes
2-Way Interactions	3	23.3	23.3	7.8	45.8	0	Yes
Aggregate Type*Binder Type	1	0.0	0.0	0.0	0.0	0.924	No
Aggregate Type*Binder Content	1	11.6	11.6	11.6	68.4	0	Yes
Binder Type*Binder Content	1	11.7	11.7	11.7	69.0	0	Yes
3-Way Interactions	1	2.3	2.3	2.3	13.7	0.001	Yes
Aggregate Type*Binder Type*Binder Content	1	2.3	2.3	2.3	13.7	0.001	Yes
Residual Error	24	4.1	4.1	0.2			
Pure Error	24	4.1	4.1	0.2			
Total	31	37.4					

SS: sum of squares; DF: degree of freedom; MS: mean of squares; Adj: adjusted; Seq: sequential; S*: significant

Table 4-2 Analysis of Variance for the PV on a Log Scale

Source	DF	Seq SS	Adj SS	Adj MS	F	P	S*
Main Effects	3	8.9	8.9	3.0	14.8	0	Yes
Aggregate Type	1	1.6	1.6	1.6	8.0	0.009	Yes
Binder Type	1	3.2	3.2	3.2	15.8	0.001	Yes
Binder Content	1	4.1	4.1	4.1	20.6	0	Yes
2-Way Interactions	3	26.5	26.5	8.9	44.0	0	Yes
Aggregate Type*Binder Type	1	0.0	0.0	0.0	0.0	0.937	No
Aggregate Type*Binder Content	1	13.3	13.3	13.3	66.2	0	Yes
Binder Type*Binder Content	1	13.2	13.2	13.2	65.9	0	Yes
3-Way Interactions	1	2.7	2.7	2.7	13.3	0.001	Yes
Aggregate Type*Binder Type*Binder Content	1	2.7	2.7	2.7	13.3	0.001	Yes
Residual Error	24	4.8	4.8	0.2			
Pure Error	24	4.8	4.8	0.2			
Total	31	43.0					

SS: sum of squares; DF: degree of freedom; MS: mean of squares; Adj: adjusted; Seq: sequential; S*: significant

For both analysis approaches, the modified binder resulted in a fatigue life of 2.7 to 3.7 times greater than that produced by the neat binder. This improved fatigue life value obtained with the modified binder was relatively higher in the case of the high friction aggregate. Furthermore, the addition of the extra 0.5% binder to the optimum amount had a significant impact on the enhancement of the fatigue life (around 3 times higher), with almost the same effect as changing the aggregate and binder types. The same trend was observed for both aggregate types with respect to the effects of using the modified binder (PG Plus) and by adding the extra 0.5% of binder content: a significant enhancement of HMA fatigue life could be noted, which emphasizes the importance of these two factors.

After the effect of each variable was obtained, a significant improvement in fatigue life was observed when the positive effects of a number of variables were combined, as presented in Figure 4-3. The best mix with respect to fatigue resistance was composed of the 12.5 aggregate and modified binder at the optimum binder content plus 0.5%. This performance was approximately 34 times better than that of the worst mix, which was composed of the high friction aggregate with the neat binder at the optimum binder content. However, performance was enhanced by approximately 9 times when 0.5% extra was added to the optimum binder content in the worst mix. The improvement in performance was reduced to only 14 times when the aggregate type in the best mix was changed to the high friction aggregate. Similarly, compared with the worst case, 12 times the fatigue life can be obtained when the binder type is altered to the unmodified binder in the best mix.

The conclusions to be drawn from the fatigue test results indicate that using a specific type of aggregate can either maximize or limit the benefits of modifying the binder in order to achieve softer mixes with improved fatigue life. The high friction aggregate negatively affects HMA fatigue, a result attributable to the irregular shape of the texture, which produces thinner coated spots and increased stiffness. The effect of the thickness of the binder coating might also provide a valid explanation for the improved fatigue life of mixes made with the extra 0.5% binder content added to the optimum, which lowers the internal friction between the particles and creates softer mixes. For all of these reasons, limitations associated with the aggregate source might be addressed by slight modifications to the amount of binder content. These conclusions

can be applied in order to optimize Ontario HMA mix design through the allocation of HMA mix components.

4.3 Reverse Impact Analysis

As expected, the recommendations or modifications for providing improved fatigue resistance would negatively impact HMA resistance to other distresses. For benefits to be maximized, such a reverse impact must be addressed. For this purpose, the stiffness and rutting resistance of the HMA mixes were compared, as follows.

4.3.1 HMA Mix Stiffness

The HMA mix master curves were constructed at 21 °C, as presented in Figure 4-4. The overall coefficient of variation of the dynamic modulus data for all mixes is 8.9 %, with variations from 4.4 to 15.7 for different mixes. It can be seen that mixes that included the modified binder showed a similar viscoelastic trend without any unusual observations. This behaviour was exhibited by both the 12.5 aggregate and the 12.5 FC2. To enable an examination of the sensitivity to stiffness of the HMA mixes, a pairwise comparison of the effect of aggregate type, binder type, and binder content on the stiffness of the HMA mixes $|E^*|$ at different temperatures and frequencies is provided in Figures 4-5 (a), 4-5(b), and 4-5(c), respectively. Figure 4-5 describes the specific percentage changes associated with each variable studied, which were computed based on the following formula:

$$\text{For Figure 4-5 (a) Change in } E^*, \% = [(E^*_{12.5FC2} - E^*_{12.5}) / E^*_{12.5}] * 100 \quad (11)$$

$$\text{For Figure 4-5 (b) Change in } E^*, \% = [(E^*_{PG\ 64-28} - E^*_{PG\ 64-28D}) / E^*_{PG\ 64-28D}] * 100 \quad (12)$$

$$\text{For Figure 4-5 (c) Change in } E^*, \% = [(E^*_{opt.} - E^*_{opt.+0.5}) / E^*_{opt.+0.5}] * 100 \quad (13)$$

In general, the HMA stiffness levels were very sensitive to all of the mix variables studied. The overall percentage change in HMA stiffness due to the incorporation of the high friction aggregate was 14.11 %, with variations related to binder type and content. Figure 4-5 (a)

shows that this effect was significantly greater at higher temperatures (37 °C, 54 °C) than at lower temperatures (-10 °C, 4.4 °C). One explanation could be that when the temperature increases, the binder tends to become softer, and the aggregate may provide a greater contribution to the stiffness due to the aggregate texture and packing in the HMA mixture. This result can be considered an important indication of the impact of high friction aggregate with respect to resistance to permanent deformation. The mix made of the high friction aggregate also showed almost no change in HMA stiffness compared to the 12.5 aggregate when the modified binder (optimum binder plus 0.5%) was used.

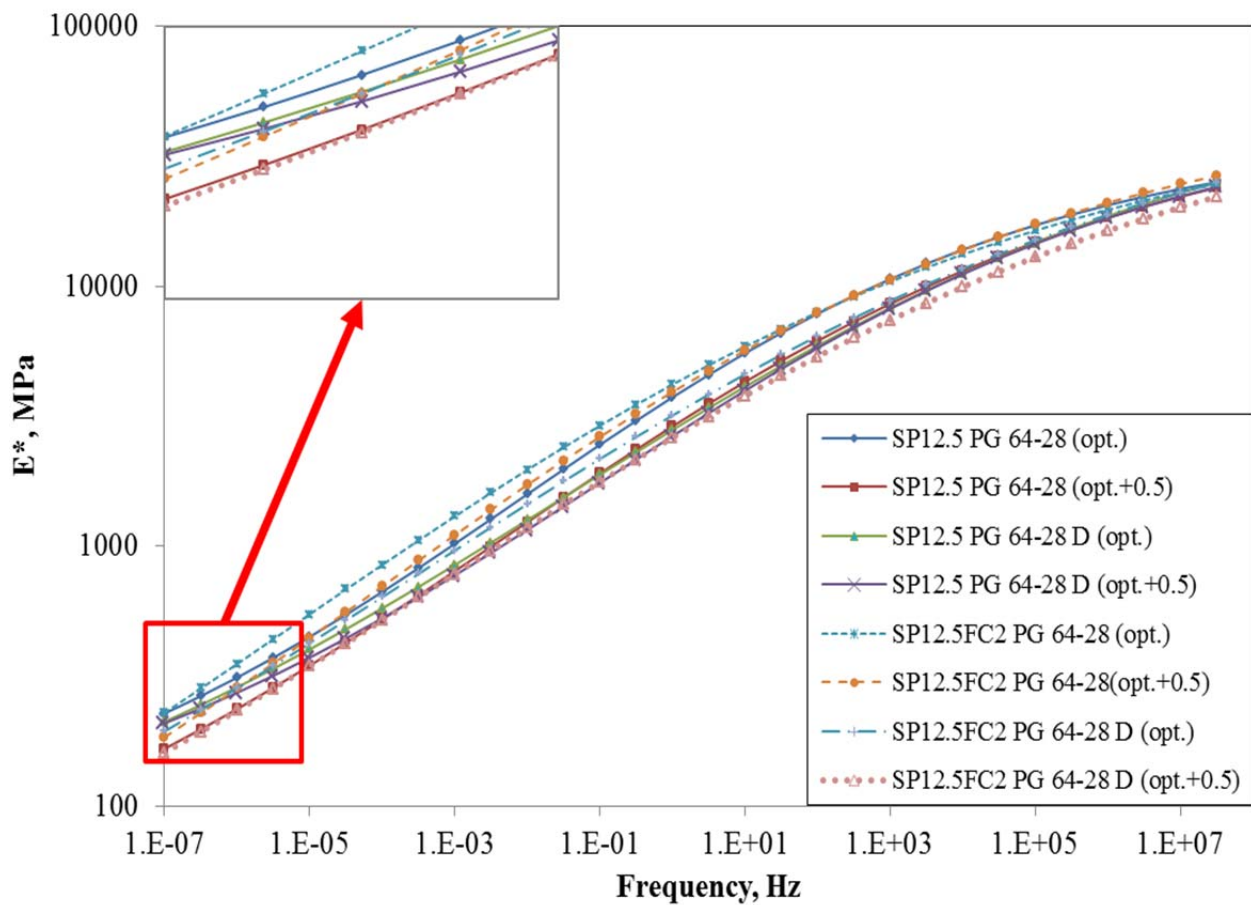


Figure 4-4 Master curves for the HMA mixes at 21 °C

As revealed in Figure 4-5 (b), the effect of binder modification on HMA stiffness is clear. At the two binder levels, the unmodified binder was found to be on average 29.5 % and 10.65 % stiffer for the SP 12.5 and 26 % and 42 % for the SP 12.5 FC2. It seems that the interaction of binder type with the high friction aggregate is greater than with the SP12.5. It can also be observed that the change in stiffness with the binder type varies more at intermediate temperatures than at either low or high temperatures.

A comparison of the values given in Figure 4-5 (c) with those in Figures 4-5 (a) and 4-5 (b) reveals that increasing the optimum binder content by 0.5% had relatively less impact on HMA stiffness. Stiffness changed significantly when the high friction aggregate was used with the lower stiffness binder (modified) or when the 12.5 aggregate was used with the higher stiffness binder (unmodified). These findings confirm that the benefits of modifying asphalt binder to obtain a specific binder may be substantially reduced when used with a specific inappropriate aggregate. The benefits of the improved fatigue resistance in these mixes will thus maintain an ideal amount of mix stiffness for resisting other distresses such as rutting and low-temperature cracking. As discussed earlier, this behavior could provide optimum values if the appropriate binder and aggregate types were used.

To show additional details about the performance of the HMA mixes, the dynamic moduli at 54 °C for all frequencies used in the test are presented in Figure 4-6. It can be clearly seen that the stiffness measurements for the 12.5 FC2 mixes were higher than for the 12.5, which may indicate the importance of internal resistance in a high-friction aggregate in improving the HMA rutting resistance. A relatively similar trend in the change in HMA stiffness was observed after modifications to the binder type and content. At 54 °C for 1 Hz, the statistical analyses were conducted at a 95 % confidence interval, as shown in Table 4-3. The analysis shows that the type of aggregate and the type and content of the binder have a significant influence on HMA stiffness.

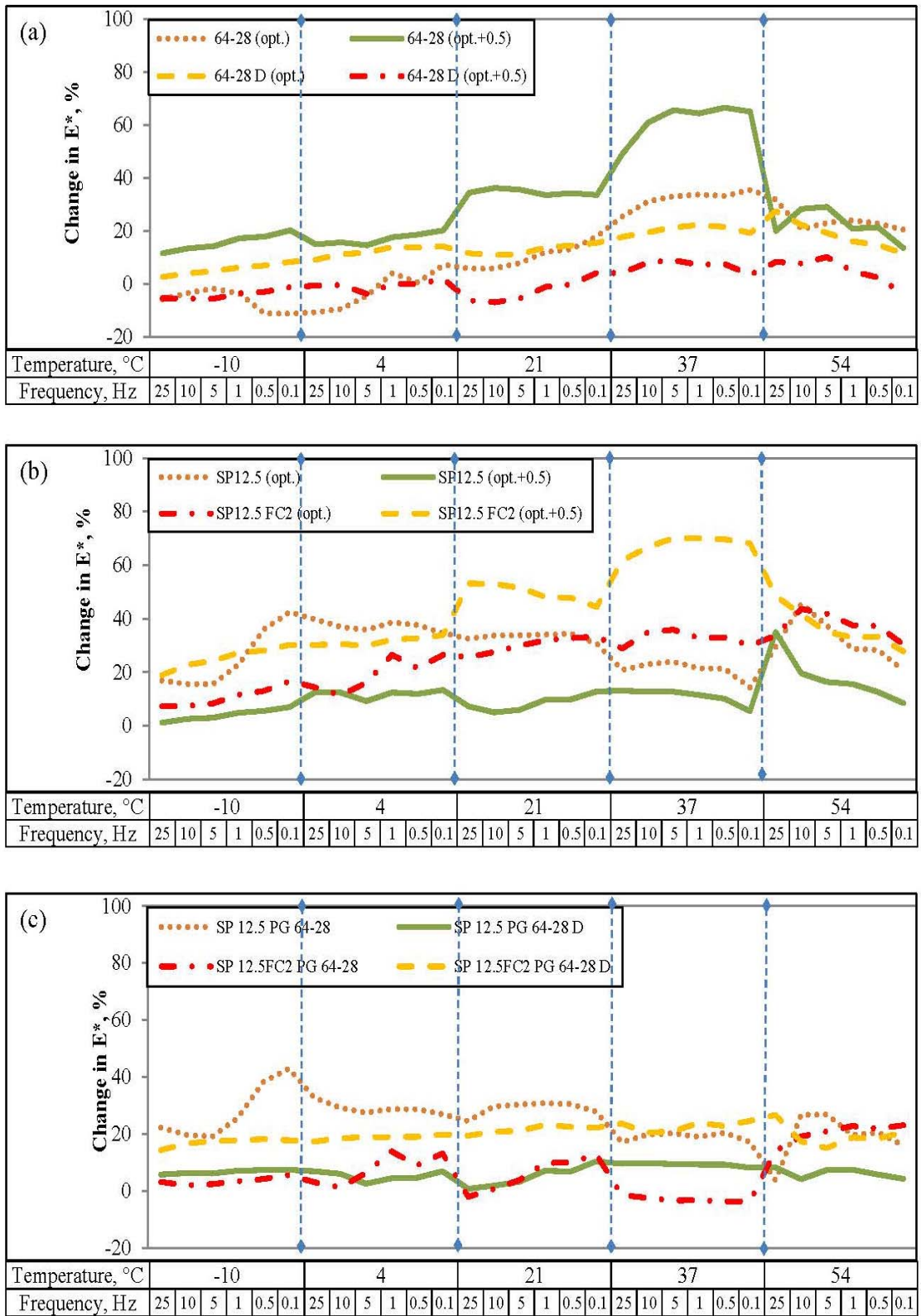


Figure 4-5 Sensitivity analysis of E^* changes: (a) effect of aggregate type; (b) effect of binder type; (c) effect of binder content

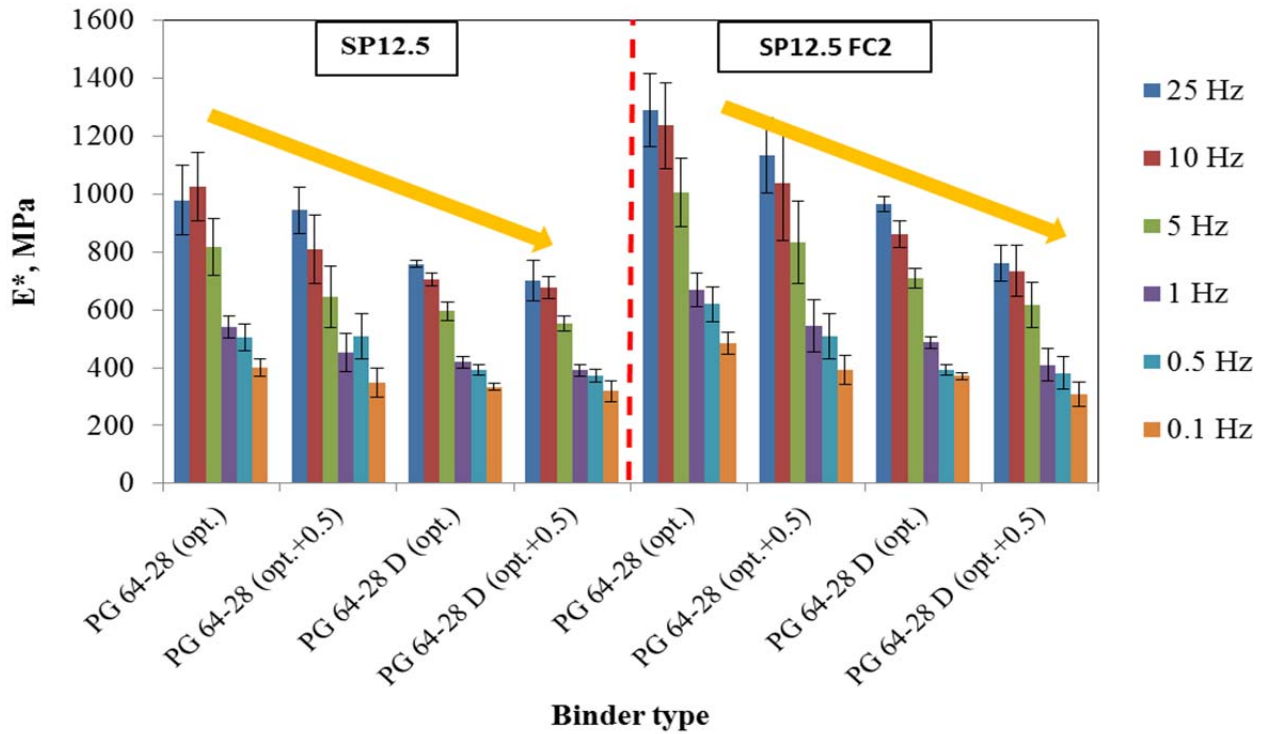


Figure 4-6 Dynamic moduli of the HMA mixes at 54 °C for different frequencies

Table 4-3 Analysis of Variance for E* at 54 °C and 1 Hz

Source	DF	Seq SS	Adj SS	Adj MS	F _{calculated}	P	S*
Main Effects	3	152,446	152,446	50,815.2	17.72	0.000	Yes
Aggregate Type	1	69,311	69,311	69,311	24.18	0.000	Yes
Binder Type	1	54,324	54,324	54,323.6	18.95	0.000	Yes
Binder Content	1	28,811	28,811	28,811	10.05	0.006	Yes
2-Way Interactions	3	22,973	22,973	7657.6	2.67	0.083	Yes
Aggregate Type*Binder Type	1	15,837	15,837	15,836.8	5.52	0.032	Yes
Aggregate Type*Binder Content	1	2059	2059	2059.4	0.72	0.409	No
Binder Type*Binder Content	1	5077	5077	5076.7	1.77	0.202	No.
3-Way Interactions	1	327	327	327.5	0.11	0.740	No
Aggregate Type*Binder Type*Binder Content	1	327	327	327.5	0.11	0.740	No
Residual Error	16	45,871	45,871	2866.9			
Pure Error	16	45,871	45,871	2866.9			
Total	23	221,617					

SS: sum of square DF: degree of freedom MS: mean of squares Adj: adjusted Seq: sequential S*: significant

For the relationships illustrated in Figures 4-7 (a), 4-7 (b), and 4-7 (c), a comparison of E^* at 54 °C at the same frequencies shows the magnitude of the effects of aggregate type, binder type, and binder content on the stiffness of the HMA mix, respectively. All relationships were characterized by a very high coefficient of determination (R^2) in the linear regression. The linear relationships are attributed to the dynamic modulus test procedure. The test focuses on the HMA linear viscoelastic behavior and is independent of the stress or strain amplitude

Figure 4-7 (a) shows that the 12.5 FC2 was stiffer by 8 % to 42 % compared to the 12.5 mixes. This finding highlights the importance of aggregate type and its impact on HMA rutting depth. On the other hand, the unmodified binder had noticeably greater stiffness than the modified ones, as can be seen in Figure 4-7 (b). The figure indicates that the degradation (approximately 25%) in stiffness in the unmodified binder was relatively similar to that in the modified binder when aggregate type and binder content were changed. Figure 4-7 (c) clearly reveals the negative effect on HMA stiffness when the extra 0.5% was added to the optimum binder content. The deterioration in stiffness was relatively similar for the three mixes (approximately 16 %) but differed for the SP12.5 mix with the modified binder, which showed a 6 % reduction in stiffness.

Table 4-3 shows the statistical analysis of the effect of the three variables on the HMA, which was computed as a full factorial design of the experiment. The analysis indicated that the effect of the main factors (aggregate type, binder type, and binder content) was statistically significant. In addition, the interaction between the binder type and aggregate type also confirmed the significance of their effects. The results revealed that the mixture containing the unmodified binder and the high friction aggregate exhibited the greatest stiffness. The interaction between binder type and binder content had no significant impact on HMA stiffness. These results seem to be consistent with the quite similar reduction in stiffness due to the additional binder content for a variety of combinations, as indicated in Figure 4-7 (c). This interaction also emphasizes the importance of full factorial design in capturing such effects and in optimizing HMA mix design. In conclusion, it can be seen that the use of 12.5 FC2 significantly improved HMA stiffness, in contrast to the negative impact of the PG Plus and additional asphalt cement content.

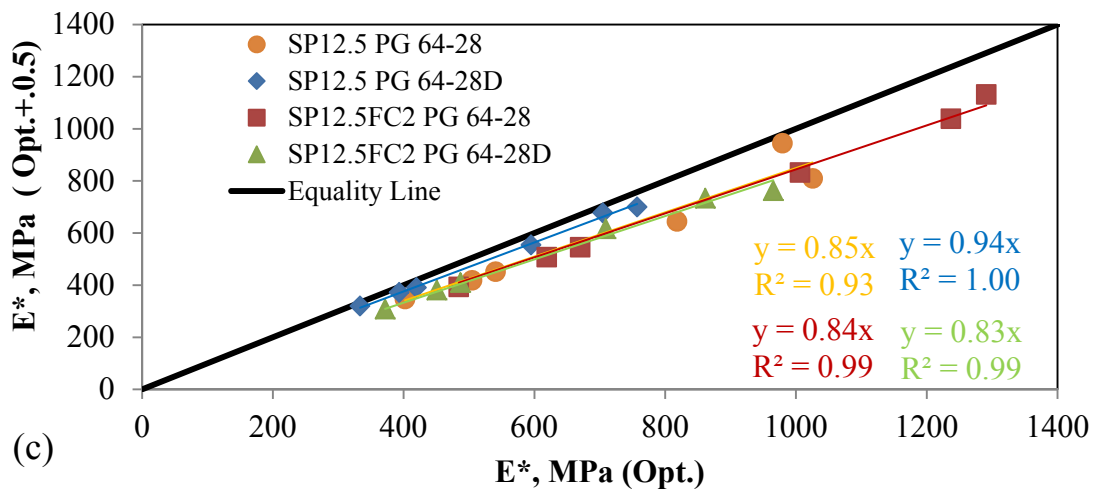
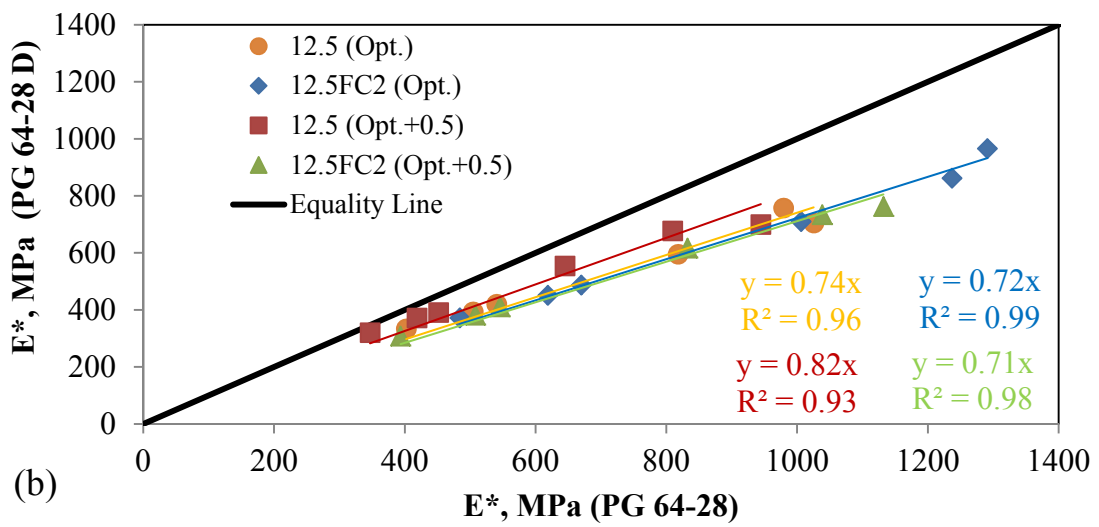
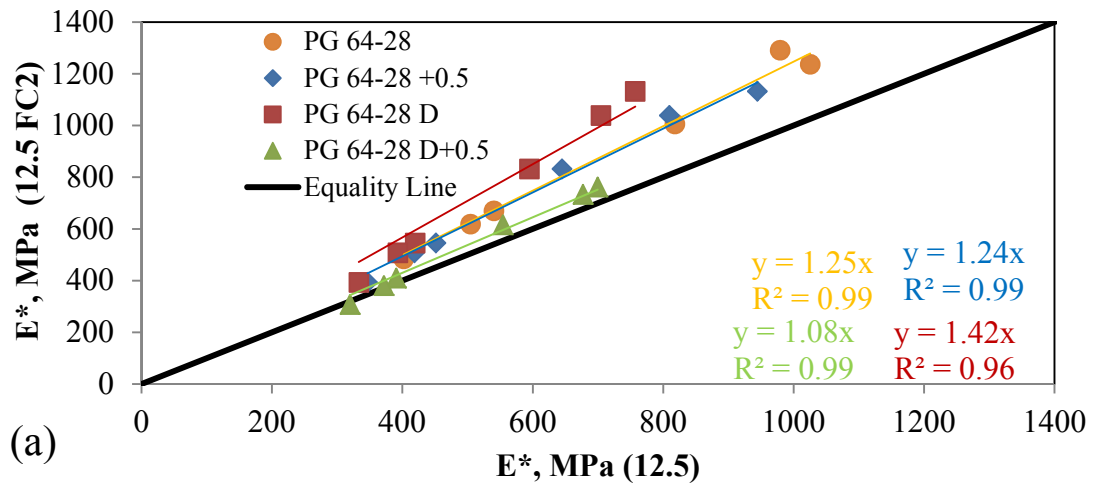


Figure 4-7 Relationships between the dynamic moduli of the HMA mixes at 54 °C and a variety of frequencies: (a) effect of aggregate type; (b) effect of binder type; (c) effect of binder content

4.3.2 HMA Mix Rutting Resistance

The purpose of the work presented in this section was to assess the rutting resistance of surface layer Superpave mixes that were designed to provide superior fatigue resistance. The rutting resistance was measured by HWRT test. Figure 4-8 shows the average rutting depth versus the number of wheel passes relationship of the submerged samples. In general, this test results provide the combined effect of rutting and moisture damage. The moisture damage starts after the stripping inflection point that occurs between the creep region and the stripping region. However, there is no indication of stripping inflection point for all investigated mixes, as presented in Figure 4-8. Therefore, the HMA mixes had an excellent moisture damage resistance and the measured permanent deformation was related to the rutting resistance. The analysis of variance (ANOVA ($\alpha = 0.05$)) of the maximum rutting depth at 20,000 wheel passes is presented in Table 4-4, which indicates a statistically significant difference in the rutting resistance of the HMA mixes.

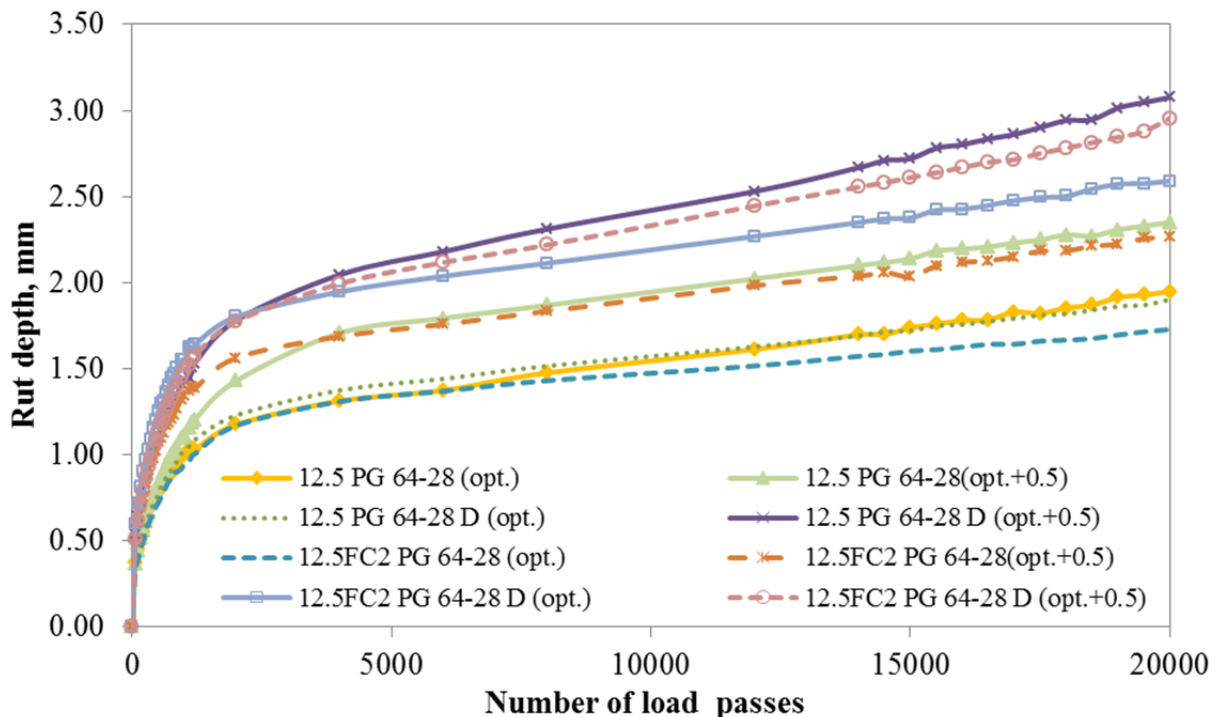


Figure 4-8 HWRT rut depth versus number of load passes

Table 4-4 ANOVA Statistical Analysis of HWRT Results

Source of Variation	SS	df	MS	F	P-value	F crit
Between Groups	5.14	7	0.73	13.33	1.32E-05	2.66
Within Groups	0.88	16	0.055			
Total	6.02	23				

The levels of rutting resistance of the HMA mixes were compared, as shown in Figure 4-9. Visual observation reveals that rutting resistance decreased with changes in binder type and with the addition of the extra 0.5% to the optimum binder. Similar trends can be noted for rutting resistance measured using HWRT, total rut depth (manually), and rutting rate.

Mixes composed of the modified binder showed greater rutting resistance, or more permanent deformation, than those containing the unmodified binder of the same grade. It was expected that the modified binder would provide less rutting resistance, as indicated in Table 3-2 by the reduction in the rutting parameter $G/\sin \delta$, but, the rutting depths for all mixes were acceptable (< 12.5 mm) (Uzarowski et al. 2006; Yildirim et al. 2007). Such a negative effect might lead to binder modification that was implemented to produce softer binder of the same performance grade of the virgin binder with enhanced fatigue resistance. This case might be different from the common practice that focuses on increasing the high temperature resistance in order to enhance the rutting resistance. Figure 4-9 also showed that the 12.5FC2 aggregate was more resistance to rutting than the 12.5 type in the case of total rut depth, and this observation was not readily evident with respect to the HWRT rut depth. The rutting rate was consistent with the total rut depth, as presented in Figure 4-9, and the high friction aggregate showed a lower level of total rutting depth. It has been observed that the binder content controls the rutting resistance of the mixes. As expected, mixes designed with the same aggregate and binder types with a higher level of binder content exhibited a 20 % to 58 % increase in rutting depth. In general, the HWRT results demonstrated that the binder (PG plus) modified to meet the LS 299 specification produced mixes with acceptable levels of rutting resistance, even if 0.5% was added to the optimum binder content.

The high friction aggregate positively affects HMA rutting resistance and this may be attributable to the rough surface texture of the aggregate which increases the stiffness. The extra 0.5% binder content reduces the internal friction and renders the mixes softer. Consequently, the rutting resistance is reduced. The aforementioned results promote incorporating stiffer binder types to overcome the lower rutting resistance associated with a smooth aggregate surface. In addition, the high friction aggregate may be used with the PG 64-28 in regions that suffer from severe HMA rutting.

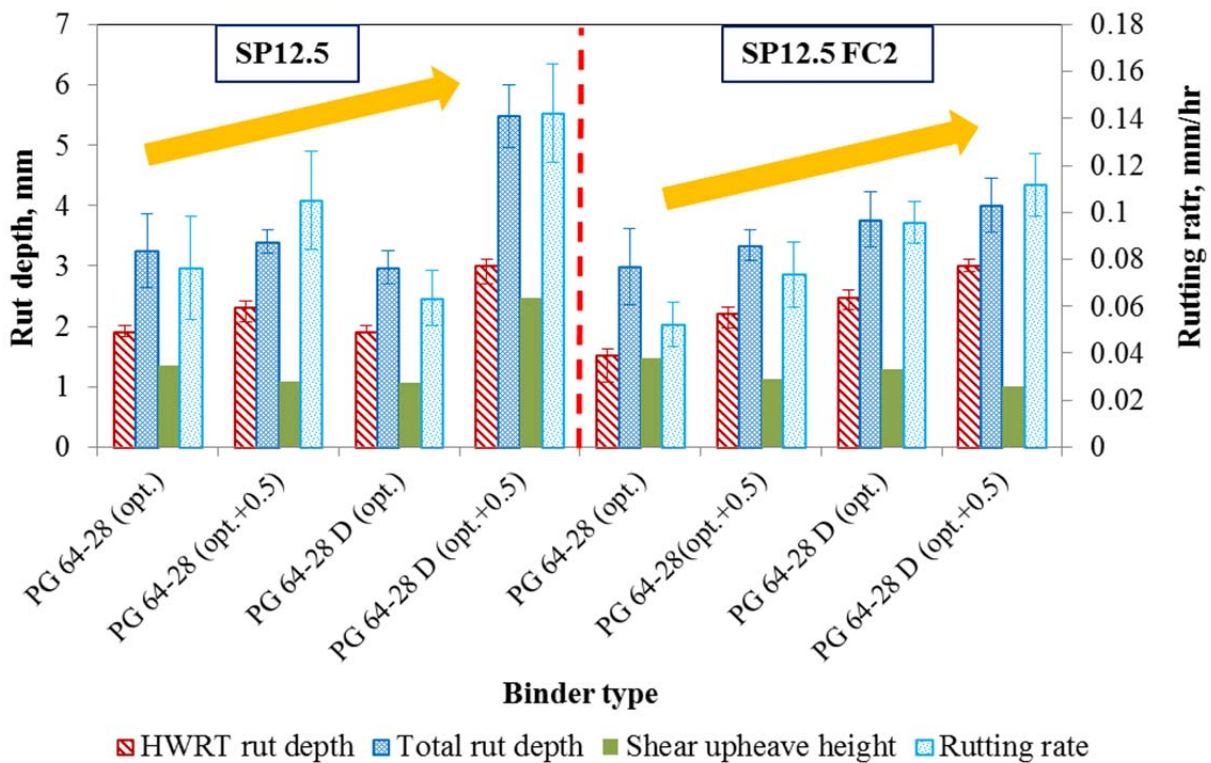


Figure 4-9 Rutting depths and rates for the HMA mixes

In addition, a full factorial two-level statistical analysis at a 95 % confidence interval was conducted with respect to the HWRT rut depth and rutting rate results, as shown in Tables 4-5 and 4-6, respectively. The analysis revealed that binder type and content were statistically significant. In contrast to its effect on HWRT rutting depth, aggregate type was shown to have a significant impact on the rutting rate of the HMA mixes. Aggregate interactions with binder content were statistically significant with respect to rutting resistance, as indicated in Table 4-5.

Table 4-5 Analysis of Variance for HWRT Rut Depth

Source	DF	Seq SS	Adj SS	Adj MS	F	P	S*
Main Effects	3	4.39	4.39	1.46	26.52	0.000	Yes
Aggregate	1	0.03	0.03	0.03	0.51	0.486	No
Binder Type	1	1.94	1.94	1.94	35.16	0.000	Yes
Binder Content	1	2.42	2.42	2.42	43.90	0.000	Yes
2-Way Interactions	3	0.58	0.58	0.19	3.50	0.040	Yes
Aggregate*Binder Type	1	0.29	0.29	0.29	5.35	0.034	Yes
Aggregate*Binder Content	1	0.09	0.09	0.09	1.70	0.211	No
Binder Type*Binder Content	1	0.19	0.19	0.19	3.46	0.081	No
3-Way Interactions	1	0.18	0.18	0.18	3.21	0.092	No
Aggregate*Binder Type*Binder Content	1	0.18	0.18	0.18	3.21	0.092	No
Residual Error	16	0.88	0.88	0.06			
Pure Error	16	0.88	0.88	0.06			
Total	23	6.02					

SS: sum of square DF: degree of freedom MS: mean of squares Adj: adjusted Seq: sequential
S*: significant

Table 4-6 Analysis of Variance for Rutting Rate

Source	DF	Seq SS	Adj SS	Adj MS	F	P	S*
Main Effects	3	0.0159	0.0159	0.0053	11.71	0.00	Yes
Aggregate	1	0.0033	0.0033	0.0033	7.21	0.016	Yes
Binder Type	1	0.0030	0.0030	0.0030	6.61	0.021	Yes
Binder Content	1	0.0096	0.0096	0.0096	21.27	0.00	Yes
2-Way Interactions	3	0.0023	0.0023	0.0008	1.69	0.209	No
Aggregate*Binder Type	1	0.0006	0.0006	0.0006	1.40	0.254	No
Aggregate*Binder Content	1	0.0011	0.0011	0.0011	2.50	0.133	No
Binder Type*Binder Content	1	0.0005	0.0005	0.0005	1.16	0.296	No
3-Way Interactions	1	0.0015	0.0015	0.0015	3.24	0.091	No
Aggregate*Binder Type*Binder Content	1	0.0015	0.0015	0.0015	3.24	0.091	No
Residual Error	16	0.0073	0.0073	0.0005			
Pure Error	16	0.0073	0.0073	0.0005			
Total	23	0.0269					

SS: sum of square DF: degree of freedom MS: mean of squares Adj: adjusted Seq: sequential
S*: significant

A multi-mean comparison of the rut depth measured according to the two methods discussed earlier is shown in Table 4-7. The Fisher least significant difference was used for ranking the mixes from highest to lowest rut depth (Leng et al. 2008). Four groups of HMA mixes with statistically equivalent levels of performance were obtained for both the total rut depth and the HWRT methods. However, it should be mentioned that, in both cases, the first group includes PG Plus with the additional 0.5% binder content, which exhibited the least satisfactory rutting performance compared to the other mixes. On the other hand, the modified binder with the high friction aggregate and the additional binder ranked second with respect to total rutting depth. This result was caused by the difference between the total rutting depth and the HWRT rut depth, which represents the shear upheave and which varied from 33 % to 82 %, with an overall value of 57 %. This finding demonstrates the impact of measuring shear flow on the evaluation of the rutting of the HMA, which would therefore have a significant impact on the correlation between rutting depths measured in the field and in the laboratory.

Table 4-7 Grouping Information for the Fisher Method Analysis

Mix Type	N	Mean	Grouping				Mean	Grouping				Difference, %
SP12.5 PG 64-28 D (opt.+0.5)	3	5.49	A				3.01	A				82.08
SP12.5FC2 PG 64-28 D (opt.+0.5)	3	4.01		B			3.01	A				33.37
SP12.5FC2 PG 64-28 D (opt.)	3	3.77		B	C		2.49		B			51.47
SP12.5 PG 64-28(opt.+0.5)	2	3.40		B	C	D	2.32		B			46.87
SP12.5FC2 PG 64-28(opt.+0.5)	3	3.34		B	C	D	2.21		B	C		51.28
SP12.5 PG 64-28 (opt.)	3	3.26			C	D	1.91			C	D	71.15
SP12.5 PG 64-28 D (opt.)	2	2.98			C	D	1.90			C	D	56.44
SP12.5FC2 PG 64-28 (opt.)	3	2.84				D	1.71				D	66.11

*Mixes sharing same letter are not significantly different ¹ Total rut depth ² HWRT rut depth

4.3.3 Comparison of Flow Numbers (FN)

The FN test was performed to enable observation of all deformation stages and to provide a better evaluation of the sensitivity of the HMA mix rutting to the mix variables. The actual test results and the FN calculation for one sample of the unmodified binder with the 12.5 FC2 and

SP12.5 aggregates are shown in Figure 4-10 (a) and 4-10 (b), respectively. Figure 4-10 (a) shows that the tertiary region was captured for the 12.5 FC2 mix, for which HWRT measurements showed the greatest rutting resistance. Visual observation reveals that the 12.5 mix had a higher flow rate and greater permanent strain than the 12.5 FC2 mix. Therefore, mixes made of high friction aggregate are expected to resist the permanent deformation under the repetitive wheel loads. The FN values for all HMA mixes, which were calculated using the same procedure, are presented in Figure 4-11. The data coefficients of variation (COV) levels adhere to the precision requirements outlined in AASHTO TP 62-07.

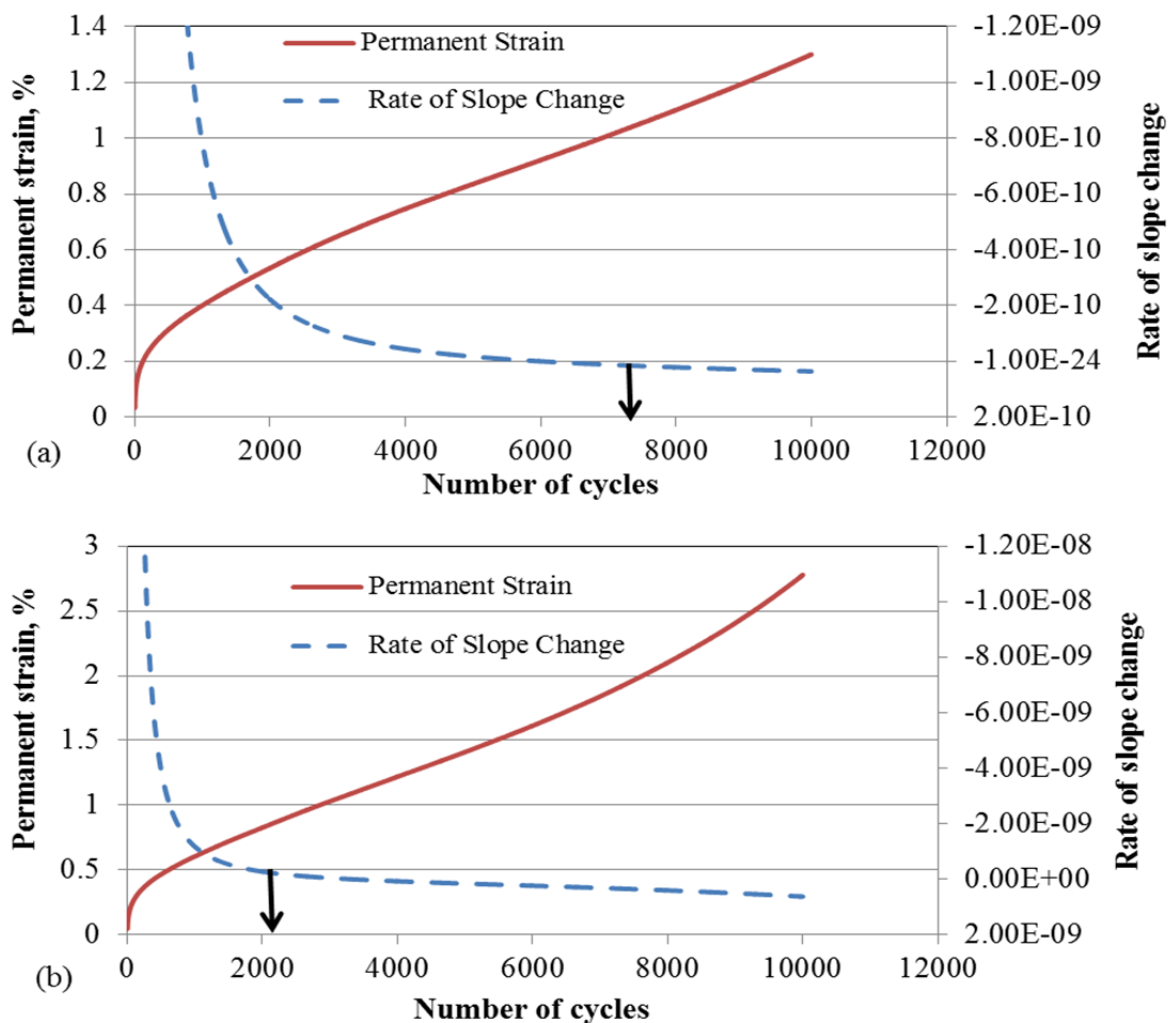


Figure 4-10 Accumulated permanent strain and rates of slope change: (a) SP12.5 FC2 PG 64-28; (b) SP 12.5 PG 64-28

As Figure 4-11 indicates, the SP12.5FC2 PG 64-28 mix exhibited the best performance. Overall, a rational trend exists between the HWRT and FN results except with respect to the SP12.5 PG 64-28 mix, in which changes may have been made in the dynamic modulus test since this mix had higher binder content and incorporated a binder with less stiffness. As a rutting resistance indicator, binder type and binder content had a negative effect on the FN. With respect to improving rutting resistance, the impact of the high friction aggregate was obvious. All mixes made of 12.5 FC2 exhibited superior rutting resistance compared to the same mixes made of 12.5, which the HWRT results failed to indicate.

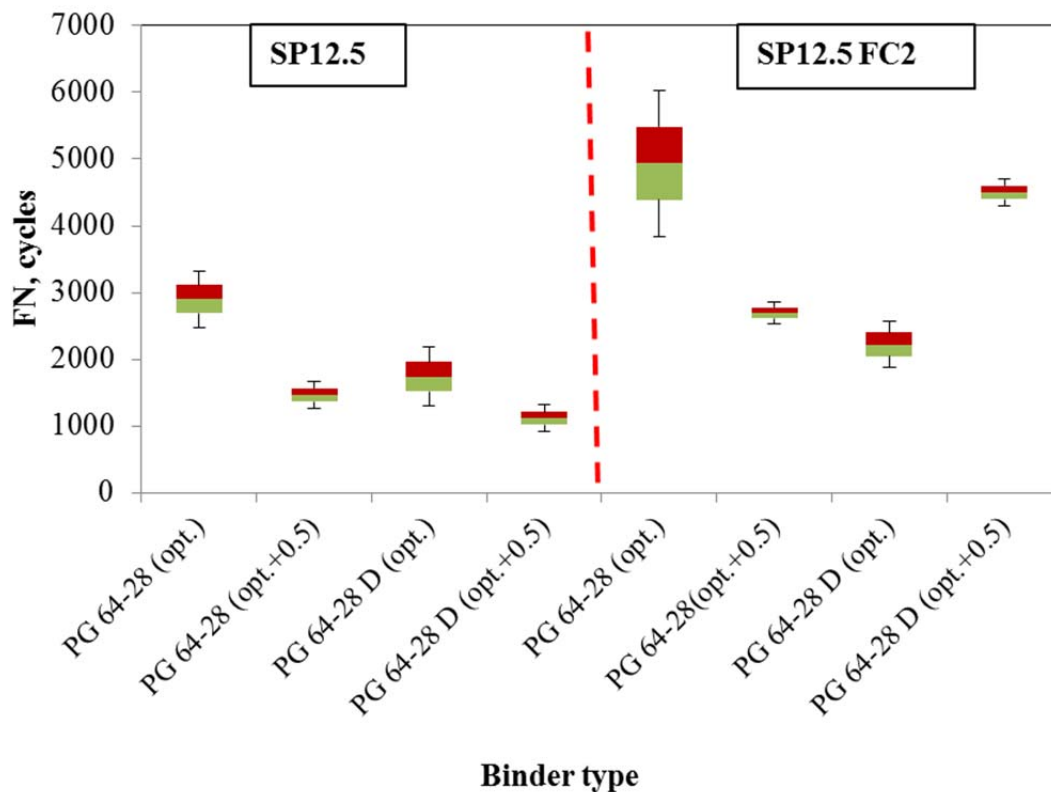


Figure 4-11 Boxplot for HMA mix flow numbers

4.4 Summary and Conclusions

This chapter has presented the results of the experimental work and the analysis that were conducted with the goal of improving HMA fatigue life without compromising rutting resistance or mix stiffness. The levels of fatigue resistance exhibited by Superpave™ mixes were investigated with respect to the use of these mixes as surface course materials. The effects of three key design variables and their interactions were quantified: aggregate type, binder type, and binder content. The methodology included four experimental tests: four-point bending, dynamic modulus, Hamburg Wheel Rut, and flow number. Two types of aggregate were examined: Superpave™ SP12.5 and high-friction SP12.5 FC2. A modified (PG Plus) and an unmodified binder were incorporated at both the optimum binder content and the optimum plus 0.5%.

The results revealed that the fatigue resistance, rutting resistance, and stiffness of HMA surface mixes were all sensitive to aggregate type, binder type, and binder content. A specific combination based on the positive effects of these variables can lead to the creation of superior fatigue resistance without a significant negative impact on the resistance of the mixture to other types of distress. The mix that produced the best fatigue performance incorporated regular 12.5 mm aggregate and PG Plus binder at the optimum binder content plus an additional 0.5%. The findings of this study could result in HMA design that mitigates fatigue cracking while maintaining a satisfactory degree of rutting resistance.

Chapter 5

Development of HMA Image-Based Analysis Frameworks

This chapter describes the development of three frameworks that were created to extend the use of image-based analysis for characterizing aggregate and hot mix asphalt (HMA). The goal was to enable visualization of the texture of the aggregate, 2D characterization of the internal structure, and the use of X-ray CT image processing for the quantification of air voids distribution and fatigue damage.

5.1 Demonstration of Aggregate Texture using SEM

Previous studies have shown that HMA cracking is initiated at the shortest pathway along the aggregate and mastic interfaces (Elseifi et al. 2008). This means that the aggregate interface, e.g., its frictional properties, is a very important parameter that may control crack initiation and propagation. HMA internal friction characteristics are dependent on numerous factors, such as aggregate textures, binder type, and coating thickness. Measuring friction is very challenging due to the complexity of aggregate texture. This texture can be expressed as fluctuations in pixel colour intensity in greyscale colors (Masad 2003). Some imaging methods can provide the ability to distinguish between aggregate angularity and texture (Sun et al. 2012). Image-based methods, such as SEM, that include different magnification levels offer a very high resolution for exploring complex aggregate textures.

To facilitate visual inspection, the surface textures of the aggregates were compared based on changes in the surface profile from peaks to valleys, along with their amplitudes, as presented in Figure 5-1. Figure 5-1 (a) shows the difference between the aggregate particle shape, texture, and angularity. It can be seen that examining aggregate texture may require very high magnification and resolution to facilitate good visualization, which was the reason for using SEM. Figures 5-1(b) and 5-1(c) illustrate the regular and irregular amplitudes of aggregate texture with very high resolution and indicate the divergence from the average lines visible with low-resolution imaging methods. With very high magnification methods, smooth and rough surfaces can thus be observed for regular and irregular amplitudes, respectively. Such

distinctions are not visible with lower resolution methods, as indicated by the dotted lines of the average amplitudes.

Figure 5-2 presents the original images of both the two-dimensional (2D) SEM and the three-dimensional (3D) visualizations of aggregate texture side by side. This figure shows that aggregate surface texture is generally characterized by a very complex geometry. The irregular shapes and the changes from peaks to valleys are more obvious in the 3D visualization of the aggregate than in the 2D SEM image. In the 3D views of the surface texture, spots with large and small wave amplitudes are designated as (L) and (S), respectively, whereas areas with regular or uniform amplitudes are designated as (U). This figure shows that the high friction 12.5FC2 aggregate (Figures 5-2 a and c) has more irregular amplitudes in surface texture than the 12.5 (Figures 5-2 b and d). However, more frequent peaks and valleys can be observed with the 12.5 than in 12.5FC2. The uniform surface amplitude of the 12.5 aggregate is clear in Figure 5-2 d.

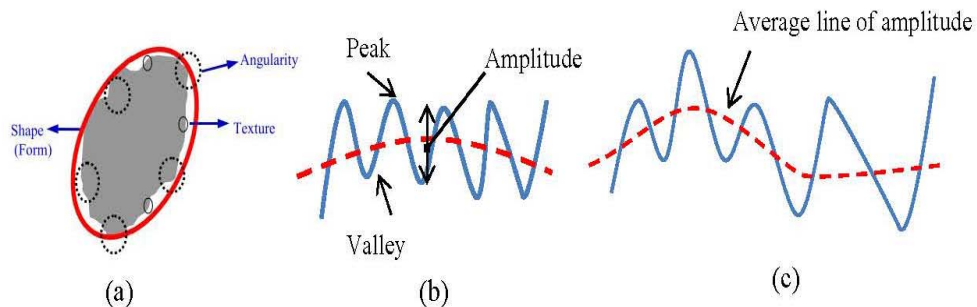


Figure 5-1 Illustrations of aggregate texture: (a) shape characteristics (Masad 2007); (b) regular amplitude; (c) irregular amplitude

5.2 2D Imaging Analysis Framework for the Mixtures Tested

Figure 5-3 shows the framework utilized for the internal structure analysis of the HWRT test samples. This involves the following three main steps: sample preparation, image acquisition and quality and image processing and analysis as described herein.

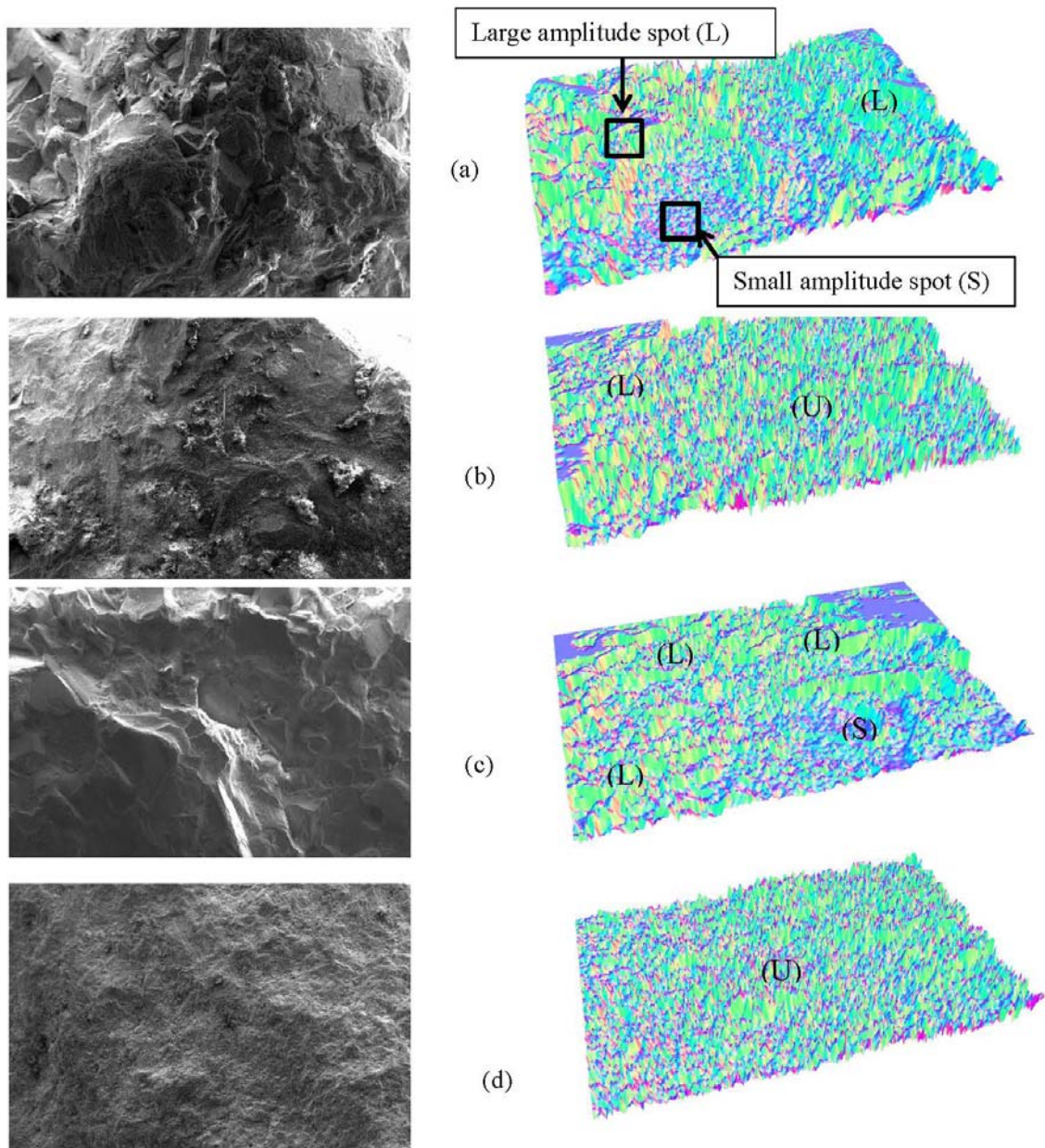


Figure 5-2 Aggregate texture for areas 2.3 mm wide (magnification = 50 X): (a) 4.75 mm 12.5FC2 aggregate; (b) 4.75 mm 12.5 aggregate; (c) 2.36 mm 12.5FC2 aggregate; (d) 2.36 mm 12.5 aggregate

5.2.1 Sample Preparation

The tested HWRT samples were cut vertically in the same direction and the location of the wheel path at three positions: one section at the centre and the other two sections at the sides of the rut depth. These locations were selected to fully evaluate the internal structure in the loaded area. To reduce variability in the analysis results, two samples were sawn to obtain six images for each mix. This number of images has been reported to be sufficient for producing valuable data that is quiet similar to the three dimensional sample properties (Sefidmazgi and Bahia 2014).

5.2.2 Image Acquisition and Quality

The cut faces were scanned using a scanner with a resolution of 600 dpi to meet the HMA images scanning protocol described by Coenen et al. (2012). Figure 5-4 shows an illustrative example of the acquired greyscale image histogram, which was captured at the middle section of the test sample for the SP12.5 PG 64-28 mix. The image was 150 mm long and 60 mm high. It can be observed that the HMA image pixels take wide range of possible intensities. Three regions of HMA microstructure composition (aggregate, mastic and air void) can be observed and separated. The aggregate thresholding level is obvious on the histogram, and thus verifies the quality of the image acquisition system.

5.2.3 Image Processing and Analysis

IPas2 software was used for image processing and analysis. All images were processed with a constant filtration level and a minimum aggregate size of 1.18 mm. The filtration level was chosen after numerous attempts to match the IPas2 input and output parameters and was verified by visual observation of the processed images. After completing image processing, three HMA internal structure indices (the number of aggregate contacts, the contact length and contact orientation angles) were calculated. The aggregate particles are considered in contact if the distance between them is less than a preselected distance (Partl et al. 2012; Sefidmazgi 2011). A distance of 0.1mm was used in the analysis. More details regarding the software validation and analysis procedure in IPas2 can be found in Coenen et al. (2012).

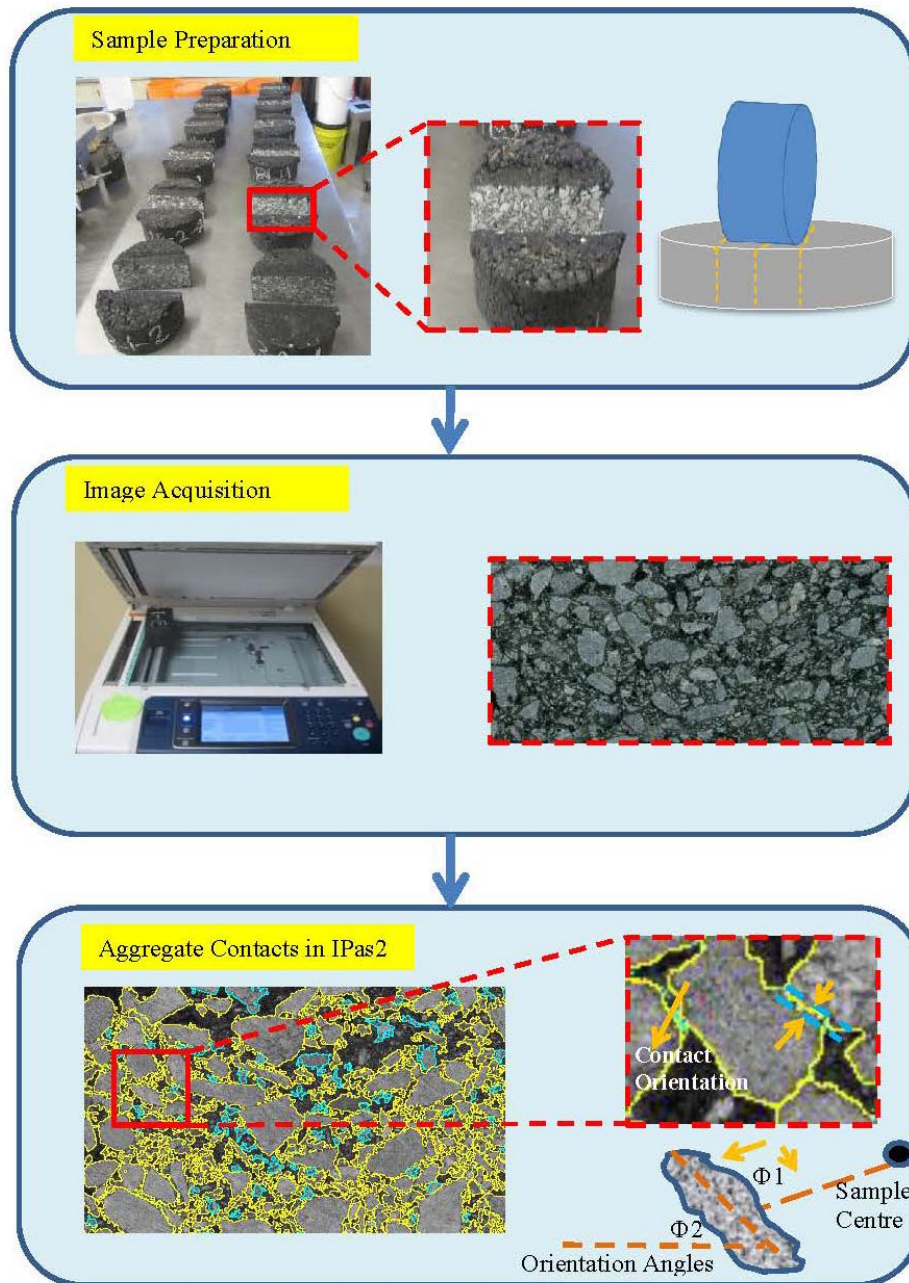


Figure 5-3 Image preparation and processing methodology

The numbers of contacts and the contact lengths have been corrected according to the aggregate surface area to ensure that the contacts of particles smaller than 1.18 mm are included in the results. The third index, i.e., internal structure index (ISI), is then calculated using the contact

orientation and contact length (Sefidmazgi et al. 2012). The acquired images on the rut side sections are smaller to the middle section image. Therefore, the results were normalized in order to achieve consistency among images from the middle rut section.

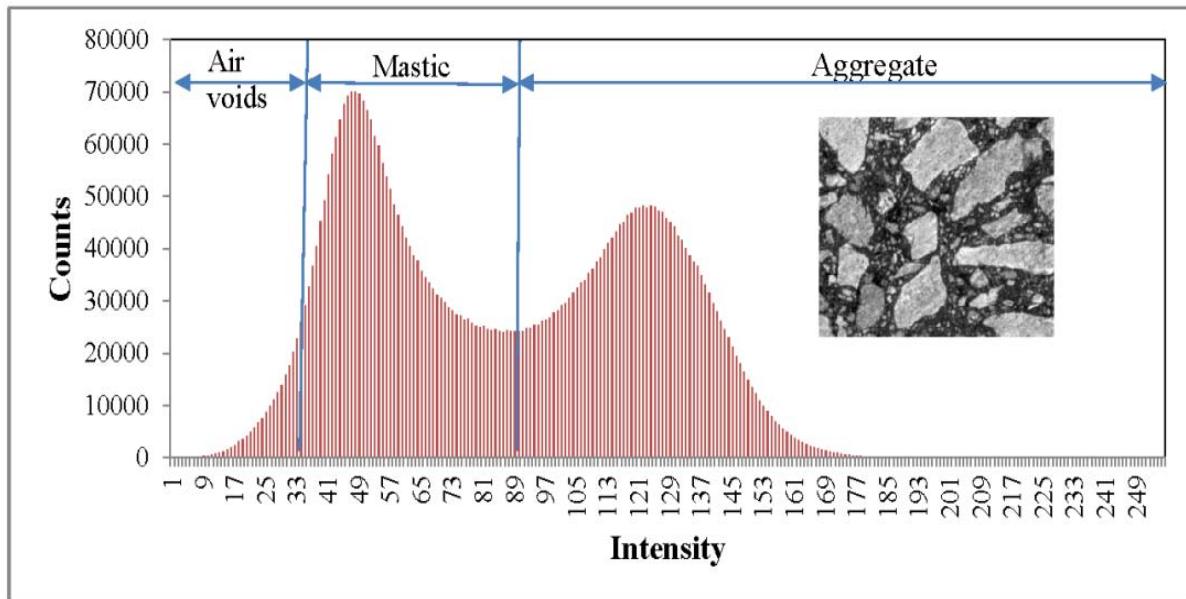


Figure 5-4 HMA image histogram of the test sample at middle section

5.3 Establishment of Framework to Quantify Fatigue Damage

The X-ray CT was used in this study to directly capture the damage that occurs in the HMA beams test using the four-point bending test. This section explains a new developed scheme to process and analysis images acquired before and after asphalt beam being subjected to four-point bending fatigue.

5.3.1 Thresholding for Air Voids and Damage

In an asphalt mixture, three thresholding (T) levels are required for the identification of the air voids, mastic, and aggregate, as can be seen in Figure 5-5. These levels may be selected visually, which is more difficult with 3D image analysis. Standard methods for finding thresholding levels

are needed. Air void thresholding levels are established by minimizing the error between the measured air voids as determined from laboratory testing and the processed images (Zeleeuw and Papagiannakis 2007a; Zeleeuw et al. 2008). Similarly, this approach has been used by (Elseifi et al. 2011) for the quantification of the damage to tested specimens after a flow test. This method is inappropriate in the case of viscoelastic damage, which does not always create damage in the form of air voids. To the best of the authors' knowledge, no method has yet been developed for determining thresholding values in tested samples. This work therefore represents a first step toward the detection of fatigue damage in asphalt beams.

5.3.2 Development of the Analysis Algorithm

The primary contribution of this analysis is twofold. First, thresholding levels of the tested specimens have been calculated based on the greyscale levels of the aggregate. The colour of the aggregate is unchanged by the testing. The changes occur in the voids or the mastic due to damage during the test but are not reflected in the aggregate particles. Second, the proposed algorithm employs a wide range of colour intensities. The images were analyzed in 16-bit greyscale colour intensities (0 to 65,535) rather than with the common methodology that uses 8-bit greyscale colour (0 to 255). This method is more appropriate for asphalt mixes, especially with respect to damage quantification, because it offers the possibility of detecting any small variations in colour intensities that occur during the testing. To provide additional insight about the importance of the range of image colour intensity, 8-bit and 16-bit histograms were compared. Figure 5-5 shows asphalt histograms for one image slice from the beam at both greyscales. The thresholding levels were determined from both histograms in order to achieve a target air void of 7 %. The air voids were found to be 7.0 % at a greyscale level of 5923 from the 16-bit histogram and 6.72 % at 43 from the 8-bit histogram. Increasing the thresholding only two levels in each case produces increases in the air voids of 0.28 % and 17.41 % for the 16-bit and 8-bit analyses, respectively. The small changes in the first case confirm the accuracy in the 16-bit image analysis. This method can thus be recommended for capturing changes that occur in the microstructure of asphalt mixtures, particularly with fatigue damage.

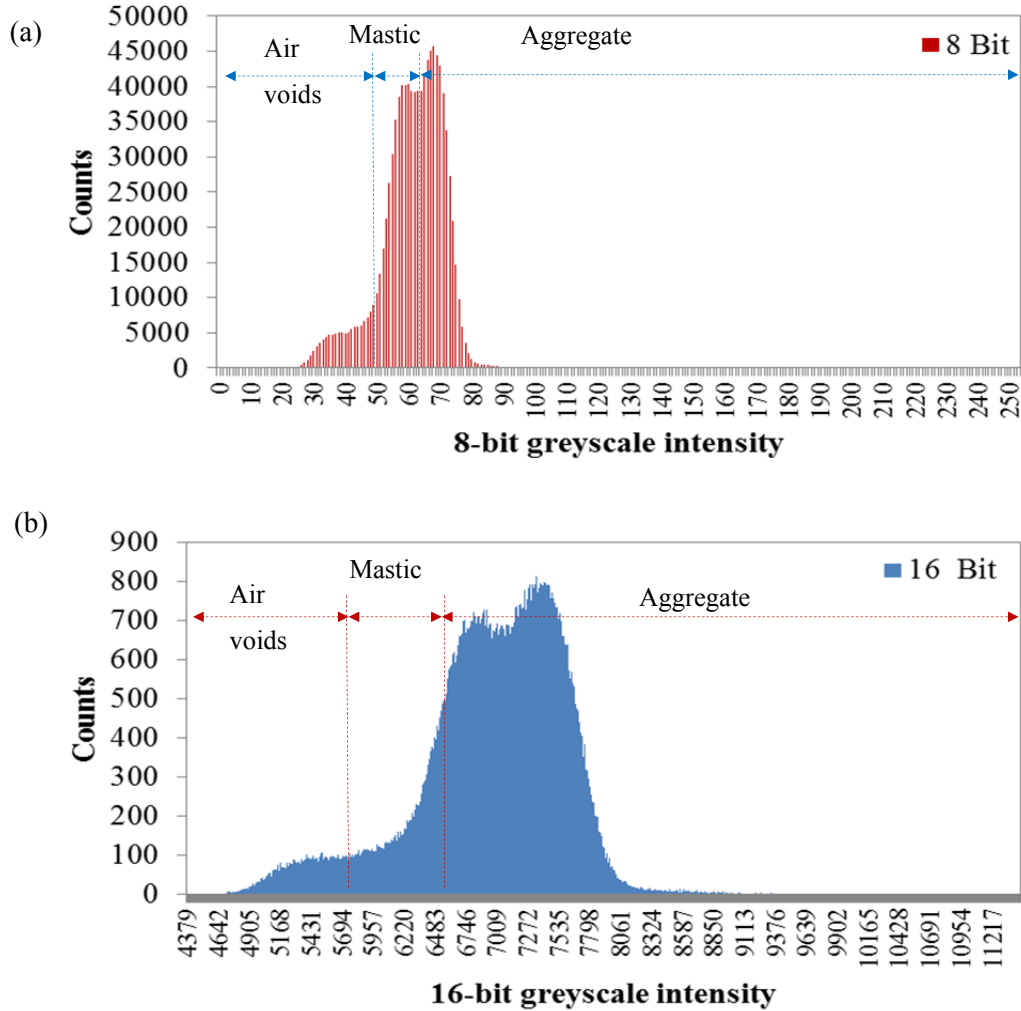


Figure 5-5 Image histograms: (a) 8 bit images, (b) 16 bit images

5.3.3 Scanning and Analysis Framework

Figure 5-6 illustrates the scanning and processing framework for quantifying asphalt damage. Prior to scanning, the air voids in the compacted beam are determined in the laboratory (V_{a-lab}). As explained earlier, the asphalt beam is scanned before the test, the 3D image view is constructed, and the histogram image is exported. In this case, the histogram represents the frequencies of the image voxels in the 16-bit greyscale. The asphalt beam is then tested using the

four-point bending. The same steps are applied to obtain the 3D image view and the histogram for the same beam after the test. The histograms of both cases are used to determine the thresholding levels based on the algorithm that was developed using Matlab. The proposed algorithm seeks two thresholds levels. The first level for the image histogram before the test (T_{before}) is the greyscale level at which the air void volume based on the images ($V_{\text{a-image}}$) is equal to the air voids as measured in the laboratory ($V_{\text{a-lab}}$). The second thresholding level for the image histogram after the test (T_{after}) is the greyscale level that indicates the air voids plus the damage induced during the test. The algorithm is divided into three main parts.

Part 1:

To find T_{before} , the following steps are implemented:

- Calculate the volume of the specimen in voxels, which is the sum of the voxel counts in the histogram data.
- Assume $T_{\text{initial}} = 1$ and then sum the voxel counts ($V_{\text{a-image}}$) if $T < T_{\text{initial}}$.
- Calculate the air void percentage from the $V_{\text{a-image}}$ percentage and compare it to the $V_{\text{a-lab}}$ percentage.
- If $V_{\text{a-image}} < V_{\text{a-lab}}$, increase the T value by 1 and repeat the previous steps; otherwise $T_{\text{before}} = T_{\text{initial}}$.

Part 2:

The portion of the pre-test image histogram that identifies the aggregate located at the end of the histogram where the lighter intensity voxels are found. This portion starts at the aggregate greyscale level (T_{agg}) that produces the percentage of the aggregate from the image ($V_{\text{agg-image}}$) equal to the percentage in the mixture ($V_{\text{agg-mix}}$). In this study, the value of $V_{\text{agg-mix}}$ is assumed to be 85 %. The T_{agg} that achieves a value of $V_{\text{agg-image}}$ equal to that of $V_{\text{agg-mix}}$ was calculated using the procedure followed in part 1.

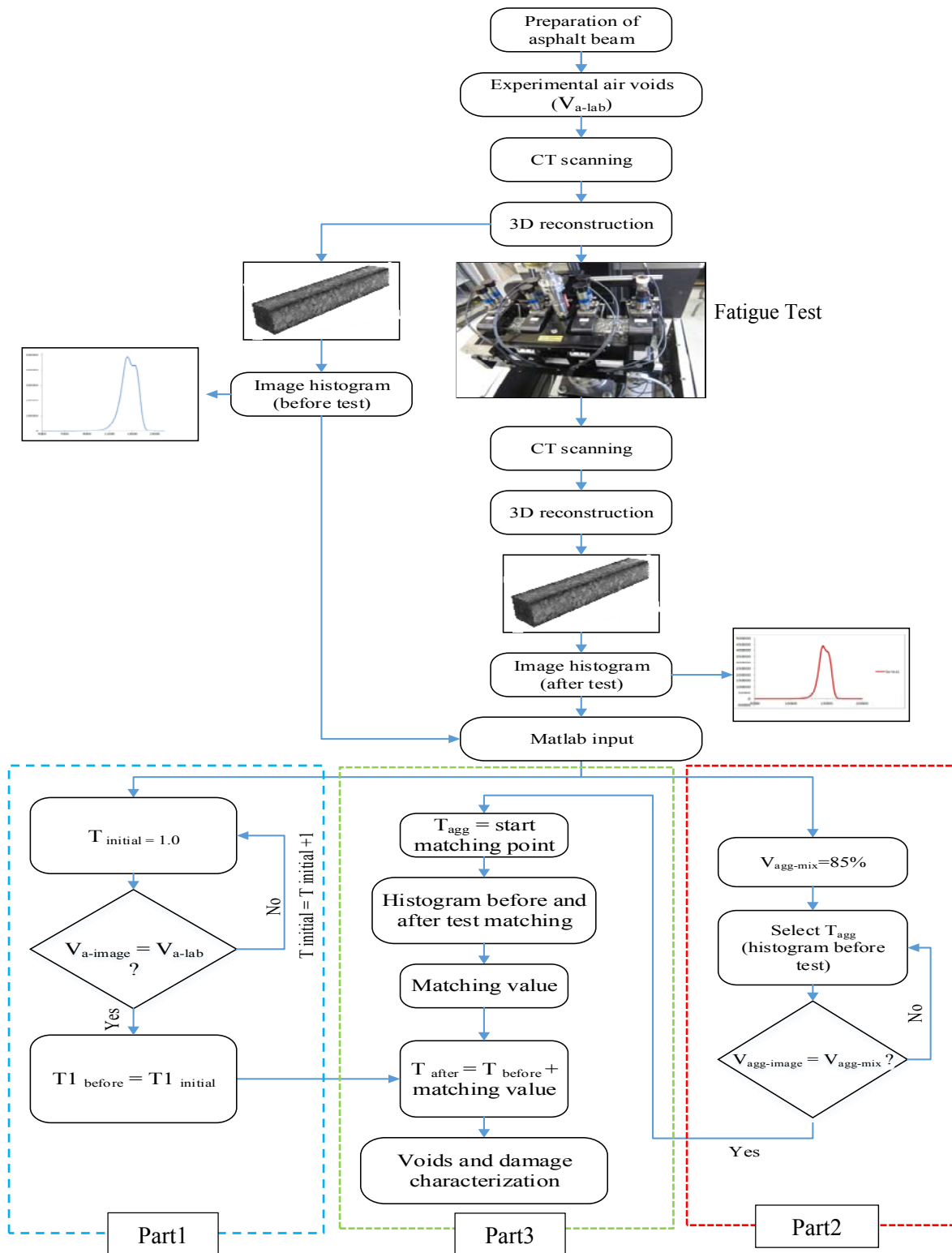


Figure 5-6 Scanning process and analysis framework

Part 3:

In this part of the algorithm, the two portions of the histograms that represent the aggregate are matched. Figure 5-7 indicates the steps followed in the matching process. The two histograms prior to the matching process are shown in Figure 5-7 (a). It can be noted that the histograms have shifted but that the distributions are similar. The idea is to shift one of the two histograms horizontally so that the error in the matching is minimal. Using Equation (14), the error is calculated only for the matched portion that represents the aggregate particles, as can be seen in Figure 5-7 (b). The location of the minimum error is identified and considered to be the best match location, as shown in Figure 5-7 (c). The difference in the greyscale level between this location and the original location is called the match value. This value is added to T_{before} in order to determine T_{after} .

$$\text{Error} = \sqrt{\frac{1}{n} \sum_{i=Tagg}^{i=65535} (Count_{\text{before}} - Count_{\text{after}})^2} \quad (14)$$

Where

n = the number of the matched point

$Count_{\text{before}}$ = the frequency of the colour with intensity i from the first histogram

$Count_{\text{after}}$ = the frequency of the colour with intensity i from the second histogram

Based on the values for T_{before} and T_{after} , VG Studio software is used for processing the image and analyzing the voids before and after testing.

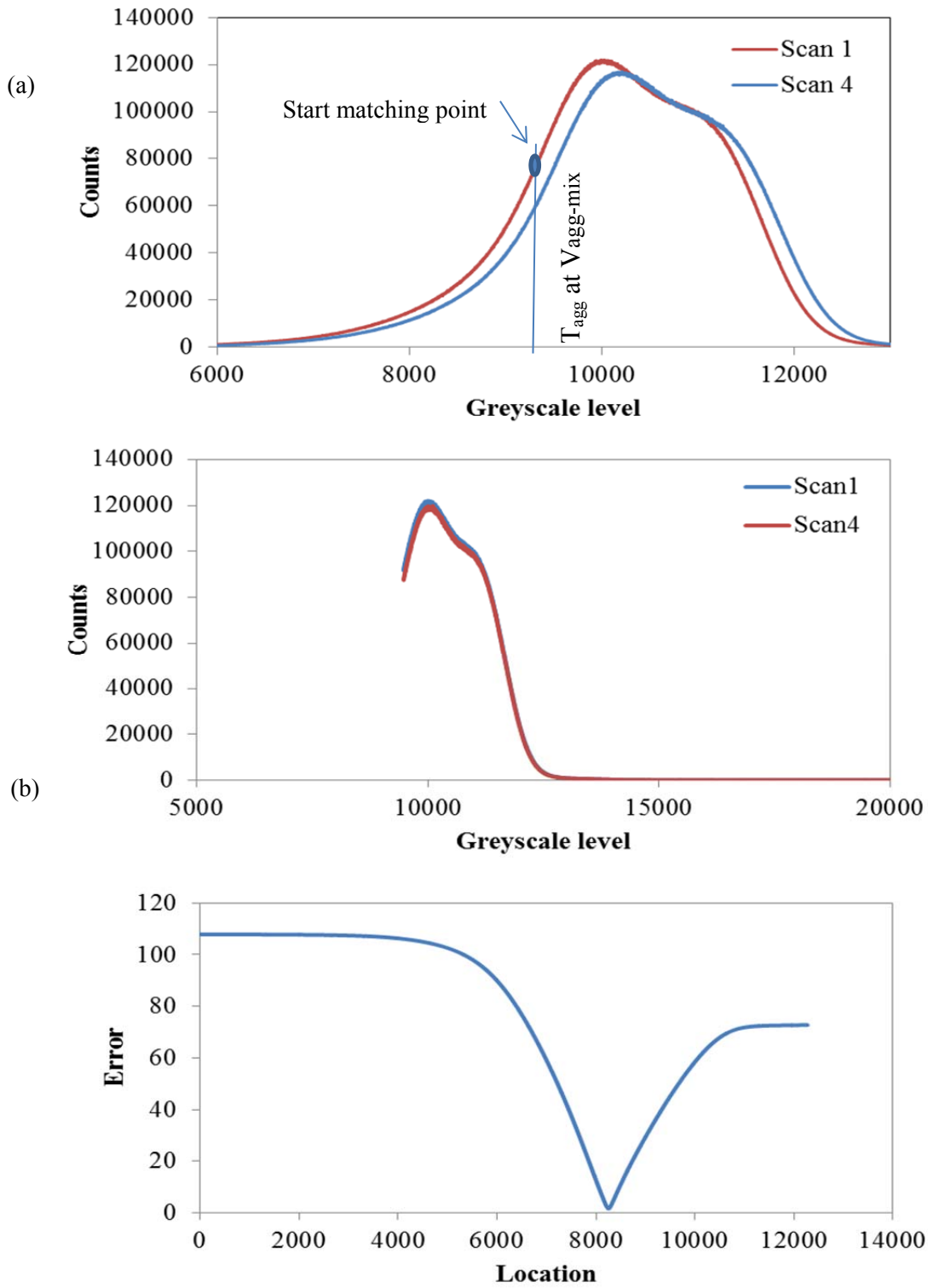


Figure 5-7 Matching of two histograms: (a) two histograms before matching; (b) matched parts; (c) error in the matching of the two histograms

5.4 Summary and Conclusions

This chapter has presented three frameworks that were developed as a means of providing enhanced image-based HMA analysis. The first framework employs an SEM tool for visualizing and comparing aggregate texture based on scans of three aggregate particles. Aggregate texture is compared based on the variations in the colour intensity of greyscale images, with the amplitude of the changes from peaks to valleys as the basis of comparison. When very pronounced variations in amplitude are observed (e.g., S to L), the texture is defined as rough. Small variations in colour amplitude, expressed as U, are considered as indicators of a smooth surface. The second framework was created in order to estimate three internal structural indices for the 2D images of the HWRT specimens. This method compares the packing characteristics of the mixtures comprised of various combinations of aggregate and binder types as well as binder content. The three indices are the number of contacts, the total contact length, and the ISI. The third framework utilizes X-ray CT results for evaluating the amount of HMA damage that has occurred in the asphalt beam during the fatigue test. A new technique has been developed for quantifying the damage based on the processing of the images collected prior to and following the four-point bending tests. This technique incorporates the colour intensities of 16-bit images of the aggregate in order to statistically match the histograms, thus enabling a determination of the post-testing thresholding levels of the images.

Chapter 6

Image-Based HMA Characterization Results and Discussion

This chapter presents the analysis that was carried out using the frameworks that were developed in Chapter 5. The results and discussion relate to 2D imaging techniques for characterizing aggregate texture and the internal structure of hot mix asphalt (HMA). The analysis also includes the results of case studies that were conducted with the goal of using the X-ray CT imaging system in order to identify air void distribution and damage in HMA asphalt test beams. To capture microstructural changes, images were collected both before and after four-point bending fatigue tests.

6.1 Comparison of Aggregate Texture

To facilitate a precise evaluation, for both the high friction 12.5FC2 and the 12.5 aggregates, 3D visualizations of the surface texture were acquired for three random spots for both the 4.75 mm and 2.36 mm sized aggregate particles. Six images were obtained for the 9.5 mm aggregate size in order to achieve a solid assessment of the aggregate texture. The images are presented in Figures 6-1 and 6-2, which shows 3D views of the SEM images obtained at a 1000 times magnification for an area with 114.4 μm widths. Higher magnification enables a very large number of waves to be observed in a very small area of aggregate surface.

The high friction 12.5FC2 aggregate showed an irregularly shaped texture. Figures 6-1(a), 6-1(c), and 6-2(a) depict changes in texture amplitude from (S) to (L) amplitudes for the high friction aggregate. In contrast, the amplitude of the texture waves in Figures 6-1(b), 6-1(d), and 6-2(b) are uniform, with very slight changes in the (S) to (L) amplitudes in very small spots. Aggregate surface characteristics, such as texture and angularity, influence the HMA internal friction and packing, thereby impacting the binder film thickness. As indicated from the results, the 12.5 aggregate provides a uniform surface texture that would produce a uniform binder film thickness, which affects the aggregate particle contacts as well as the stress distribution in the HMA mixes. The high friction aggregate provides a better aggregate interlock but creates a coating thickness that is too thin or thick due to the irregular shape of the texture, which would

result in stiffer mixes. Therefore, the 12.5 aggregate was expected to produce mixes with less stiffness than the high friction 12.5 aggregate, which mitigates cracking.

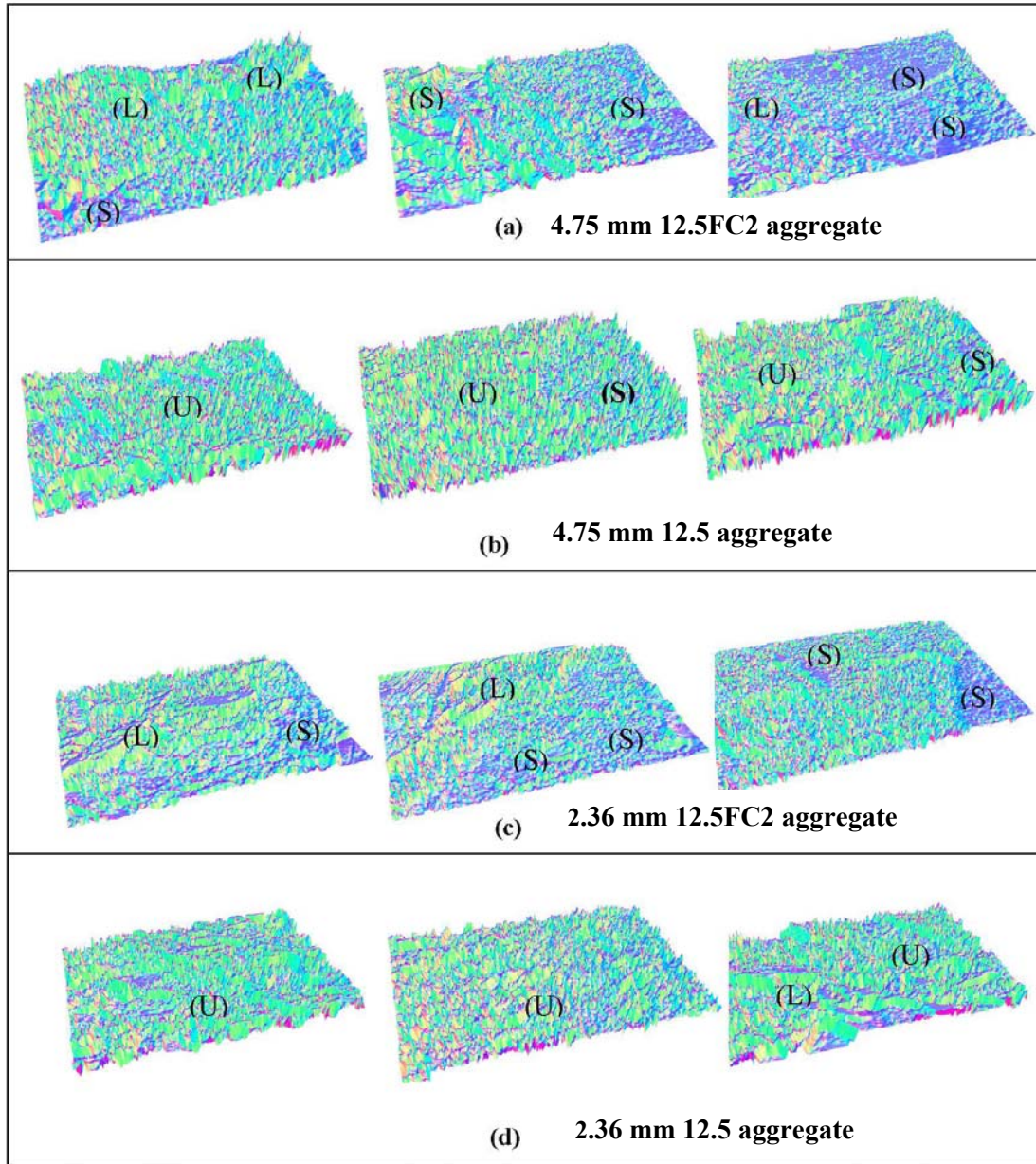


**Figure 6-1 Three-dimensional visualization of aggregate texture for 114.4 μm wide samples
(magnification = 1000 X)**

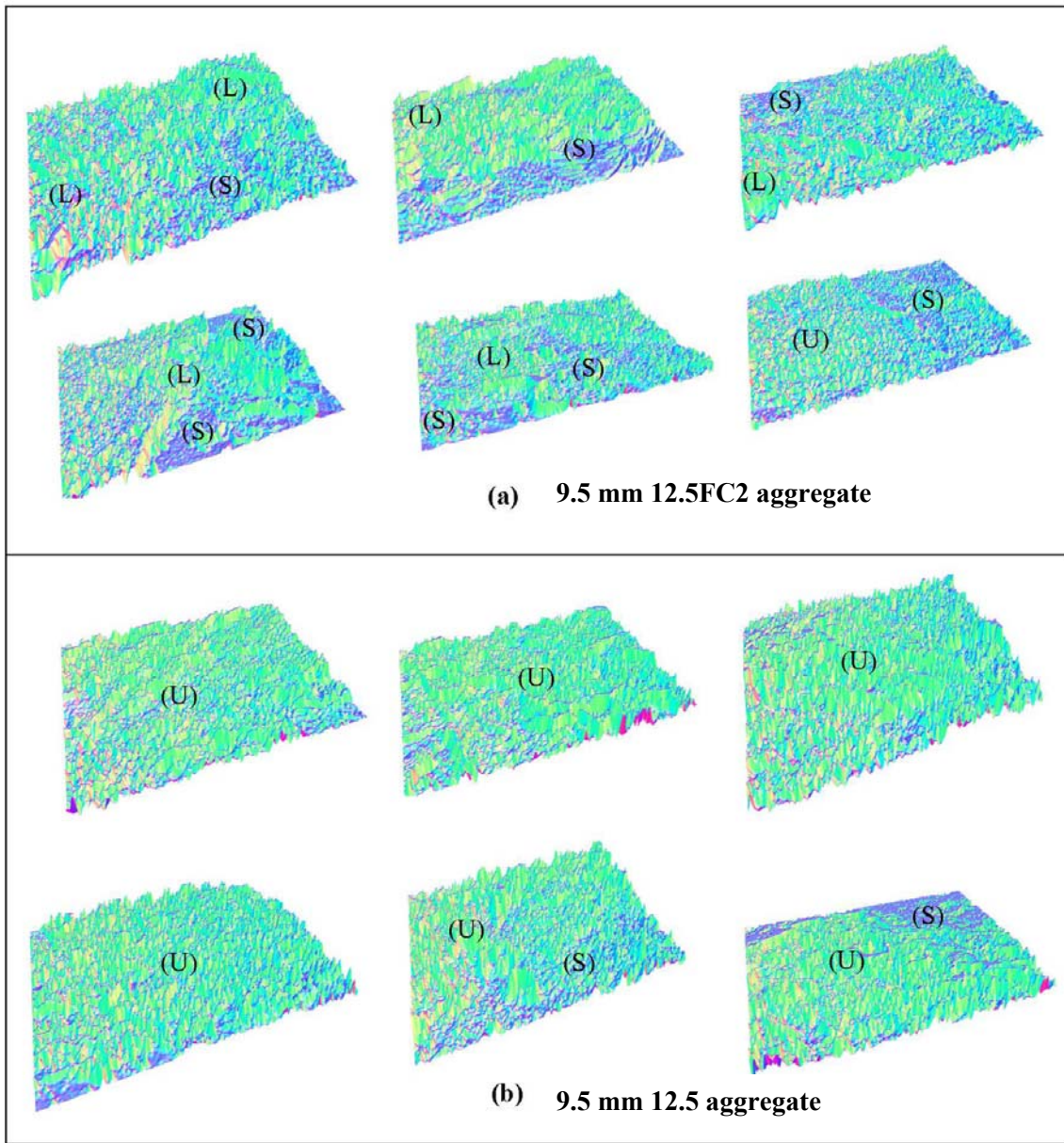


Figure 6-2 Three-dimensional visualization of aggregate texture for 114.4 μm wide samples
(magnification = 1000 X)

6.2 2D Internal structure analysis of HMA

The internal structures of the eight mixes used in this study were analyzed in order to provide an advanced evaluation of the effect of aggregate type, binder type, and binder content on rutting resistance. The aggregate-to-aggregate contacts in the compacted samples constitute one factor that affects permanent deformation. In addition to deformation, this factor also has an impact on HMA internal resistance and stress distribution. The numbers representing the contact zone, the total contact length, and the ISI for each mix are shown in Figure 6-3. Similar trends were observed with respect to all three Internal Structure Indices (ISIs) measured.

These data were computed for the aggregate skeleton, which refers to the aggregate particles that are in contact from the top to the bottom of the asphalt images (Sefidmazgi et al. 2012). This method seems to be more relevant to stress distribution than the total number of aggregate particles contacts in the mixture. In general, the image-based characteristics were consistent with the laboratory test results. It is clear from Figure 6-3 that the indices computed decrease with increases in binder content. This effect is not surprising due to the associated increase in the thickness of the aggregate coating. The number of contacts in the high friction aggregate 12.5 FC2 mixes was greater than in the 12.5 mixes, which may be related to the rough surface of this aggregate and the consequent increase in surface area.

Statistical analysis of the three indices measured was performed at 0.05 significance levels as shown in Tables 6-1. The analysis of the total contact length and Internal Structure Index (ISI) of the aggregates revealed that the effect of the aggregate was statistically significant. The number of contacts was an accurate gauge of the effect of the binder content on HMA rutting. The results confirm the important role of the aggregate and binder interaction in providing more stable HMA mixes, especially for high friction aggregates. When images processed with constant parameters, a change in the microstructure response was an effective indicator of a shift in HMA performance

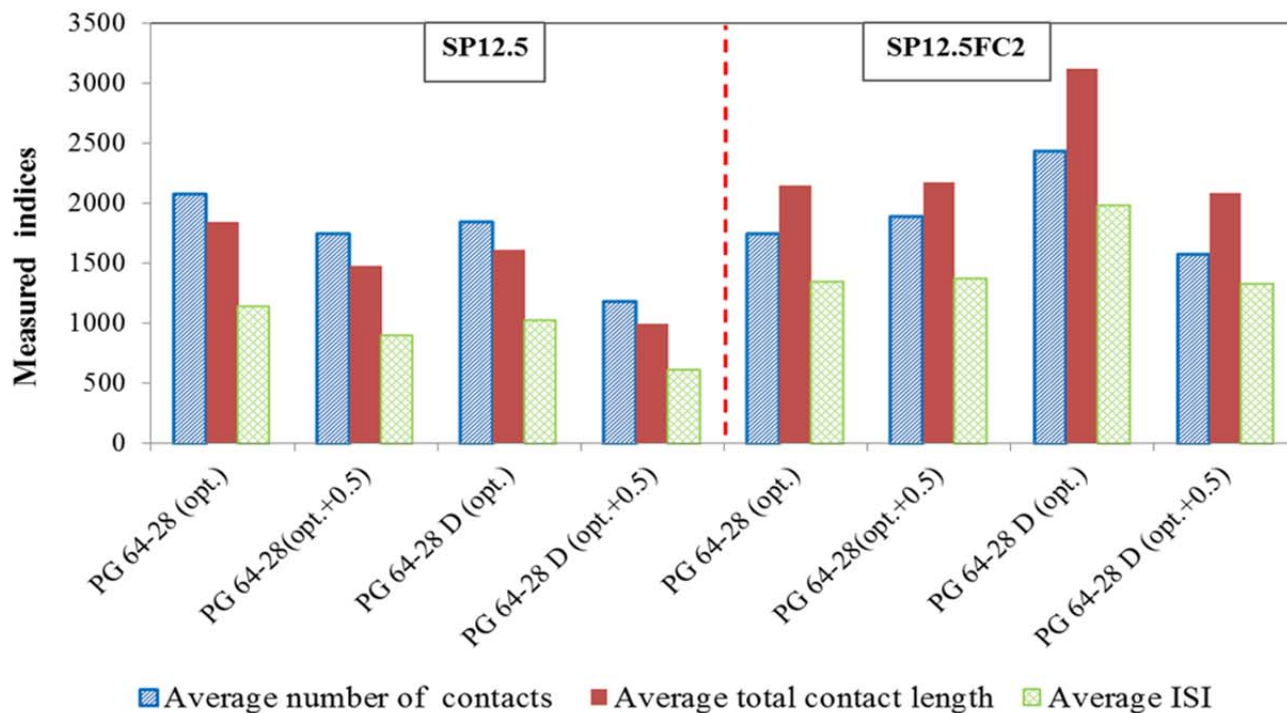


Figure 6-3 Number of contacts between aggregate particles in HMA mixes

Table 6-1 Analysis of Variance for Number of Contacts

Source	DF	Seq SS	Adj SS	Adj MS	F	P	S*
Main Effects	3	6153952	6153952	2051317	6.70	0.001	Yes
Aggregate	1	1638725	1638725	1638725	5.35	0.026	Yes
Binder Type	1	14235	14235	14235	0.05	0.83	No
Binder Content	1	4500992	4500992	4500992	14.70	0.000	Yes
2-Way Interactions	3	1608436	1608436	536145	1.75	0.172	No
Aggregate*Binder Type	1	560109	560109	560109	1.83	0.184	No
Aggregate*Binder Content	1	108303	108303	108303	0.35	0.555	No
Binder Type*Binder Content	1	940024	940024	940024	3.07	0.087	No
3-Way Interactions	1	674374	674374	674374	2.20	0.146	No
Aggregate*Binder Type*Binder Content	1	674374	674374	674374	2.20	0.146	No
Residual Error	40	12246949	12246949	306174			
Pure Error	40	12246949	12246949	306174			
Total	47	20683712					

SS: sum of square DF: degree of freedom MS: mean of squares Adj: adjusted Seq: sequential
S*: significant

6.3 HMA Fatigue Damage

6.4 Validation of the Proposed Framework

Figure 6-4 (a) shows 3D views of a 90 mm length of the asphalt beam. Aggregate, mastic, and air voids are three microstructure components visually distinguishable in the images. The lighter colours of the aggregate appear in contrast to the darker areas that represent the mastic and air voids. The heterogeneous distribution of the air voids is evident in Figure 6-4 (b). The 3D view reveals the importance of using X-ray CT as a tool for HMA characterization because of the unique visualization and characterization it provides.

The specimen displayed in Figure 6-4 was scanned four times for use in the verification of the developed algorithm. A 3D view of each scan was constructed, and a 16-bit image histogram was obtained. Figure 6-5 shows the histograms of the colour intensities for the four scans. It can be noted that the distributions in all scans are similar but are shifted by different values. Compared to Scan 1, Scan 4 has the largest shift value. The air voids calculated from the four scans are expected to have the same values and distributions since they were obtained for the same specimen. To verify the developed algorithm, thresholding levels were identified for each scan using two methods. In the first method, the calculation of the values resulted in 7 % air voids. With the second method, the developed algorithm was used in order to match the Scan 1 histogram with those of the other three scans as a means of determining the match value and the thresholding values, as discussed in the previous section. The thresholding values computed were then used for processing the images and calculating the air voids. Table 6-2 lists the values obtained by the two methods along with the percentage of error and air void. The error values were less than 1 % for all scans, which is attributable to the use of the 16-bit colour range. The air void values vary from 6.49 % to 6.96 %, which can be considered only a slight variation from the actual air voids (7 %). These results are indicative of the accuracy of the developed algorithm for calculating the thresholding values.

Another method of validating the proposed algorithm is through voids characterization. The air voids obtained at the T value were characterized using two methods. First, the specimen was sliced every 0.1 mm; a sample slice is shown in Figure 6-6. Image J software was used in

order to calculate the total area of the voids in each image slice, which was then divided by the total area of the image to determine the air void percentage. All image slices were processed using the same method, and the air void distributions and specimen lengths are shown in Figure 6-7. It can be seen that the air void distributions for the four scans are almost the same with respect to shape and value; no clear differences are evident. This finding can also be considered a good indication of the repeatability of the results. Second, VG studio software (VGStudio 2013) was employed for the calculation of the volumes and distributions of the void particles. Figure 6-8 provides 3D views of the air void particles for all scans. Scanning the same specimen more than once and using the developed algorithm to find the T values produced similar 3D views for the voids. The same effect can be observed from a comparison of the distributions of the volumes given in Figure 6-9. Only slight discrepancies are evident between the volumes and frequencies of the voids.

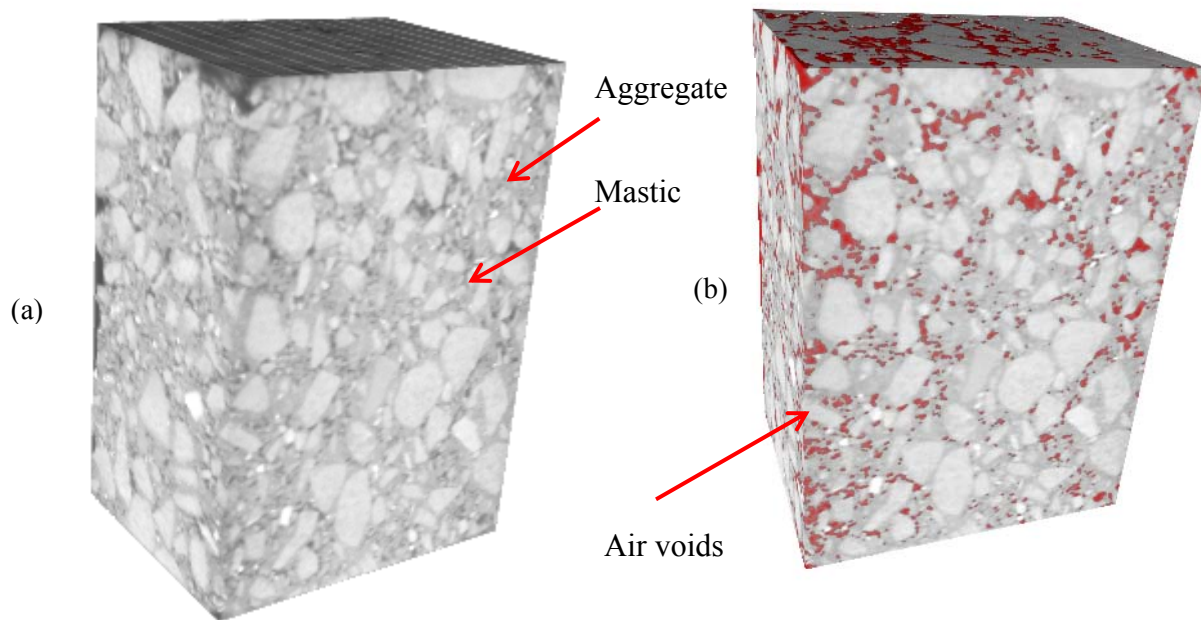


Figure 6-4 3D views of 90 mm of an asphalt beam: (a) 3D microstructure (b) 3D air void distribution

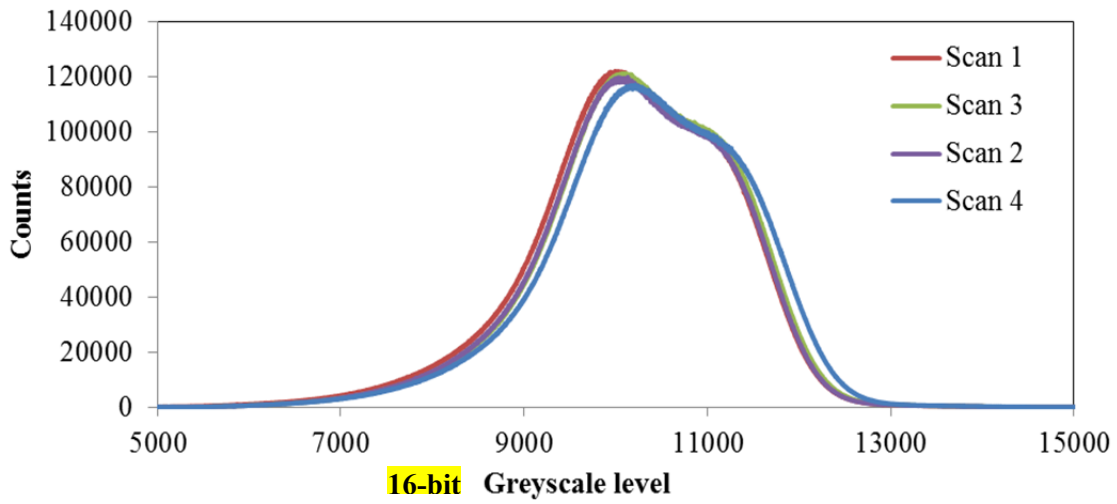


Figure 6-5 Image histograms of four scans for the same specimen

Table 6-2 Validation of Analysis

Scan	T ¹ at 7%	T ²	Error, %	Air Voids
Scan 1	8503	8503	NA	7.00
Scan 2	8615	8538	0.89	6.58
Scan 3	8641	8566	0.87	6.49
Scan 4	8708	8678	0.34	6.96

1: Thresholding at V-lab = 7% 2: Thresholding calculated from the developed algorithm

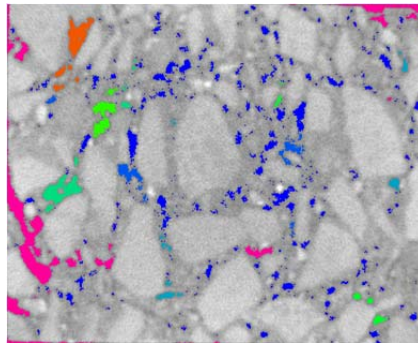


Figure 6-6 Air voids in a sample image slice

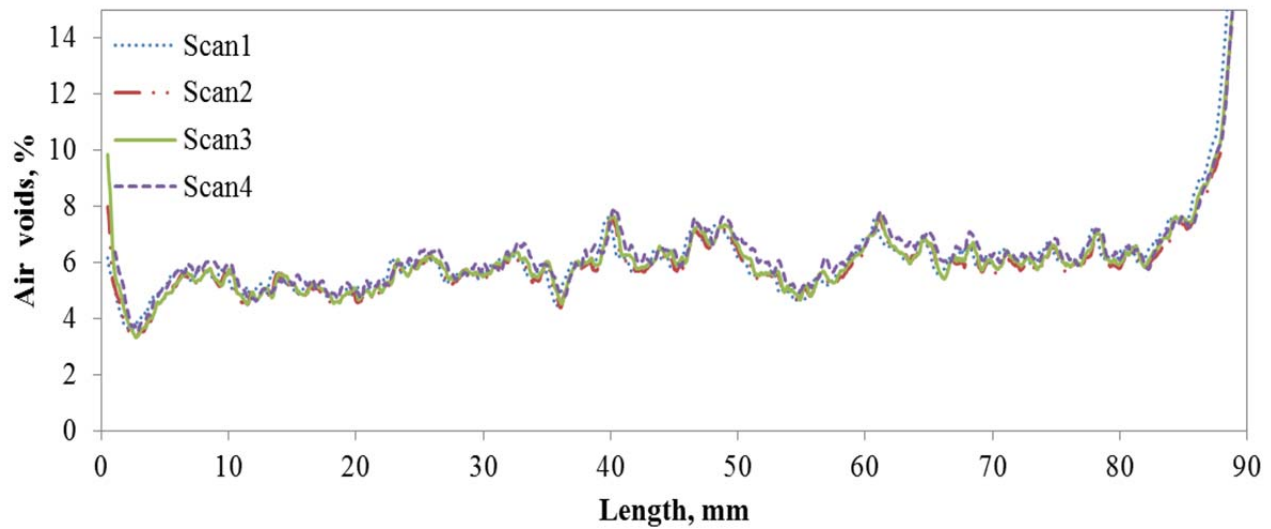


Figure 6-7 Air void distributions for four scans of the same specimen

These results and discussion indicate that the proposed algorithm is suitable, with no additional damage or changes in the voids when the same asphalt specimen is examined more than once. Similar distributions of light intensity were obtained for different scans with shifts due to the X-ray calibration process. Applying the developed algorithm to establish the thresholding limits has also been validated based on a comparison of the thresholding values and the air void characterization. The accuracy of the matching process using this methodology can be attributed to the use of 16-bit histograms and the incorporation of the aggregate intensities as a large constituent factor in the analysis. When the same sample is scanned before and after testing, any changes can therefore be ascribed to damage that occurred during the test.

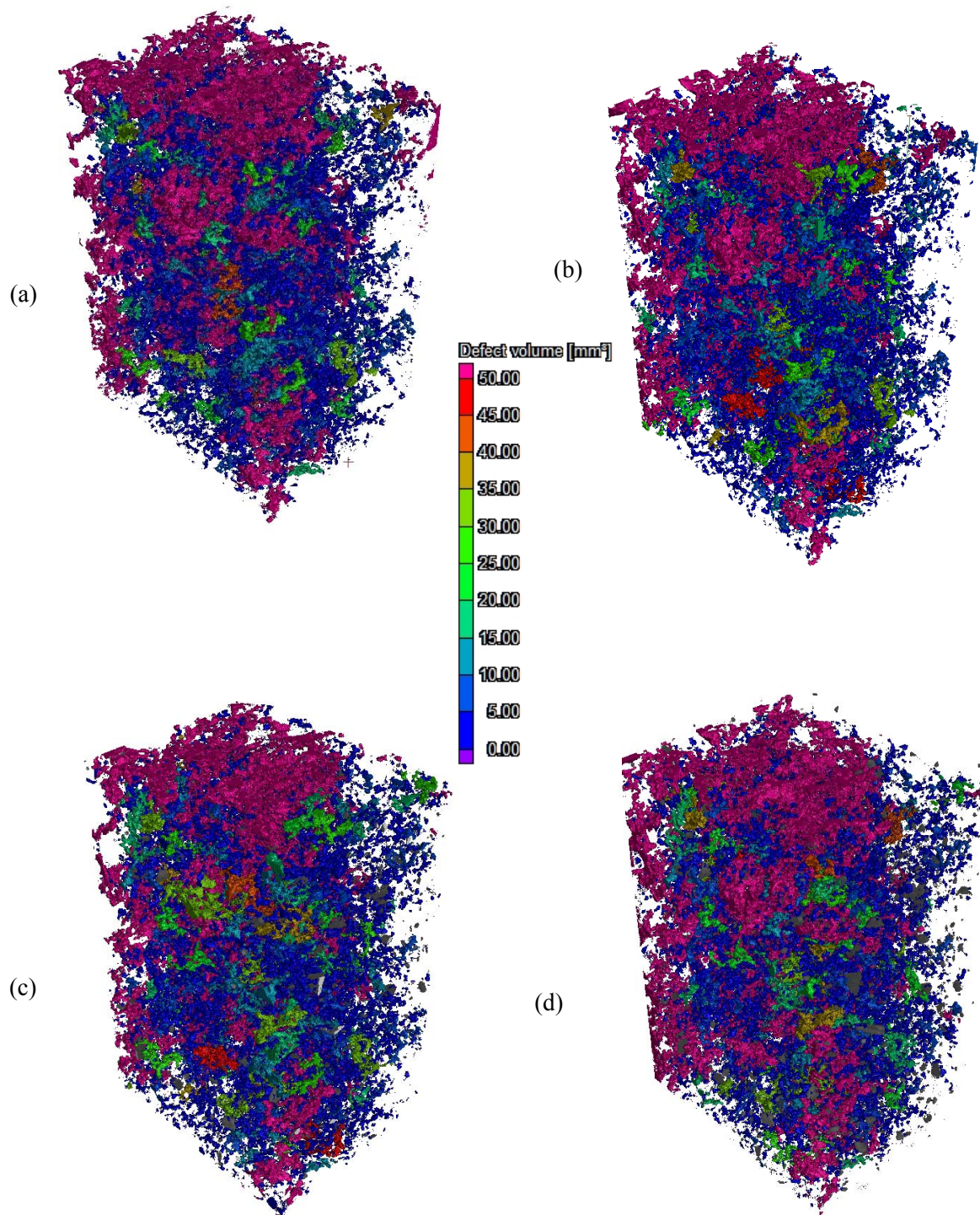


Figure 6-8 3D visualization of air void distributions for the same specimen: (a) Scan 1; (b) Scan 2; (c) Scan 3; (d) Scan 4

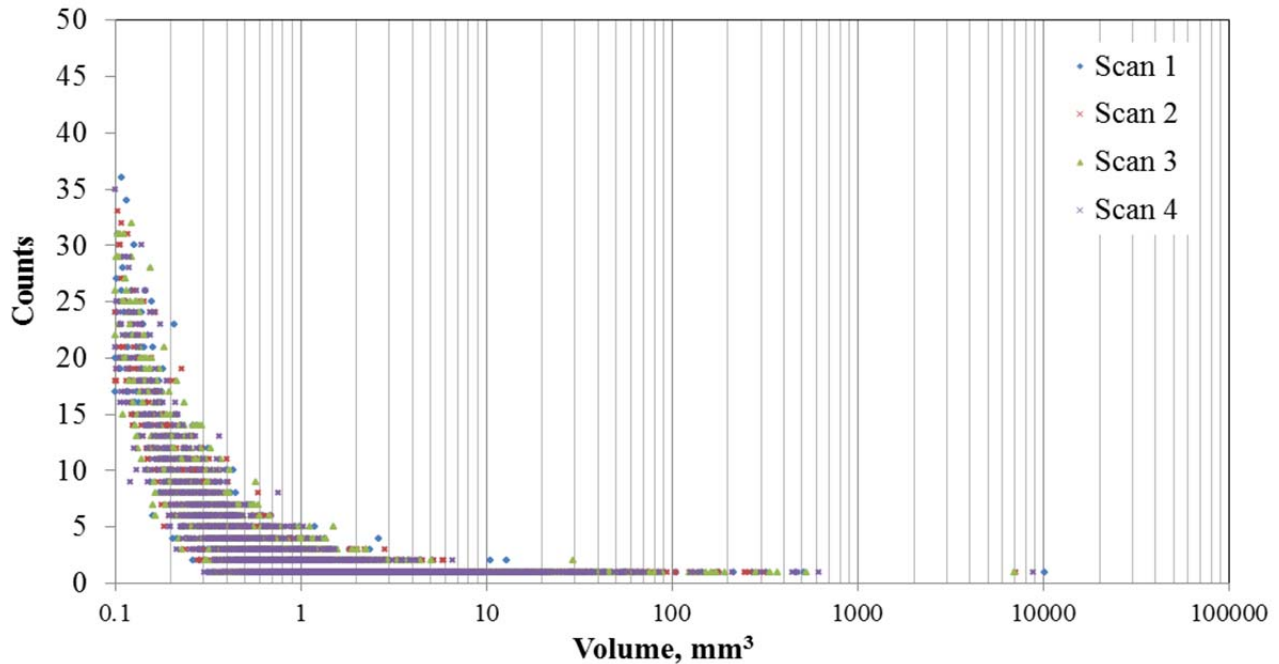


Figure 6-9 Changes in the 3D void distributions for the four scans

6.5 Case Studies

Four asphalt beams prepared from four dense-graded HMA mixes were investigated. The aggregate type was 12.5 mm nominal maximum aggregate size (NMAS). Two asphalt binders of the same performance grade (PG 64-28) were used: unmodified and modified by incorporating styrene-butadiene-styrene (SBS). Two levels of binder content were used: optimum and optimum plus 0.5%. The asphalt beams were compacted using an Asphalt Vibratory Compactor (AVC). The air void target for the prepared samples was 7 % \pm 1 %. Details about the test beams are provided in Table 6-3.

The four-point bending test was carried out on four asphalt beams created from four different mixes. Each beam was scanned using X-ray CT before and after the test and was processed using the developed framework. The fatigue results and the applicability of X-ray CT for quantifying the fatigue damage in the beam are discussed in this section.

Table 6-3 Test Beam Details

Beam code	Mix Type	Air Voids before testing
Beam 1	SP12.5 PG 64-28 (opt.)	7.70
Beam 2	SP12.5 PG 64-28 (opt.+0.5)	7.52
Beam 3	SP12.5 PG 64-28D (opt.)	6.20
Beam 4	SP12.5 PG 64-28D (opt.+0.5)	7.08

6.5.1 Fatigue test results

For an asphalt beam, the stiffness degradation curve plotted against the number of cycles (S-N curve) is typically divided into three main stages, as indicated in Figure 6-10. The rate of reduction in stiffness is quicker during the first stage than in the second stage, during which the reduction occurs linearly. In the third stage, microcracks accumulate and propagate to macro sizes, at which point failure occurs. When the common failure criterion is reached (50 % reduction in stiffness) the test is terminated without observable damage or cracks (Zhang et al. 2013). In this study, the fatigue analysis was therefore conducted for the third stage, during which damage can be easily detected and quantified.

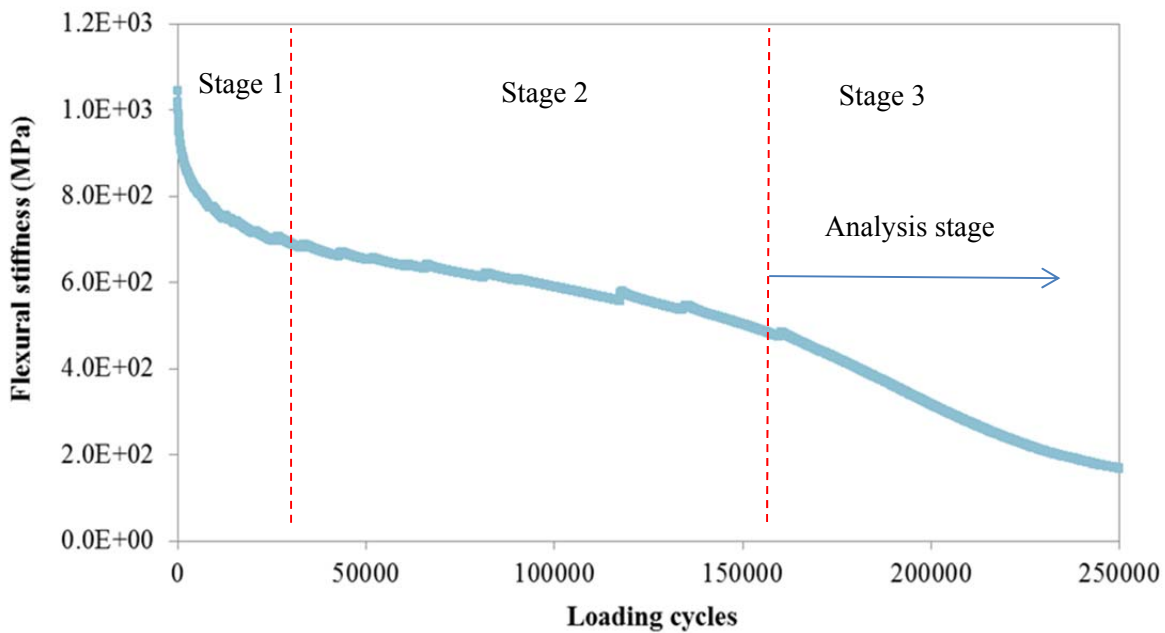


Figure 6-10 Typical reduction in flexural stiffness in asphalt mixtures

Figure 6-11 shows the S-N curves for four asphalt beams made of different materials. The curves reveal that the rate of fatigue damage for Beam 1 is much higher than for the other three specimens. Beam 4 shows a smaller reduction in stiffness and fails to exhibit the third stage of reduction; it therefore does not fail before the termination of the test. One explanation for this phenomenon is that beams comprised of softer mixes exhibit longer lifespans. Even though Beams 2 and 3 have different reduction rates, the overlapping stiffness at several points on the reduction curves influences the amount of accumulated damage. The significant difference in the damage rates of the specimens sheds additional light on the importance of finding a unique fatigue failure criterion for ending this test and for comparing the performance of different mixes. The number of cycles required to reach 50 % is an inappropriate failure criterion. In this regard, significant effort has been made to find an appropriate fatigue failure criterion, but the evaluation and prediction of HMA fatigue remain problematic.

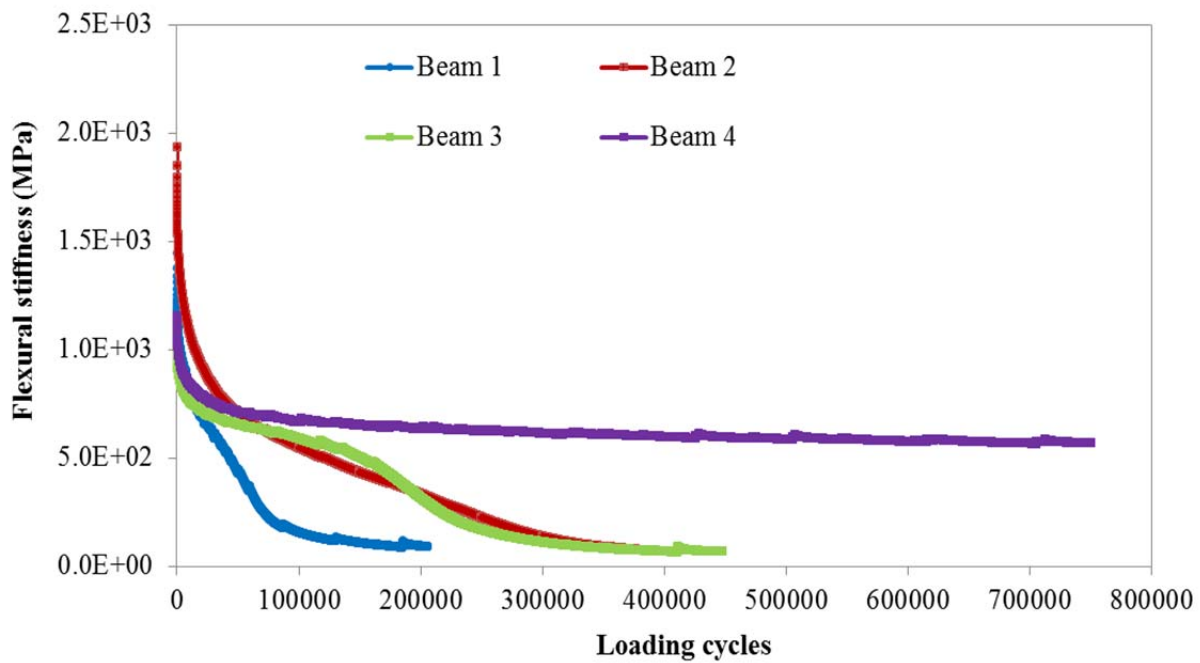


Figure 6-11 S-N curves for four asphalt beams

6.5.2 Air void distribution

Prior to the test, the air void distribution was calculated along the length of each asphalt beam. The results for the four beams are presented in Figure 6-12. The void distributions are non-uniform and take the form of wavy shapes that vary randomly from 4 % to 15 %. No specific trend is noted in the distributions of different beams. Beam 3 exhibits the greatest variation in air voids, with higher values toward the beginning of the beam than in the middle, which is more compacted. The distributions of Beams 1, 2, and 4 show continual overlaps. These findings are consistent with the experimental air voids listed in Table 3. However, the sudden changes from high to low or low to high values in the air voids at some locations along the beam length were a surprising observation and constitute a void characterization that is not visible in any experimental work. The irregular shape of the void distribution can be expected to affect crack patterns in HMA mixes. The very wide range in the variations would have a significant impact on performance.

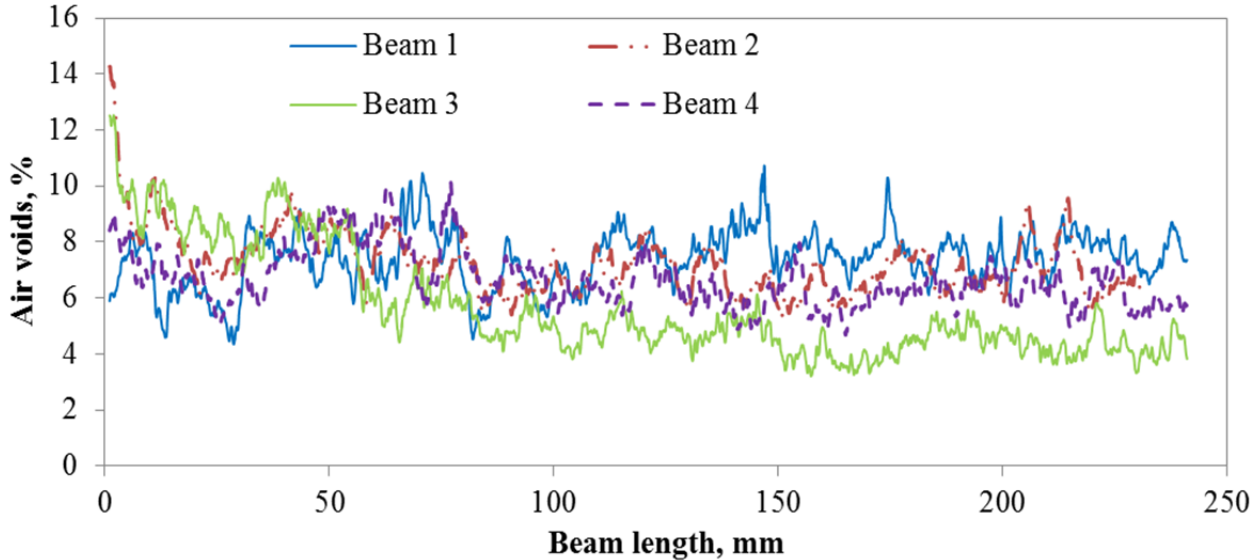


Figure 6-12 Air void distribution in 240 mm length of each asphalt beam

6.5.3 Damage characterization

Damage is the action of disintegration of the homogeneity of a material. HMA damage occurs when the cracks propagate or air voids expand. Detecting microcracks requires very high resolution. However, an indication of damage can be obtained from changes in colour intensity during the test or after crack propagation. Changes in the microstructure that occur during the test alter the colour intensity, enabling easy quantification of the damage. Such changes would be expected to occur throughout the mastic and air voids, which constitute possible locations where damage could occur.

To demonstrate damage in the asphalt beams, two methods were employed: 2D image slice analysis and 3D particle characterization. In 2D image slice analysis, the voids were calculated for each slice after testing and compared to the air voids prior to the test. It should be noted that voids after the testing represent the air voids before the test plus the damage. Figure 6-13 shows the changes in the void distribution for all beams after testing. The voids distributions before and after the testing are similar in shape. However, the changes in the air voids subsequent to the testing vary both among the beams and within the beam length in the same beam. Region 1 represents an example of the greatest change in air void distribution after the tests. On the other hand, in some spots, e.g., region 2, few changes could be noted in the air voids exhibited before and after testing. This observation might be related to the test configuration and the heterogeneity of the material. Image-based analysis is thus an advanced tool for identifying both the quantity and location of damage in HMA beams. With respect to the comparison of the beams, Beam 1 showed the greatest change in the voids due to testing damage, and Beam 3 exhibited the least amount.

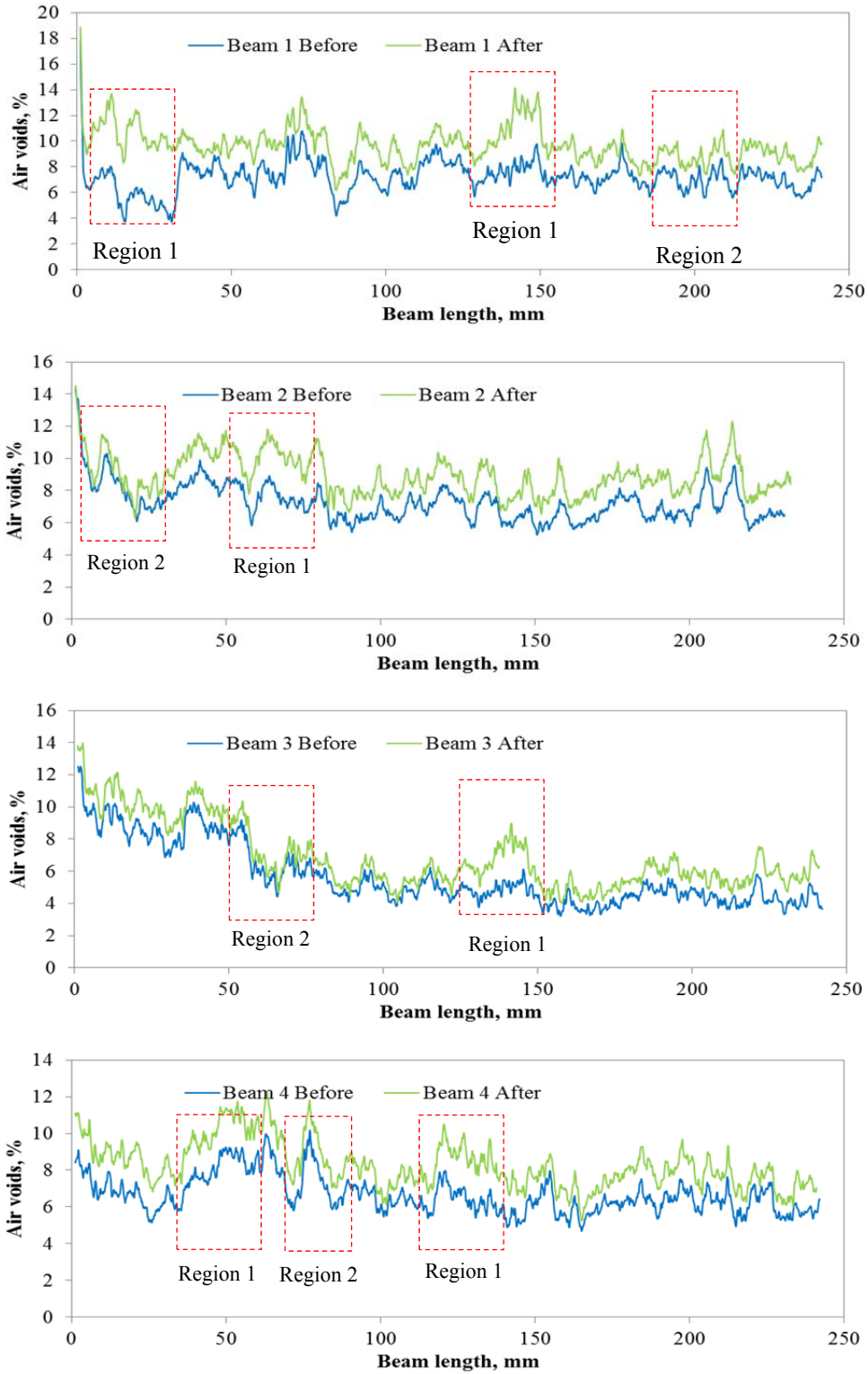


Figure 6-13 Air void distributions before and after the fatigue test

For quantification purposes, the degree of damage was estimated based on a damage factor called ξ , calculated as given in Equation (15) (Elseifi et al. 2011):

$$\xi = 1 - \frac{\bar{A}}{A_0} \quad (15)$$

Where

A_0 = the initial area of the undamaged section (before the test), and

\bar{A} = the effective cross-sectional area in the current damaged state (after the test).

The value of the damage factor varies from 1 (completely damaged state) to 0 (completely undamaged state).

The damage factor was quantified for cross sections along the length of the beam; the average value for each beam is shown in Figure 6-14. The damage induced in Beam 1 is about 2.25 times greater than that in Beam 3 and about 1.5 times greater than that in Beams 2 and 4. Although the average damage induced in Beams 2 and 4 was same value, the distribution differed significantly, as revealed in Figure 6-13. The relationships among the levels of damage, the mechanical performance, and the number of load cycles in the fatigue test will be considered for future work by the authors.

With respect to the 3D damage characterization, the distributions of void volumes were compared prior to and subsequent to the testing. Figure 6-15 shows the distribution of air void volumes for both cases. In general, the frequencies of occurrence of the void particles decrease when the void volumes increase. The void volumes after the test represent the quantification of the voids before the test plus the amount of the damage that has occurred during the test. For all beams tested, the number of small voids decreases significantly after the test. Larger volumes were quantified after the test than before the test. This observation could be the result of the creation of large volumes from air void expansion or crack propagation, which reduces the number of small volumes. In this case, the maximum volume of air voids subsequent to the test increased significantly. However, it is difficult to monitor changes in specific air void particles due to the complexity associated with their geometry, but damage can be calculated locally and the location of the maximum damage can be identified. Changes in the microstructure resulting from fatigue damage were therefore considered to be successfully depicted by X-ray CT. This

finding can also be confirmed from a comparison of Figure 6-9 and Figure 6-15 because no noticeable changes can be detected with respect to the non-tested specimen in the former figure.

The tested beams exhibited significantly different degrees of damage. Beam 1 was subject to the greatest damage, as indicated by the volume of the largest void particle shown in Figure 6-15 (a) compared to the same volume that appears in Figures 6-15 (b), (c), and (d). This result is consistent with the performance revealed in Figure 6-11. The beam with the shortest fatigue life was subject to the maximum fatigue damage, as computed from the X-ray CT images. It can be concluded that the integration of the developed framework with the X-ray CT method is a valid means of determining damage in large asphalt beams.

6.5.4 Crack Detection

Detecting cracks in an HMA fatigue beam is challenging: they are especially difficult to observe at the micro-level, although they might be evident when they reach the macro-level. Figure 6-16 shows a 3D visualization of an asphalt crack. It can be seen that the crack propagates in the mastic between the aggregate particles and that it is perpendicular to the direction of the loading of the test beam. The crack might become more visible at a higher scanning resolution although increasing the resolution might also hinder the analysis due to greater computational challenges.

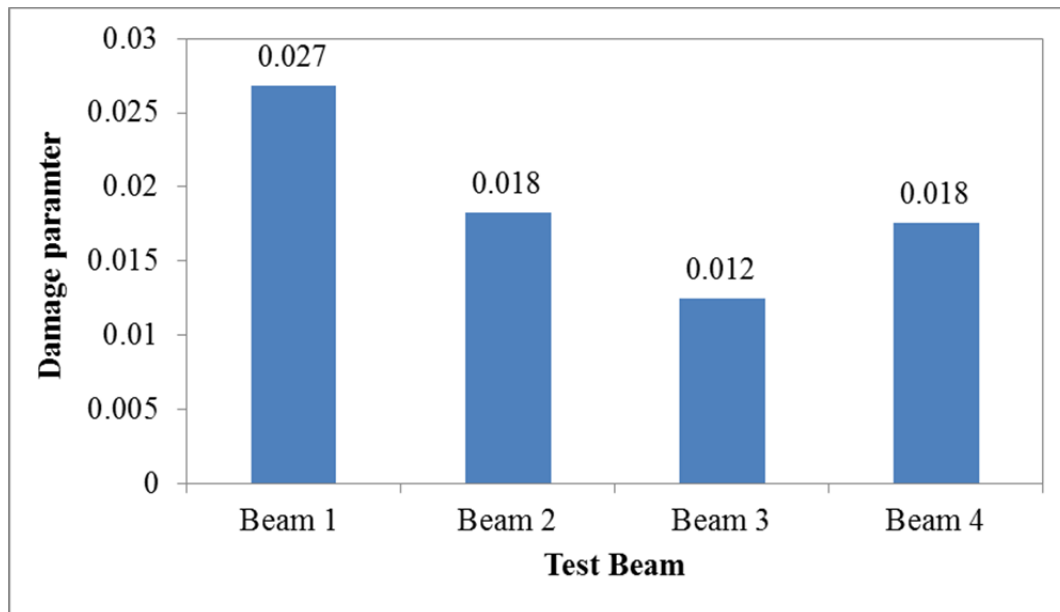


Figure 6-14 Average level of damage in the beams tested

To provide additional insight into X-ray 3D damage analysis, changes in the width of the crack were explored. As shown in Figure 6-17, the depth of the crack is about 7 mm from the bottom surface of the beam. Detecting the geometry (i.e., length and depth) and location of a crack would normally require special algorithmic processes. However, as discussed earlier, the pixels representing the crack in the image shown in Figure 6-17 have been quantified for inclusion in the damage analysis. The use of X-ray CT for HMA damage quantification therefore represents a unique and advanced methodology that provides direct damage estimation without the need for complex models and conversion methods, which offer only poor correlation between predicted and actual HMA performance.

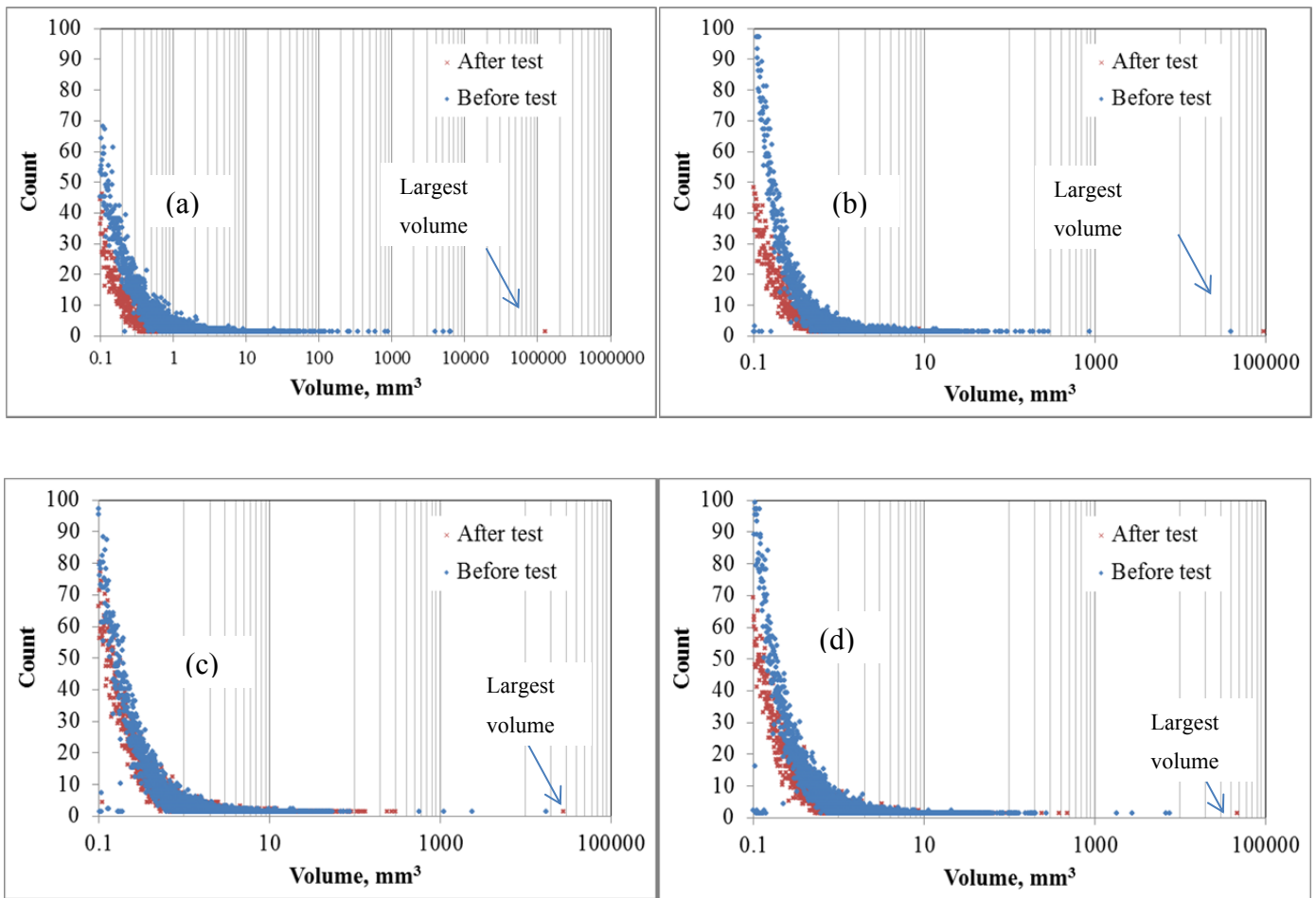


Figure 6-15 Effect of the fatigue test on void size distribution: (a) Beam 1; (b) Beam 2; (c) Beam 3; (d) Beam 4

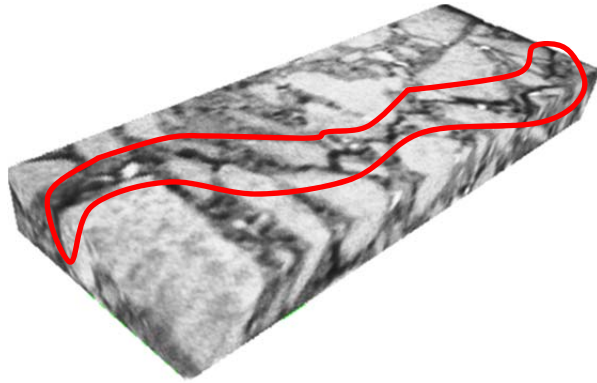


Figure 6-16 3D visualization of a HMA crack

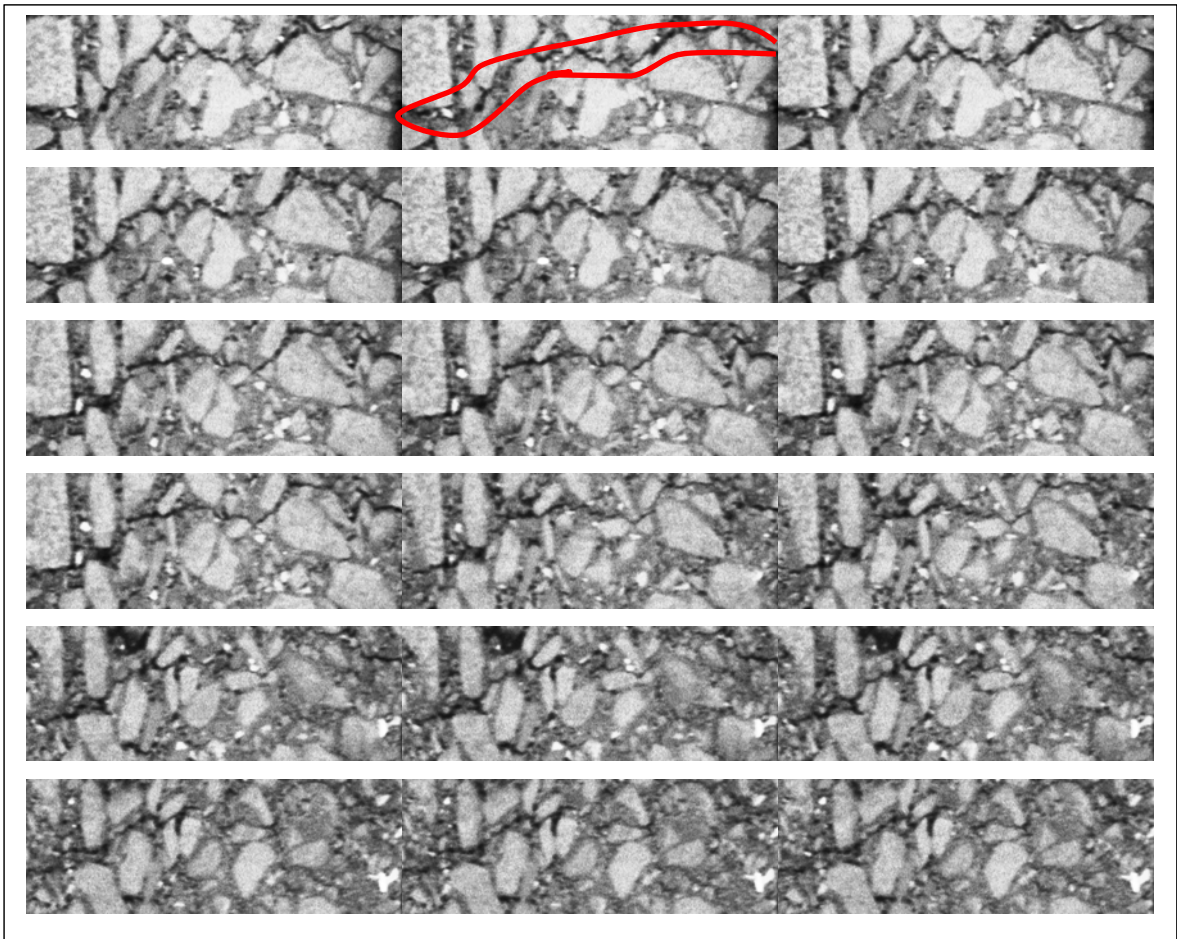


Figure 6-17 2D slices of crack region in asphalt beam

6.6 Summary and Conclusion

This chapter has described the investigation of HMA characteristics and performance using the image-based analysis explained in Chapter 5. The key parameters measured are aggregate texture and contacts, HMA air void distribution, and damage. Case studies that involved the use of X-ray CT imaging for analyzing air voids and damage in test beams subjected to four-point bending have been presented. Both 2D and 3D image analysis proved suitable for evaluating internal HMA structural characteristics, and in general, the results showed this type of analysis to be a promising tool for providing an understanding of the packing characteristics and fatigue damage of HMA.

The SEM images indicated a high degree of variability in the aggregate texture as revealed by the 3D surface view. Based on observations of the amplitudes of the colour intensities, the 12.5FC was rougher in texture and exhibited more irregular amplitudes than the 12.5. With respect to the 2D internal structure, the indices demonstrated the effect of aggregate type and binder content. Binder type had no statistical impact on the indices measured in this study. When X-ray CT was employed, the air voids and damage distribution in the asphalt beams was shown to be non-uniform, with possible significant changes along the length of the beam. For this reason, the incorporation of air void distribution into any beam evaluation is recommended. In the case study presented, the damage to the asphalt beam caused by the fatigue test was observed to be greater for low levels of fatigue life. When an asphalt crack reached macro size, it became visible in the X-ray CT images. However, micro-crack detection requires such high resolution that computational issues might affect the analysis. Instead, an alternative valid and acceptable approach could be indirect damage analysis through the quantification of changes in the air voids.

Chapter 7

Microstructural Finite Element Modelling of HMA

This chapter presents the development of image-based and specimen-specific three-dimensional (3D) finite element (FE) microstructural modelling of hot mix asphalt (HMA) mixtures using X-ray CT images. X-ray CT was employed for constructing a microstructural model that enables the visualization and measurement of changes in the HMA response to microstructural changes. This model was developed for the specific investigation of the effect of air voids and the aggregate modulus on the predicted response of a mixture.

7.1 Components of the HMA Microstructure

Figure 7-1 shows 2D slice and 3D views of the HMA microstructure obtained from X-ray CT images. Three microstructure components of the HMA are visible: aggregate, mastic, and air voids. The mastic is composed of binder and mineral fillers. When the microstructure incorporates fine aggregate particles and air voids into the mastic, this composition scale is called a fine aggregate asphalt matrix (FAM). These internal components can be clearly distinguished based on a visual examination of X-ray CT images. The spatial distributions of these microstructural components are non-uniform. In some regions, the aggregate skeleton can be seen to be in better contact than in other areas of the beam. Variations in beam microstructure can lead to significant changes in the strain and stress distribution, and FAM distribution and aggregate contact are major factors that could control cracking pathways. Therefore, developing a microstructural model is important for accurate prediction of the response. Such a modelling approach may lead to a better understanding of role of the internal structure on the performance of HMA.

7.2 Extraction of the Aggregate from the Images

For the research presented in this thesis, the asphalt images were processed using 3D image processing software called XCAT in order to extract the aggregate particles from the images. For the application of the 3D image analysis algorithms, the software requires the input of a stack of

images. A stack of 2040 images for a 200 mm length of asphalt beam was therefore carefully processed in order to obtain representations of aggregate that exhibited realistic shapes and characteristics. To achieve this goal, a set of steps were performed in order to remove the noise in the aggregate images and to enable the particle boundaries to be detected. This procedure included filtration, watershed segmentation, and thresholding. Figure 7-2 shows the steps involved in processing a 3D image of asphalt mixture. Additional details about the procedure and software development are available in (Kutay et al. 2010).

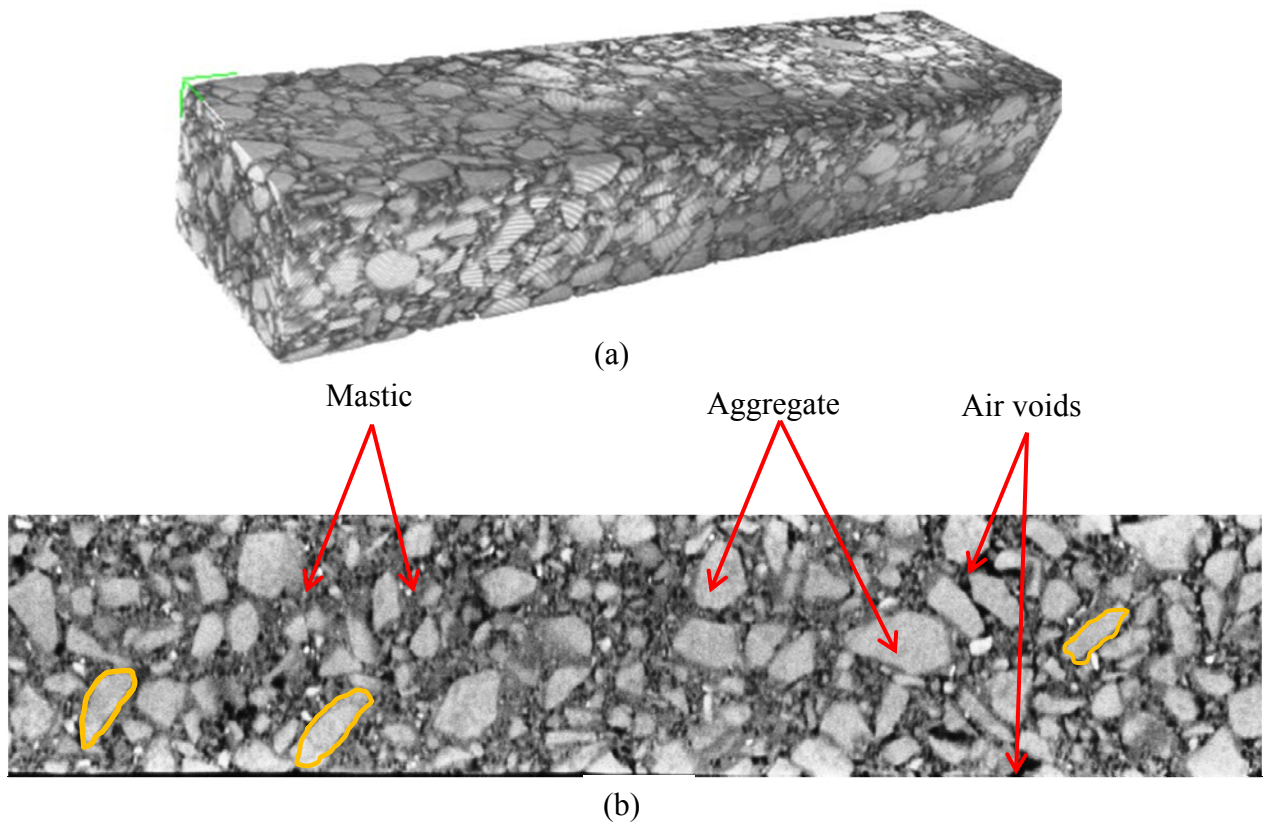


Figure 7-1 Images of an HMA mixture obtained using X-ray CT: (a) 3D; (b) 2D slice

The 3D images that enable the visualization of the extracted aggregate particles are shown in Figure 7-3. Figure 7-3 (a) indicates the complexity of the shape of the aggregate particles, particularly in a virtual representation. The virtual mixture has two main components, as

indicated in Figure 7-3 (b): the aggregate and the FAM, which contains aggregate particles smaller than 2.36 mm. The total air void content was assumed to be part of the FAM shown in this image. To clearly distinguish the digital representation of the aggregate, Figure 7-4 provides representations of four categories of aggregate size, ranging from 2.36 mm to 12.5 mm. It can be observed that the smaller the particle size, the greater its frequency in the mixture. The total number of particles was found to be 4437, with only 15 particles that were 12.5 mm or larger. The overall particle distribution matches that expected in the physical mixture with respect to the frequency of each particle size.

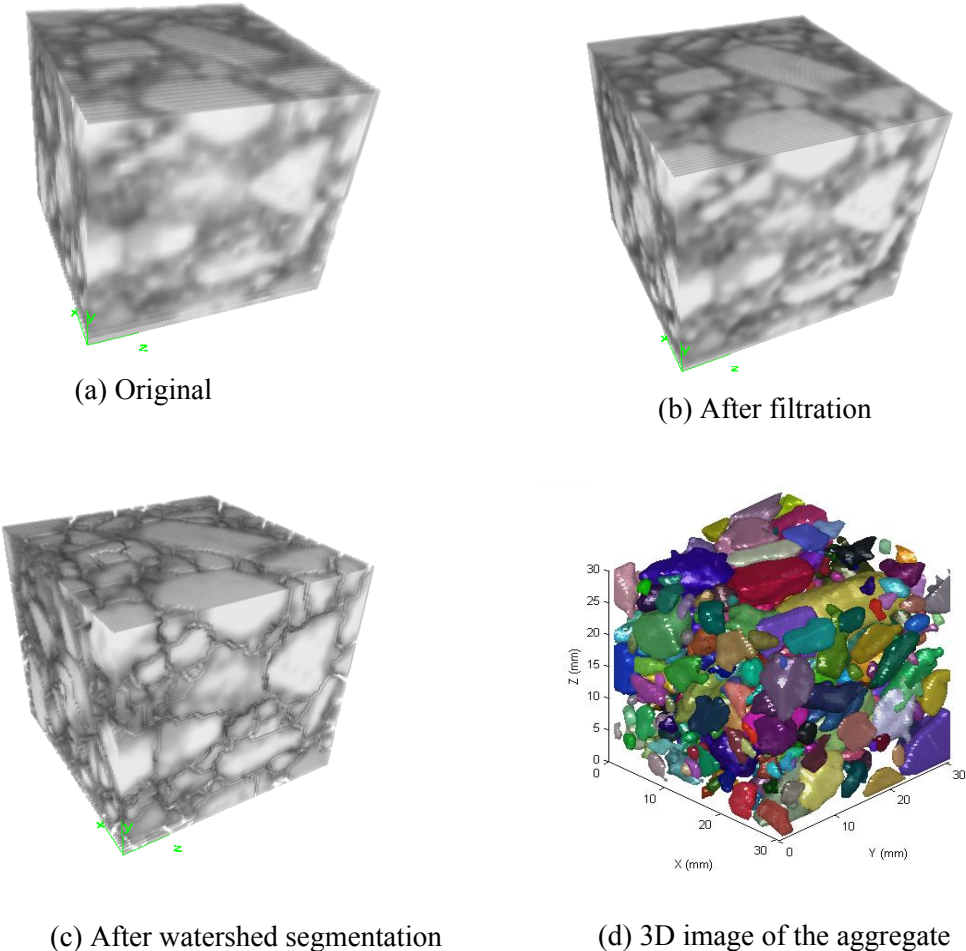


Figure 7-2 Illustration of the steps for extracting aggregate images

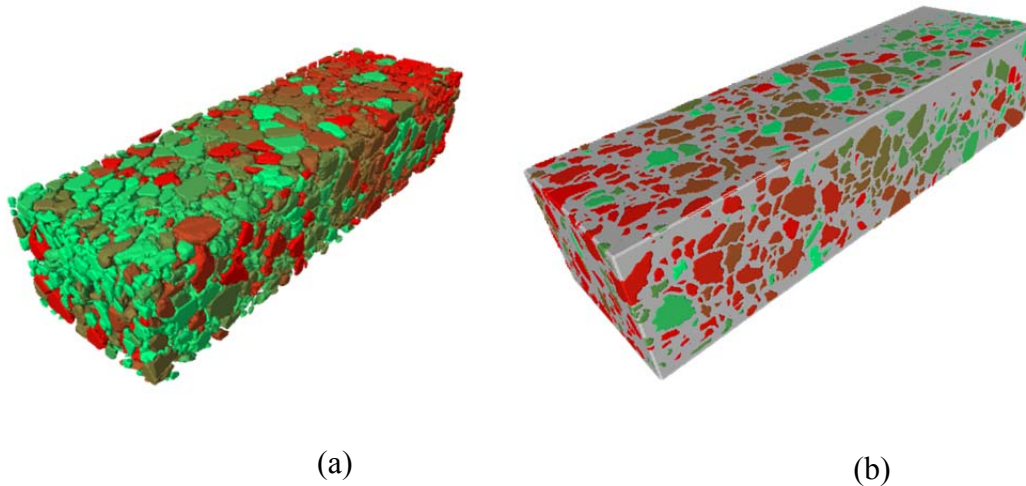


Figure 7-3 3D digital images: (a) aggregate; (b) mixture

7.3 Building a Three-Dimensional Microstructural Model

A model of a 30 mm cube of asphalt mixture was developed to investigate the influence of the microstructure on HMA performance. The 3D microstructural model was constructed in the following phases.

7.3.1 Phase 1: Identification of Microstructural Components

Figure 7-5 shows the three main microstructural components that were quantified based on the X-ray CT images: aggregate, air voids, and the FAM. Figure 7-5 (b) is an image of the extracted aggregate discussed above. The aggregate percentage was found to be 42.66 %. For the FAM, which is shown in Figure 7-5 (c), a percentage of 57.34 % was obtained by extracting the aggregate component from the volume of the solid cube. The distribution of the air voids, whose image is shown in Figure 7-5 (d), was determined from the original X-ray CT images through thresholding, as discussed in Chapter 5. They represented 7 % of the total volume of the mixture. The volume of the air voids was then subtracted from the FAM to produce a percentage for the FAM without air voids, as shown in Figure 5 (e): 50.34 %. To provide visual verification of the extracted components, the air void distribution was demonstrated around the aggregate structure, as can be seen in Figure 7-5 (f). The spatial distribution of air voids create space that reduce aggregate to aggregate contact which may cause instability and create heterogeneous stress distributions in the FAM domain that influence on HMA fatigue cracking resistance.

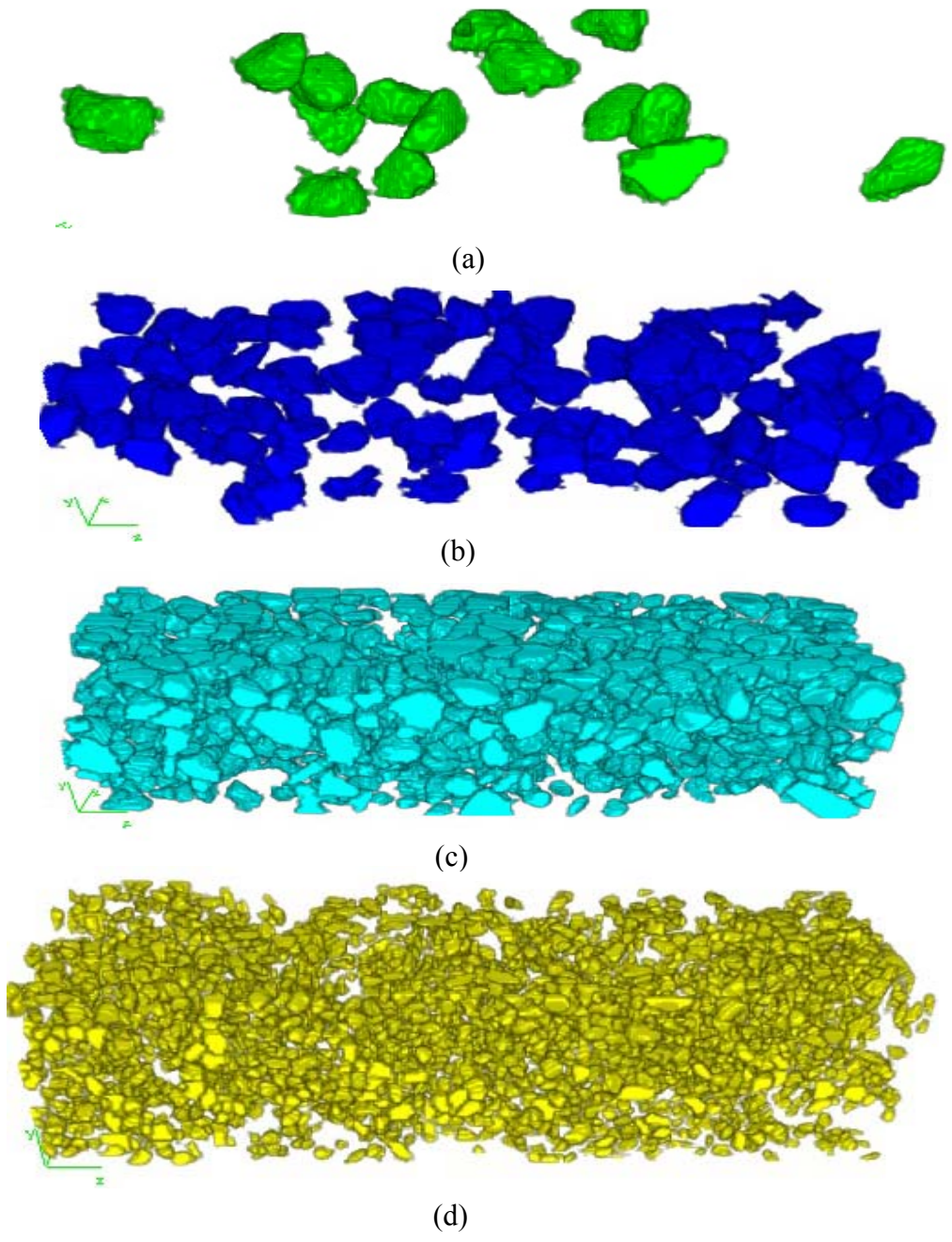


Figure 7-4 3D visuals of the aggregate sizes in the asphalt beam: (a) > 12.5 mm; (b) 12.5 mm to > 9.5 mm; (c) 9.5 mm to >4.75 mm; (d) 4.75 mm to > 2.36 mm

7.3.2 Phase 2: Finite Element Mesh and Boundary Conditions

The aggregate and the FAM were meshed separately for use in the FE modelling. The effect of the air voids was included when they are subtracted from the geometry of the FAM and modelled as empty domains. Linear tetrahedral elements type C3D4 was used for all cases. For example, the model shown in Figure 7-6 (a) contains 466,608 C3D4 elements: 196,222 for the aggregate and 270,386 for the FAM when the air voids were ignored, as shown in Figures 7-6 (b) and (c), respectively. Constraints, including a full elimination of the degree of freedom, are also defined for the contact between aggregate and FAM regions. A displacement load of 0.04 mm was applied on the top of the modelled specimen to measure the response within the viscoelastic region, and the model was constrained in the Y direction, as shown in Figure 7-6 (a). The scenarios studied for this research involved identical boundary conditions as well as loading values and directions, but in line with the goals of developing the model, the percentage of each component in the mixture differed.

7.3.3 Phase 3: Constitutive Model and Material Parameters

Aggregate and FAM properties were defined individually as separate constitutions in the ABAQUS commercial software. A generalized Maxwell model was applied for modelling the linear viscoelastic properties of the FAM in the form of a Prony series. The viscoelastic parameters used in the numerical implementation of this model are shown in Table 7-1. The Poisson's ratio (ν) of the FAM was assumed to be 0.49. The aggregate was modelled as an elastic material with a modulus of 25 GPa and a Poisson's ratio of 0.25.

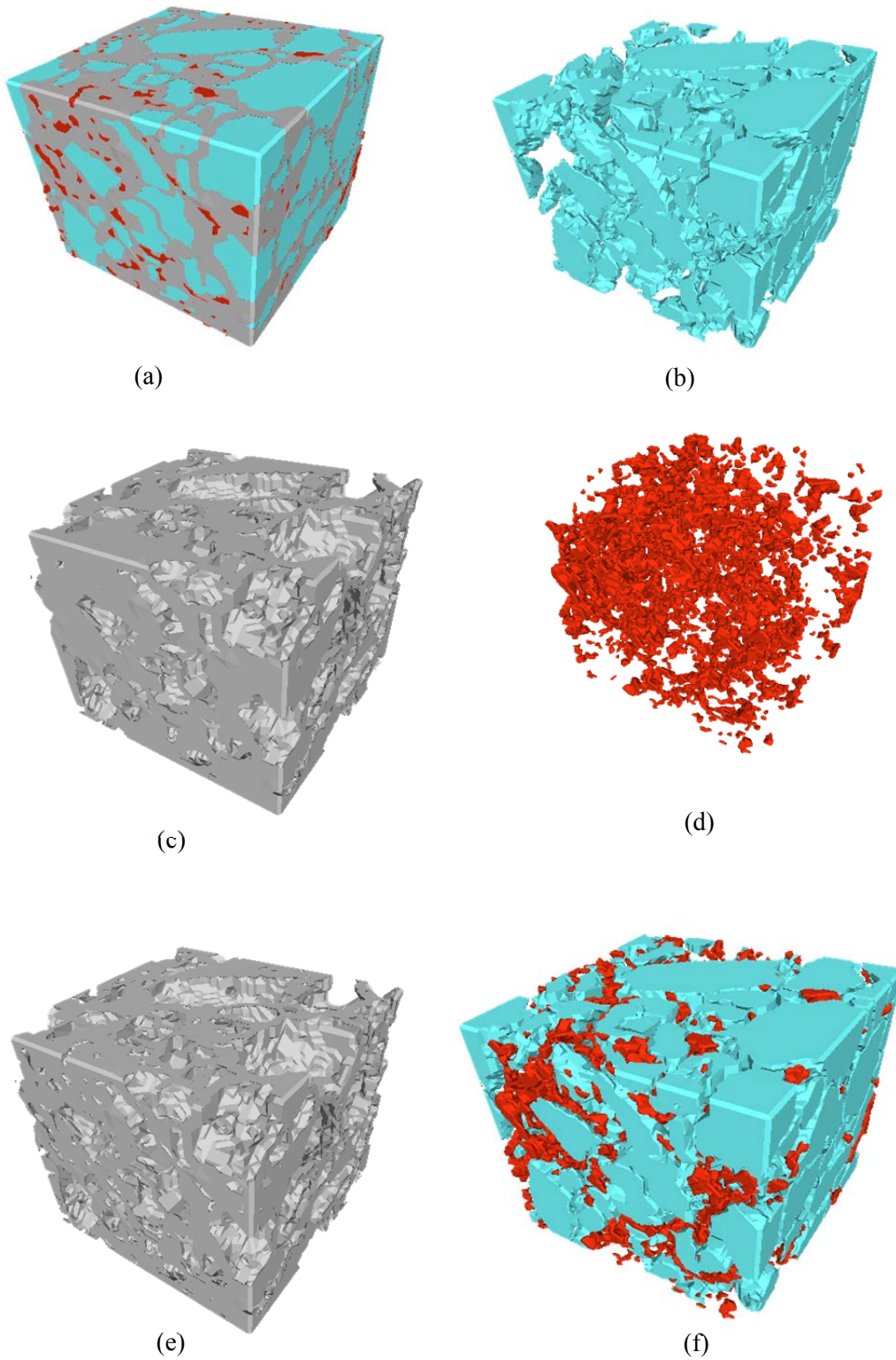


Figure 7-5 3D images of the asphalt mixture microstructure: (a) mixture; (b) aggregate; (c) FAM; (d) air voids; (e) FAM without air voids; (f) aggregate and air voids

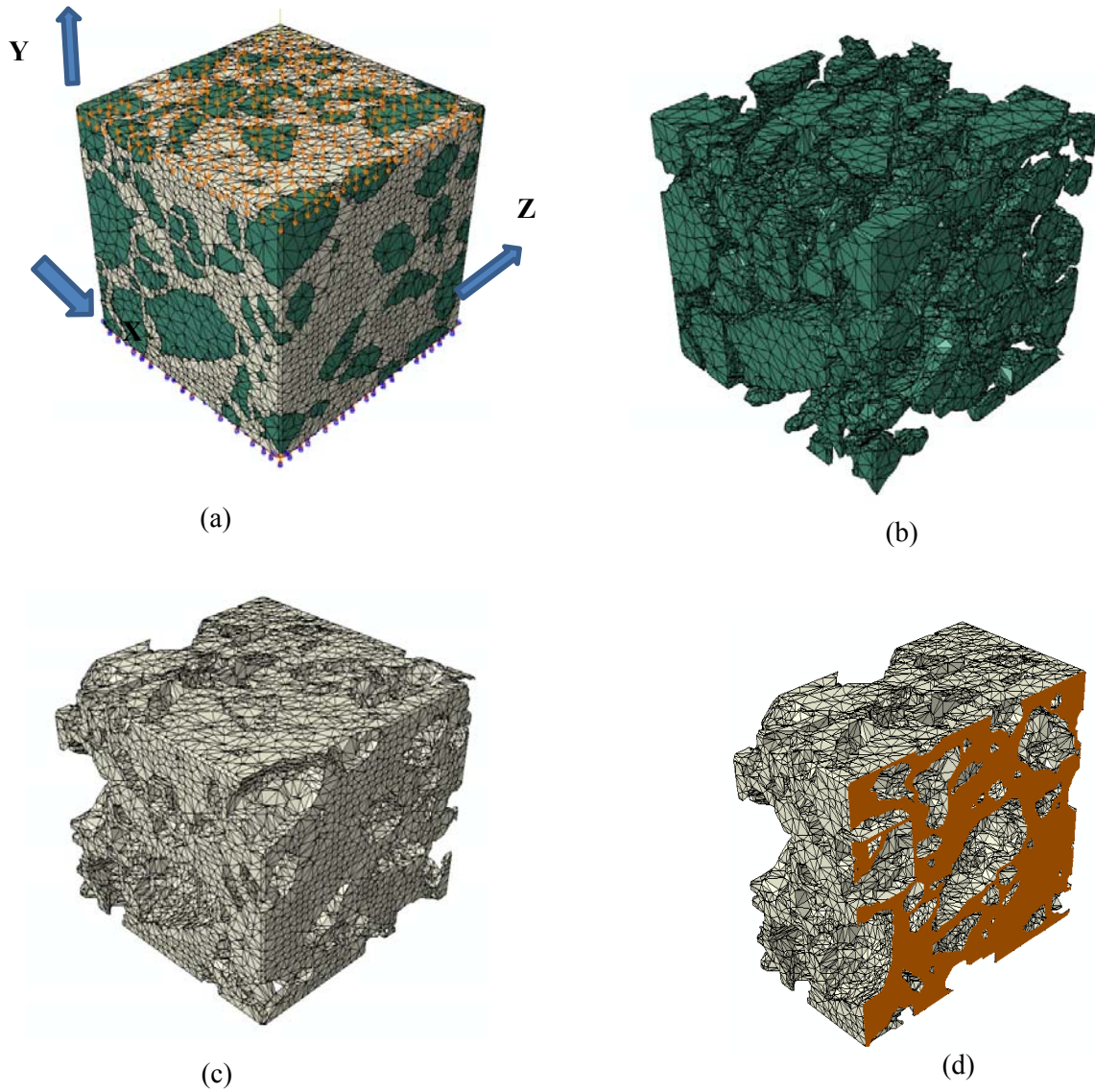


Figure 7-6 Images of the FE model mesh: (a) mixture; (b) aggregate; (c) FAM; (d) FAM cross section

Table 7-1 Prony Series for the Generalized Maxwell Model (Coleri et al. 2012)

i	g_i	λ_i
1	6.80E-01	6.49E-03
2	1.41E-01	6.89E-03
3	1.28E-01	7.70E-02
4	2.79E-02	1.10E+00
5	5.27E-03	2.00E+00

i: Maxwell model unit; g_i: spring constant for the ith spring; λ_i: relaxation time

7.4 Microstructural FE Model Results and Discussion

The performance of an asphalt mixture can be evaluated based on its response to loading, which is related to the composition of the microstructure. Although the mixture was modelled as linear viscoelastic without a damage mechanism, the microstructural model predicted the HMA response based on a relevant failure mechanism as indicated by the heterogeneous stress and strain distributions.

7.4.1 Stress and Strain Distributions

Figure 7-7 shows the vertical stress and strain contours for the model specimen with respect to both the aggregate and the FAM without air voids. This figure illustrates the discontinuity in the stress and strain contours that arise because of the high degree of stiffness that characterizes the aggregate. In general, consideration of the HMA as heterogeneous enables the real evolution of the damage to be described and captures a more accurate indication of the response than a macrostructure approach in which the material is assumed to be one homogeneous body.

A comparison of Figure 7-7 (a) and 7-7 (b) reveals that the stress values for the aggregate are higher than those for the FAM. As shown in Figure 7-7 (a), the stress on the aggregate particles varies according to the location and packing characteristics of the underlying particles, which control load transfer to the particles located on the bottom. Figure 7-7 (b) shows that the effect of the aggregate on stress distribution is significant because it controls the local

concentration of stress in the FAM, which would impact crack initiation and propagation in the FAM. Although Figure 7-7 (c) indicates that the distribution of the strain on the aggregate seems to be uniform, it in fact varies significantly with respect to the FAM, particularly around the interface with the aggregate. These observations shed additional light on the importance of the aggregate-FAM bond and its impact on crack initiation. The response distribution emphasizes the significance of microstructural modelling with respect to identifying both areas of potential damage throughout a mixture and the relationship to the design variables. This model can therefore be used for predicting weaknesses in HMA mixes, especially those due to poor aggregate orientation or gradation.

7.4.2 Effect of the Aggregate Elastic Modulus on the Response of the Mixture

A major advantageous feature of the developed model is its ability to perform sensitivity analysis based on utilization of the effect of changes in the characterization of the mix components. Figure 7-8 shows the effect of the elastic modulus of the aggregate with respect to the response based on the FAM loading and unloading diagrams. The study involved four levels of aggregate elastic modulus at 5 GPa increments but with a constant Poisson's ratio. The predicted response increases with each higher level of the aggregate elastic modulus, which indicates improved overall mixture stiffness. The percentage increase in stress clearly declines as the modulus increases. The high stiffness aggregate can produce a mixture with both a high degree of stiffness and a greater likelihood of cracking, as indicated by the induced stress. This figure also shows that the stress release is faster for an aggregate with a higher modulus, which changes the viscous nature of the FAM. Aggregate sources should thus be classified according to their modulus in order to avoid the inclusion of particles that are either stiff or soft in some associated physical parameters.

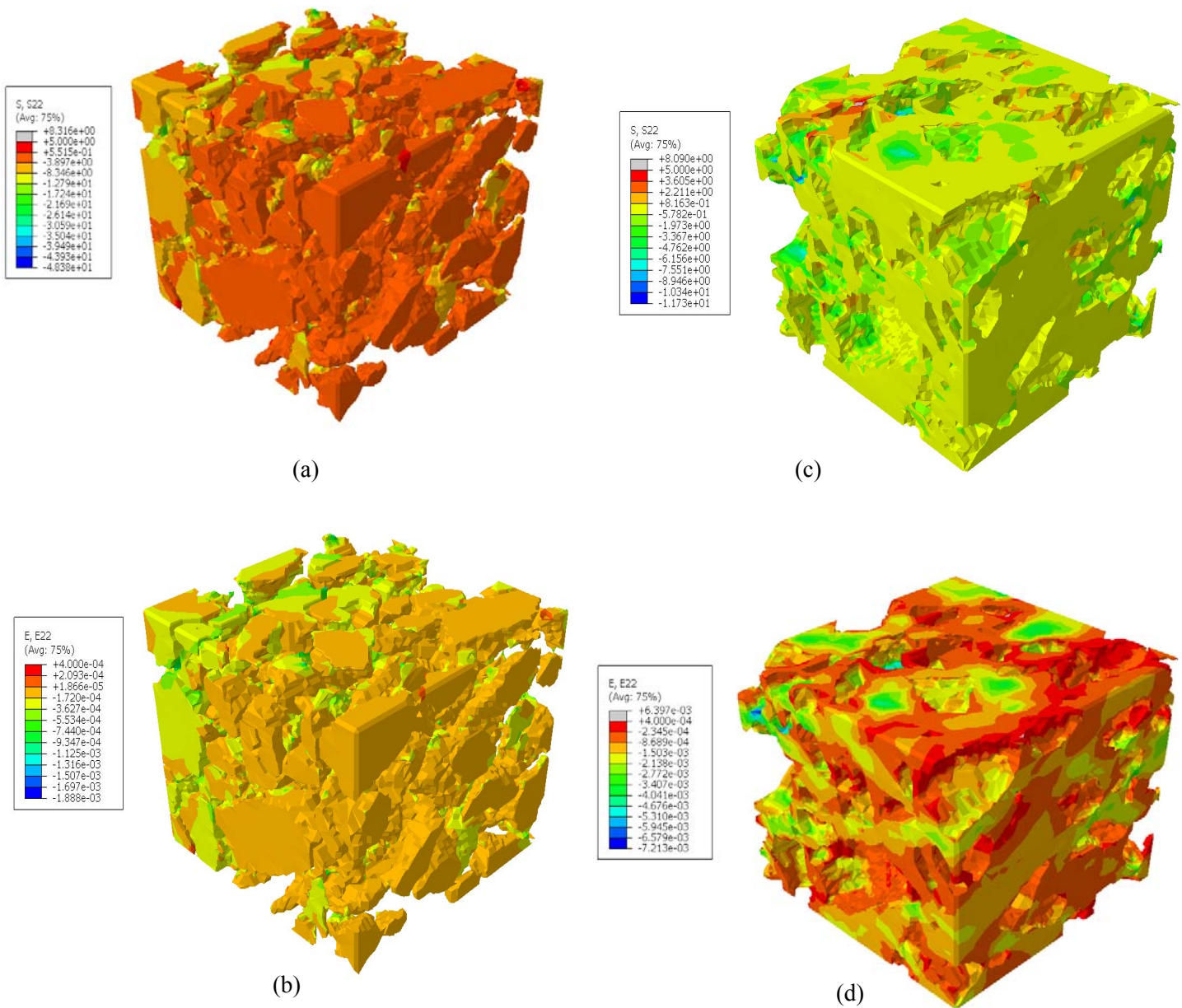


Figure 7-7 3D Microstructural response: (a) stress on the aggregate; (b) stress on the FAM; (c) strain on the aggregate; (d) strain on the FAM

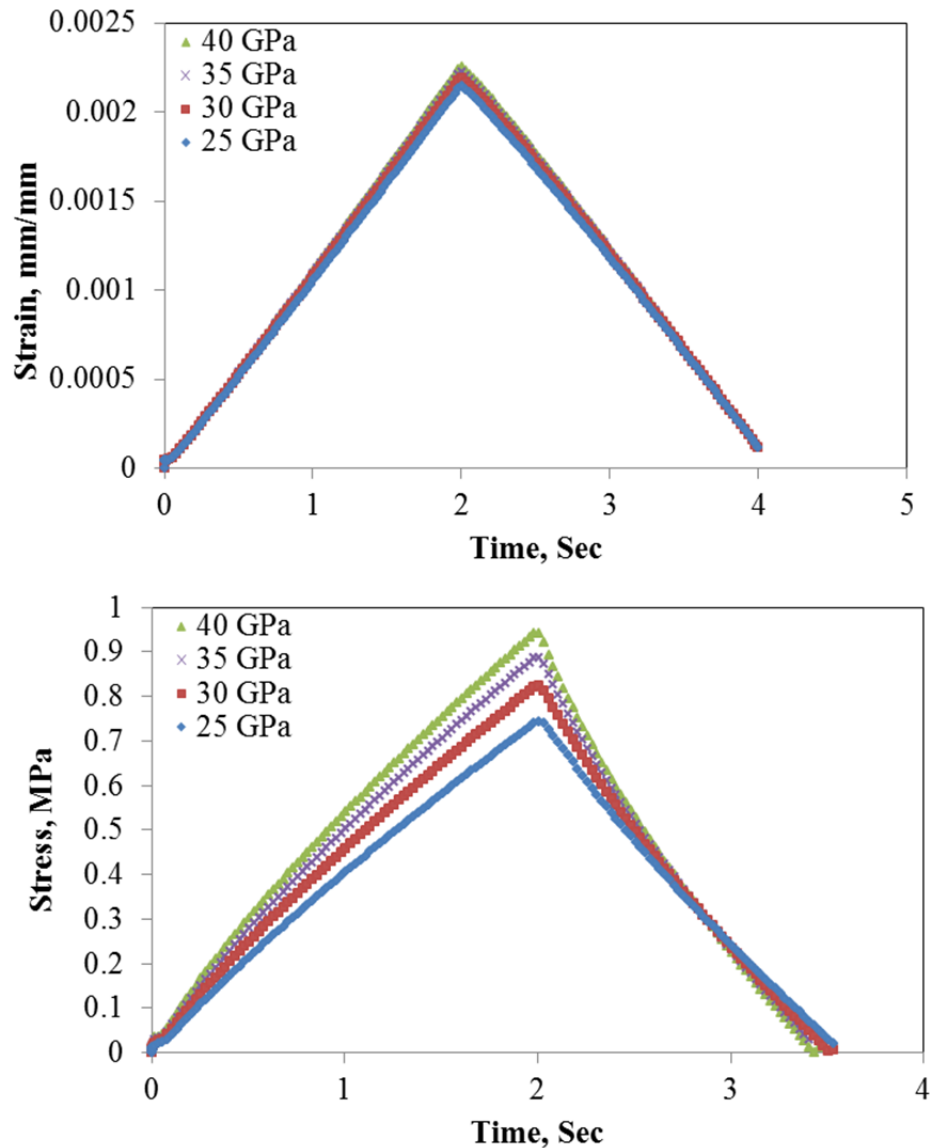


Figure 7-8 Effect of the aggregate elastic modulus on asphalt mixture response

This modelling approach enables the use of a thresholding approach with respect to the effect on aggregate modulus of other mixture design variables because the comparison can be based on identical arrangements of aggregate in the compacted mixture. Rerunning the analysis would enable the evaluation of many other parameters, such as FAM modulus, aggregate

skeleton, or air voids. The importance of this modelling approach lies in its determination of the optimal level of mix stiffness needed for resistance to rutting and fatigue cracking based on the predicted response.

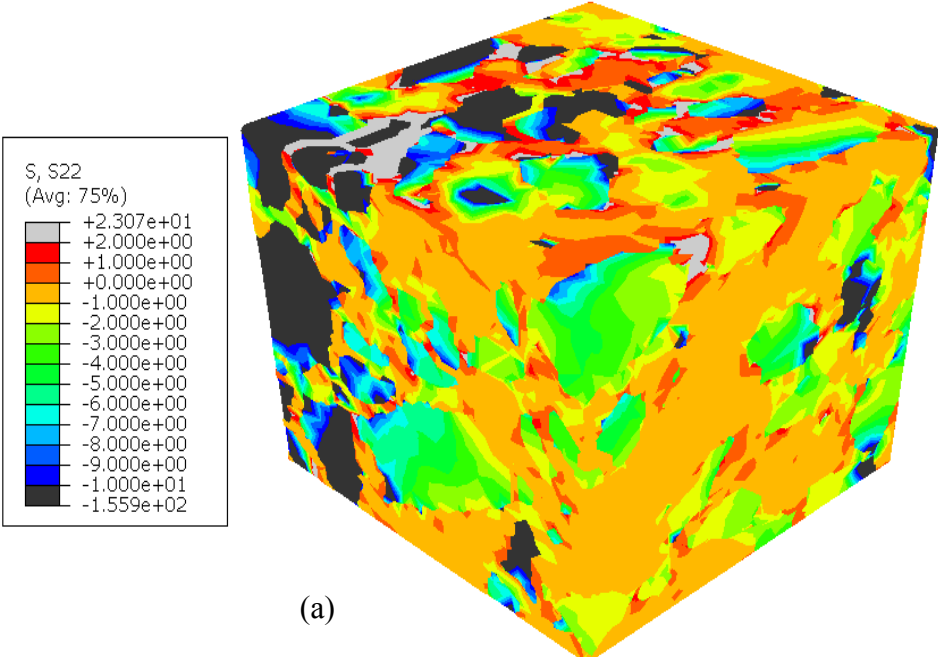
7.4.3 Effect of Air Voids on the Asphalt Mixture

Air voids have a significant effect on the response of asphalt mixtures because they create structural heterogeneity, which has a considerable impact on the response. To experimentally measure the effect of air voids on the asphalt mixtures, specimens are prepared with differing air void levels, and the mechanical performance is measured for each level. The relation between air voids and performance is always based on the macroscopic response. However, the internal structural changes with loading are a key factor in performance, particularly with respect to cracking. To investigate the effect of air voids on the response, two model specimens were prepared: with and without air voids. A load was applied that would reach a 0.04 mm displacement on the top of the specimen with a strain rate of 700 μ strains/s in compression mode.

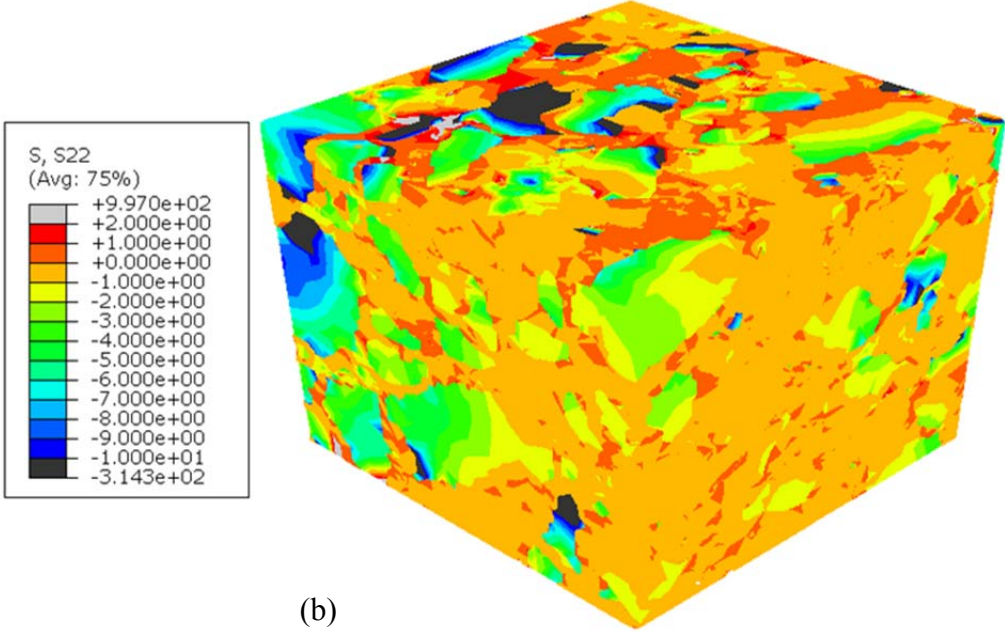
The vertical stress distributions at the maximum applied loads before unloading are shown in Figure 7-9, which indicates that air voids have a strong impact on stress distribution, which would impact the amount of induced damage. The stress levels with the presence of air voids are clearly higher than those that without air voids. Both distributions are non-uniform, but more variation is evident in the stress contours of the mixture with the air voids than in those of the mixture without air voids. It can also be observed that the air voids create a greater concentration of localized stress, which might increase the probability of damage. Caution should therefore be used with respect to choosing asphalt compaction method due to its influence on air void distribution that would affect HMA potential for damage.

Figure 7-10 illustrates the stress and strain responses of mixtures with and without air voids. The responses were measured at mid-height on the surface of the specimen. The maximum stress for the specimen with air voids is twice as high as that for the specimen without air voids. It can also be seen that the rate of development of stress and strain during the loading stage is significantly higher in the presence of air voids. As well, the stress and strain release is

faster for the specimen containing air voids, a finding attributable to the existence of the voids, which provide an empty domain that permits the material to return to its original shape.



(a)



(b)

Figure 7-9 Effect of air voids on the asphalt mixture response: (a) no air voids; (b) 7 % air voids

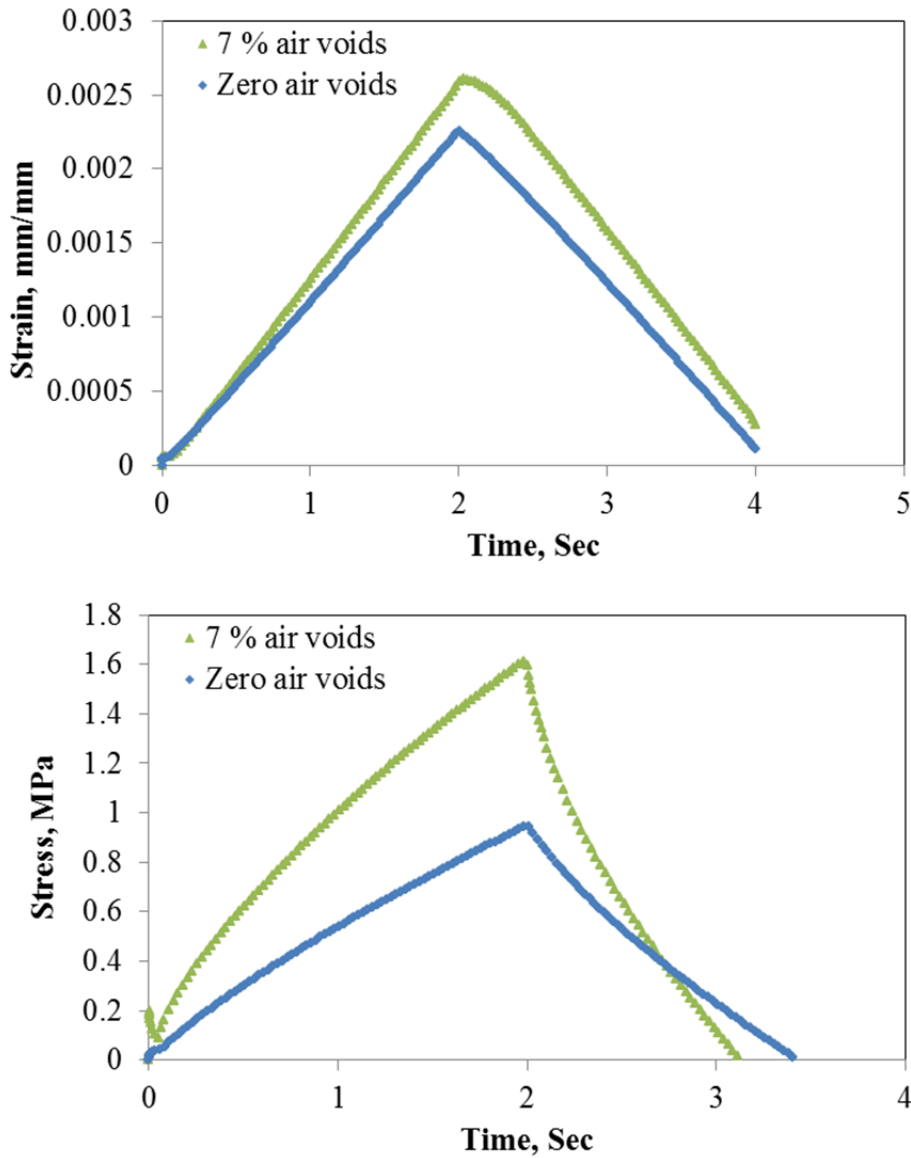


Figure 7-10 Effect of air voids on the asphalt mixtures responses: (a) strain in compression; (b) stress in compression

7.4.4 Effect of Air Voids on the FAM

Since the air voids were shown to have a significant impact on the predicted response of the mixture, it was reasonable to investigate the effect at the FAM scale because the FAM represents a possible domain where cracks initiate and propagate. To investigate the effect of air voids on the FAM responses, a model of a solid FAM cube with no air voids was created. Air voids were

then subtracted from this solid volume in order to obtain a model of a specimen that contains air voids. The boundary conditions and loading mode were similar to those for the model of the mixture specimen. Figure 7-11 shows the stress distributions in the loading direction for FAM both without and with air voids. Air void distribution clearly has an obvious effect on FAM stress distribution: the maximum stress for FAM with air voids was approximately twice that without voids. It was also observed that local stress concentrations always occur around the empty domains created by the air voids.

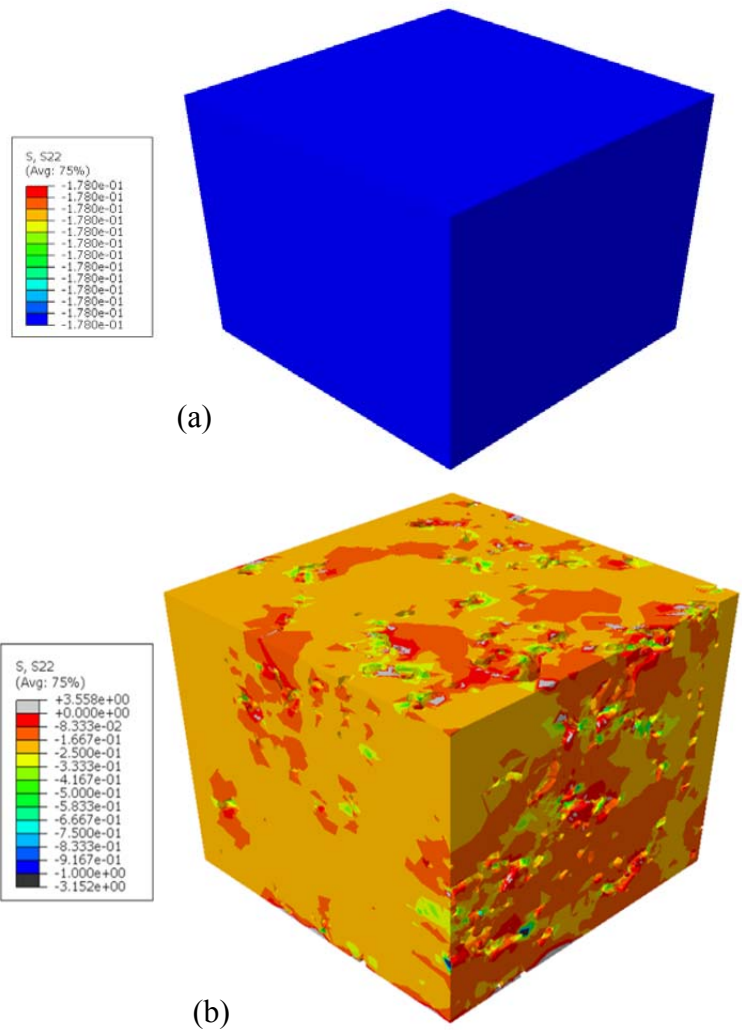


Figure 7-11 Effect of air voids on FAM responses: (a) no air voids; (b) air voids

Stress was measured at four different locations around the center of the surfaces of the vertical cross sections of the model specimens. As shown in Figure 7-12, for the FAM containing air voids, the stress values vary according to location, results that differ from the values indicated in Figure 7-12 (a), in which a uniform stress distribution can be measured at all locations. The maximum stress at location 2 exceeded twice the value measured at location 4. This observation indicates that the induced damage can be expected to vary significantly throughout the FAM based on local stress concentrations.

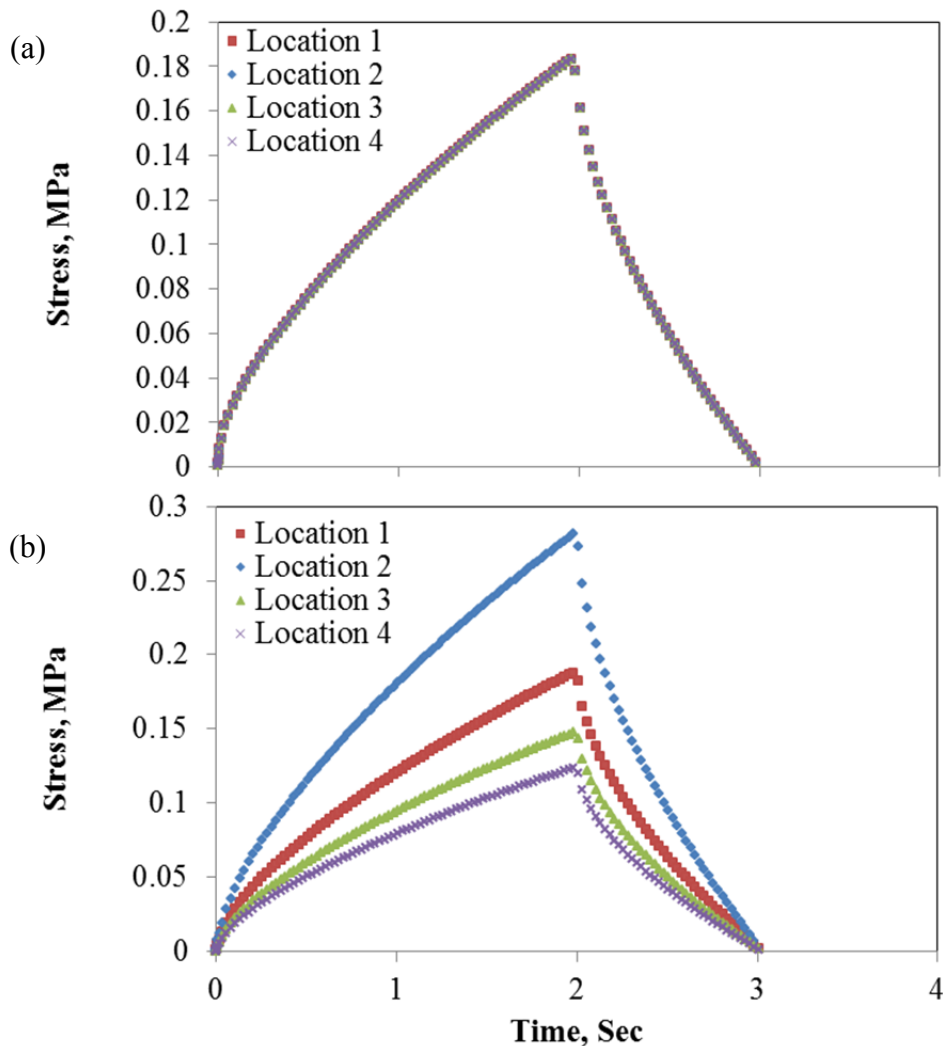


Figure 7-12 Effect of air voids on the FAM stress: (a) without air voids; (b) with air voids

A comparison of Figures 7-12 (a) and 7-12 (b) reveals that the stress release occurs at the same time for both model specimens: with and without air voids. For the four locations measured

on the specimen containing the air voids and for the same direction, the measured stress is completely released at the same time. However, the recovery rates at the four locations differed and were dependent on the maximum stress at each location. Air void distribution in asphalt mixtures can therefore be expected to influence the initiation and pattern of cracking and should be taken into account in asphalt performance predictions. The X-ray CT is a unique tool that facilitates the investigation of this design variable.

7.5 Summary and Conclusion

X-ray CT images have been used for the development of 3D microstructural FE modelling. The model was constructed as a means of acquiring an advanced understanding of the impact of internal structure on the mechanical responses associated with HMA. To this end, three asphalt mixture phases were included in the model: aggregate, FAM, and air voids. Images of the aggregate phase were extracted using XCAT software. FAM visuals were then obtained by subtracting the aggregate component from the image of the solid volume. Similarly, air voids were then subtracted from the FAM volume in order to generate depictions of the FAM with empty domains representing the air voids. All responses were measured in the FAM region because it represents a possible area where crack initiation and propagation occurs.

The findings indicate that 3D microstructural modelling provides a useful tool for investigating the effect of internal HMA structure on mechanical responses. The properties examined might not be detectable through typical experimental work, and the model thus provides an advanced understanding of material performance. The results of this work support the view that the relationship between FAM properties and the mechanical response is sensitive to the characteristics of other microstructural components. Both air voids and the aggregate modulus have a strong impact on the FAM with respect to response values and spatial distribution. The model also offers additional features, (e.g., sensitivity analysis of microstructure components and properties) that can lead to improved HMA pavement design and construction.

Chapter 8

Conclusions and Recommendations

8.1 Conclusions

The research reported in this thesis has included an investigation of typical and advanced characterization methods for providing a better understanding of hot mix asphalt (HMA) under fatigue which was then used to develop mitigation strategies. Overall, the findings presented in this thesis can be used as a guide for HMA mix design in order to achieve optimum performance and stiffness at a variety of temperatures. This chapter includes a summary of the work conducted and the conclusions to be drawn from the results of the extensive experimental work, the image-based analysis, and the development of the microstructural finite element (FE) model based on three-dimensional (3D) X-ray computed tomography (CT) imaging. Advanced understanding of HMA fatigue mechanism and recommendations for potential future research arising from this study are also discussed.

8.1.1 Experimental Work

The implementation of a full factorial experimental design enabled for the computation of the individual effects of asphalt binder type, aggregate type, and asphalt cement content on HMA fatigue, stiffness, and rutting characteristics. The ultimate goal was to identify the interactions between the binder and the aggregate at two binder levels in order to optimize HMA design in a manner that would provide longer fatigue life but have a minimal effect on rutting resistance. To achieve this objective, four-point bending testing, dynamic modulus testing, Hamburg wheel rut testing, and flow number testing were employed for evaluating the materials experimentally. The results of the experimental work and analysis revealed the following:

- Based on both the stiffness and PV damage approach, it was determined that the use of a high friction aggregate reduces HMA fatigue life. Conversely, the mixes produced with this type of aggregate also exhibited greater stiffness and enhanced rutting resistance. However, this behaviour might be minor or might disappear when the optimum binder content is increased by 0.5%.

- Although the two binders tested had been assigned identical performance grades (PG 64-28), one was modified so that it was softer than the neat binder in order to improve HMA fatigue resistance. The effect of using the PG Plus (PG 64-28D) binder, which satisfied the Ontario LS 299 modified binder specification, was found to be a significant improvement in the fatigue life of HMA mixes. This result matches the behaviour expected with respect to binder stiffness (G^*), but the overall approximate threefold increase varied substantially with different aggregate types and with the addition of a slightly greater amount of binder content: 0.5%.
- Maximum fatigue life performance was obtained when the optimum binder content with the extra level of binder content added was used with the SP 12.5 aggregate and the softer binder (PG Plus). The fatigue performance resulting from this combination was found to be 34 times better than the performance of the worst mix, which contained the high friction aggregate and the unmodified binder at the optimum binder content.
- Improvements in fatigue resistance were observed to have a negative impact on HMA stiffness and rutting resistance. However, depending on the effect of the variables studied and their combinations, even a mix that results in a 20 % to 58 % decrease in rutting resistance, as indicated by the HWRT rut depth and rate, would still provide an impressive increase in fatigue life.
- Mixes with both the modified binder (PG plus) and the additional 0.5% binder content were found to exhibit a decrease in both the HMA stiffness value and rutting resistance.
- A reasonable solution would be to add amount of binder to decrease the negative effect on fatigue performance when an aggregate with a rough texture is incorporated. For the materials used in this research, this strategy will produce mixes with acceptable levels of rutting resistance (maximum rut depth < 12.5 mm).
- The use of a high friction aggregate resulted in an 8 % to 42 % increase in HMA stiffness at 54 °C. While not statistically significant with respect to HWRT rut depth, the effect of the high friction aggregate was found to be significant with respect to rutting rate and total rutting depth. A flow number test was therefore necessary as a means of validating the effect of the high friction aggregate in relation to improvements in rutting resistance.

- The average increase in rutting depth for all mixes due to shear upheaval was found to be 57 % of the HWRT rut depth. To ensure a better assessment of rutting resistance, shear upheave measurements are therefore recommended.

8.1.2 Image-Based Analysis

Two-dimensional (2D) images were employed as a means of acquiring an understanding of the failure mechanism that occurs in rutting and its relationship with each characteristic of the individual components. SEM imaging was also used in order to explain how aggregate texture could alter HMA mix performance. The work conducted for this thesis also included the development and validation of an innovative framework for HMA fatigue characterization based on 3D X-ray CT images. The new method incorporates an advanced algorithm for establishing thresholding levels for asphalt beams before and after testing based on measured air voids and the distribution of aggregate colour intensities. Damage analyses were conducted for both the 2D image slices and the 3D volumetric characterization of the asphalt beam subjected to a four-point bending test. The following conclusions can be drawn based on the results and analysis:

- The 3D visuals of the aggregate surface obtained from the SEM images demonstrated the variability in the texture and the substantial impact it would have on the stiffness and performance of the HMA mixes. In contrast to the uniform amplitude texture displayed by the 12.5 aggregate, the high friction aggregate was characterized by irregular waves. The experimental and visual observations of the effect of the aggregate surface were consistent.
- Image analysis was shown to be a good indicator of HMA rutting based on the number of aggregate contacts, the total contact length, and the Internal Structure Index (ISI). Binder content significantly affected aggregate contacts and can also result in lower levels of rutting resistance. The image-based characteristics that were computed also demonstrated that a high friction aggregate offers superior packing characteristics, which were clearly observable in the laboratory test results, especially with respect to HMA stiffness and the

flow number. However, this conclusion is based on only two types of aggregate from two different sources.

- A 16-bit image is more appropriate than an 8-bit image for characterizing the interior structure of asphalt mixtures. This method provides a wide range of colour intensities and more accurate analysis because the error between the measured and predicted air voids is insignificant compared to the discrepancy resulting from the use of an 8-bit image.
- The air void distribution and damage in the asphalt beams tested was non-uniform along the beam length. The void percentage varied significantly, and no specific trend was observed. The correlation between air void distribution in asphalt beams and performance will be examined in future work.
- The proposed algorithm constitutes a valid method of calculating thresholding levels. While no changes were detected in the untested specimen, significant differences were evident in the tested beams.
- X-ray CT represents a promising tool for providing an understanding of the complexity of HMA and for quantifying damage. Both 2D slice analysis and 3D volume analysis of void particles have been successfully employed as a means of demonstrating damage.
- For the case studies presented in this thesis, significant differences were observed with respect to the four beams tested. Compared to the other beams, Beam 1 which made of 12.5 PG 64-28 at optimum binder content exhibited the greatest damage and the shortest fatigue life.

8.1.3 Microstructural FE Modelling Based on Three-Dimensional X-ray CT Imaging

The developed 3D microstructural FE model based on X-ray CT represents an efficient tool for providing advance information about asphalt microstructure because of its ability to indicate the effect on the predicted response that results from the shape, distribution, and properties of microstructural components. This modelling approach can provide an enhanced understanding of the contribution of each individual component to the overall response of the mixture. In general, the new model can reflect the influence of air voids and aggregate on the predicted response. The

findings from the application of the 3D heterogeneous model can be used as a guide for improving asphalt design and construction methods. Specific conclusions are as follows:

- Microstructural modelling facilitates the incorporation of the effects of air void distribution, aggregate packing, and mechanical characteristics into the calculation of the predicted response.
- The aggregate contributes significantly to the overall response of the mixture, particularly with respect to recovery rate, because it impacts the viscous nature of the material. Higher levels of aggregate stiffness induce greater stress in the mixture and a faster recovery rate during the unloading stage.
- Both the aggregate and the air voids significantly influence the response of the mixture, with respect not only to the values but also to the distribution. The presence of these components in the mixture lead to local stress concentrations that can be expected to produce local damage even though the overall response of the mixture may still be structurally adequate.
- The maximum stress on the FAM modelled with air voids was approximately 1.5 times higher than that on the FAM without air voids. However, for the same loading pattern, although the rates differed, both cases exhibited full stress recovery at the same time.
- When air voids are considered as empty domains, FAM stress results show a more than twofold variation in the levels for four close locations. The stress recovery rate differs by location and is dependent on the maximum local stress at each point. However, for all locations, full stress release occurs at the same instant.

8.2 Advanced Understanding of the HMA Fatigue Mechanism

The purpose of this section is to explain how the three different approaches in this research: FE microstructural model, the image-based analysis, and the experimental fatigue characterization respectively are related to each other. The HMA is a complex material and thus it is difficult to investigate the effect of all of the design variables. The conventional experimental work alone is insufficient for providing a complete understanding of the HMA fatigue mechanism. Therefore, the FE microstructural models and image-based analysis were utilized.

8.2.1 Experimental fatigue life

The HMA fatigue damage initiates and propagates due to the deterioration of the materials under cyclic loading. The damage mechanism is dependent on numerous control variables. The results of the experimental work revealed the effect of the type of aggregate, type of binder, and binder content on the HMA fatigue mechanism both individually and in combination. Each design variable can produce a specific positive or negative effect on fatigue life based on how it affects the deterioration of the material properties. For this study, the materials were selected in order to provide a wide range of fatigue life based on the interactions of the design variables. Two of the aggregates chosen were anticipated to have different frictional characterizations so that the effect of frictional properties could be verified for both types of binders: modified (soft) and unmodified (stiff). The results showed that a rough aggregate texture produced stiff mixes and reduced the fatigue life of HMA mixes. The use of a SBS polymer modified binder resulted in an improvement in addition when the binder content was increased by 0.5% were found to significantly increase the HMA mixes fatigue life. In summary, using an aggregate with a smooth texture, increasing binder content, and employing a SBS modified (soft) binder are effective solutions for improving HMA design in order to achieve better resistance to fatigue damage.

8.2.2 Image-based analysis

Image-based analysis offers advanced methods for understanding the asphalt fatigue mechanism. For example, the SEM was employed as a tool for producing high-resolution images of the texture of the aggregate, a characteristic that cannot be investigated through typical laboratory tests. Images of two aggregates were compared under identical scanning conditions. The findings were applied to explain why fatigue life was reduced when a rough aggregate was used, which resulted in changes in the surface area of the aggregate and the thickness of the coating.

The x-ray CT was also employed to assist with the quantification of fatigue damage and air void distributions. This method provided two unique benefits. First, it avoided the assumptions underlying typical evaluation methods with respect to the microstructure of the HMA. Second, it provided an indication of the distribution of the damage rather than producing one measured value in the experimental results. This method also identified the locations of the

maximum damage and can be used for comparing and ranking the performance of a variety of HMA mixes.

8.2.3 Microstructural FE Modelling

The mechanical responses of the asphalt mixtures studied were computed by incorporating the observed microstructure into an FE model. The new model included three phases: aggregate, binder, and air voids. A microstructural model enables the simulation of a variety of tests and the quantification of the effect of HMA design variables. The relation between the experimental results and the developed FE model can be summarized as follows:

- The model evaluated the expected influence of air voids on the predicted stress distribution in the mixture. This advantage can be used for comparing different compaction methods in order to determine the suitable compaction practice.
- The predictions of stress under compression load produced by the developed model were similar to the outcomes provided by a common experimental setup. However, the model can also be used to evaluate different loading modes and frequencies to offer an enhanced understanding of material performance without the requirement for any additional experimental work.
- The FE model can be used for measuring new characteristics that cannot otherwise be easily investigated or even addressed in laboratory testing, such as the effect of the aggregate modulus of elasticity when the aggregate structure is constant.
- The microstructural FE model incorporated a real arrangement and shape of aggregate particles, as in compacted specimens, it can be used for investigating the effect of aggregate characteristics on performance.
- Changing the FAM viscoelastic characteristics enables the FE model to be used for exploring the effects of the binder type with respect to identical aggregate structures.

8.3 Future Work

The following represent possible avenues of further investigation:

- With respect to long-term follow-up, it is recommended that the HMA surface course mixes described in this thesis be considered for future research in order to monitor their performance and to measure tensile strain under actual traffic loads and environmental conditions. Such investigations would enable full verification of the hypothesis that producing surface course HMA materials that provide longer fatigue life with minimal effect on other types of distress would reduce the severity of distresses and the associated costs.
- As a non-destructive technique, X-ray CT could be considered for use with 3D characterizations in order to provide a better understanding of HMA rutting performance under the wheel path.
- New indices could be established for quantifying and comparing aggregate texture based on the very high resolution provided by SEM images.
- The developed 3D microstructural model could be used to simulate a variety of testing and loading conditions, such as temperature.
- Analyze asphalt responses with 3D microstructures FE modelling that involves complicated constitutive models such as those required for representing nonlinear viscoelastic properties.
- Investigate the effect of FAM and aggregate adhesion on the predicted response of the mixture.

Publications

Journal Papers

1. Shaheen, M., Al-Mayah, A., and Tighe, S. (2015). "Effects of High Friction Aggregate and PG Plus Binder on Rutting Resistance of Hot Mix Asphalt Mixtures." International Journal of Pavement Engineering: 1-11
2. Shaheen, M., Al-Mayah, A., and Tighe, S. (2015) "Optimization of Hot Mix Asphalt Surface Course Mix Design for Fatigue Resistance: PG Plus and High Friction Aggregate." Journal of Material in Civil engineering, 04015172.
3. Shaheen, M., Al-Mayah, A., and Tighe, S. (2015). " A Novel Method for Evaluating Hot Mix Asphalt Fatigue Damage: X-Ray Computed Tomography. " Journal Of Building and Construction Materials: under review

Conference Papers

4. Shaheen, M., Al-Mayah, A., Tighe, S., and Safiuddin, M. (2013) "Fatigue Damage Evolution in Micro and Macrostructure of Asphalt Beam Tested under Four Point Bending." 58th Annual Conference of the Canadian Technical Asphalt Association (CTAA), Newfoundland, Canada.
5. Shaheen, M., Al-Mayah, A., Tighe, S. (2014) "Evaluating the Potential for Hot Mix Asphalt Rutting Performance Using Laboratory and Digital Imaging Technique." Transportation Association of Canada (TAC) Conference, Montreal, Ontario, Canada.
6. Shaheen, M., Al-Mayah, A., and Tighe, S. (2015) "Visualization and Quantification of Hot Mix Asphalt Characteristics using X-Ray Computed Tomography." 60th Annual Conference of the Canadian Technical Asphalt Association (CTAA), Ottawa, Canada.
7. Shaheen, M., Al-Mayah, A., and Tighe, S. (2015) " Improving the Fatigue Resistance for Hot Mix Asphalt Surface Course Mix" 60th Annual Conference of the Canadian Technical Asphalt Association (CTAA), Ottawa, Canada.

References

- AASHTO-T 321 (2007). "Standard Method of Test for Determining the Fatigue Life of Compacted Hot-Mix Asphalt (HMA) Subjected to Repeated Flexural Bending." *American Association of State Highway and Transportation Officials, Washing-ton, DC.*
- AASHTO-T 324 (2008). "Hamburg Wheel-Track Testing of Compacted Hot Mix Asphalt (HMA)." *American Association of State Highway and Transportation Officials, Washing-ton, DC.*
- AASHTO-TP 62-07 (2007). " Standard Method of Test for Determining Dynamic Modulus of Hot-Mix Asphalt Concrete Mixtures." *American Association of State Highway and Transportation Officials, Washing-ton, DC.*
- Adhikari, S., Shen, S., and You, Z. (2009). "Evaluation of fatigue models of hot-mix asphalt through laboratory testing." *Transportation Research Record: Journal of the Transportation Research Board*, 2127(1), 36-42.
- Ahlich, R. C. (1996). "Influence of aggregate gradation and particle shape/texture on permanent deformation of hot mix asphalt pavements." DTIC Document.
- Al-Khateeb, G., and Shenoy, A. (2004). "A distinctive fatigue failure criterion." *Journal of the Association of Asphalt Paving Technologists*, 73, 585-622.
- Al-Suhaibani, A., Al-Mudaiheem, J., and Al-Fozan, F. (1992). "Effect of filler type and content on properties of asphalt concrete mixes." *Effects of aggregates and mineral "filler" s on asphalt mixtures performance. American Society for Testing and Materials, ASTM STP*, 1147, 107-130.
- Ameri, M., Sheikhmotevali, A. H., and Fasihpour, A. (2014). "Evaluation and comparison of flow number calculation methods." *Road Materials and Pavement Design*, 15(1), 182-206.
- Aragao, F. (2011). "Computational microstructure modeling of asphalt mixtures subjected to rate-dependent fracture." Ph.D Thesis, Lincoln, Nebraska.
- Bahia, H. U., and Faheem, A. F. (2007). "Using the Superpave gyratory compactor to estimate rutting resistance of hot-mix asphalt." *Transportation Research E-circular, Transportation Research Board, Washington, DC*, 45-61.
- Bessa, I. S., Branco, V. T. C., Soares, J. B., and Neto, J. A. N. (2014). "Aggregate Shape Properties and Their Influence on the Behavior of Hot-Mix Asphalt." *Journal of Materials in Civil Engineering*.
- Breakah, T. (2009). "Stochastic finite element analysis of moisture damage in hot mix asphalt." Ph.D Thesis, Iowa State University, Ames, Iowa.

- Cannone Falchetto, A., Montepara, A., Tebaldi, G., and Marasteanu, M. O. (2012). "Microstructural and rheological investigation of asphalt mixtures containing recycled asphalt materials." *Construction and Building Materials*, 35, 321-329.
- Carpenter, S. H., and Shen, S. (2006). "Dissipated energy approach to study hot-mix asphalt healing in fatigue." *Transportation Research Record: Journal of the Transportation Research Board*, 1970(1), 178-185.
- Chen, J. (2011). "Discrete Element Method (DEM) Analyses for Hot-Mix Asphalt (HMA) Mixture Compaction." Ph.D Thesis, University of Tennessee, Knoxville.
- Clyne, T. R., Li, X., Marasteanu, M. O., and Skok, E. L. (2003). "Dynamic and resilient modulus of Mn/DOT asphalt mixtures."
- Coenen, A. R., Kutay, M. E., Sefidmazgi, N. R., and Bahia, H. U. (2012). "Aggregate structure characterisation of asphalt mixtures using two-dimensional image analysis." *Road Materials and Pavement Design*, 13(3), 433-454.
- Coleri, E., Harvey, J. T., Yang, K., and Boone, J. M. (2012). "Development of a micromechanical finite element model from computed tomography images for shear modulus simulation of asphalt mixtures." *Construction and Building Materials*, 30, 783-793.
- Collop, A. C., McDowell, G. R., and Lee, Y. (2007). "On the use of discrete element modelling to simulate the viscoelastic deformation behaviour of an idealized asphalt mixture." *Geomechanics and Geoengineering*, 2(2), 77-86.
- Collop, A. C., McDowell, G. R., and Lee, Y. W. (2006). "Modelling dilation in an idealised asphalt mixture using discrete element modelling." *Granular Matter*, 8(3-4), 175-184.
- Dai, Q. (2010). "Three-dimensional micromechanical finite-element network model for elastic damage behavior of idealized stone-based composite materials." *Journal of Engineering Mechanics*, 137(6), 410-421.
- Dai, Q. (2011). "Two- and three-dimensional micromechanical viscoelastic finite element modeling of stone-based materials with X-ray computed tomography images." *Construction and Building Materials*, 25(2), 1102-1114.
- Dai, Q., Sadd, M. H., and You, Z. (2006). "A micromechanical finite element model for linear and damage-coupled viscoelastic behaviour of asphalt mixture." *International journal for numerical and analytical methods in geomechanics*, 30(11), 1135-1158.
- Dai, Q., and You, Z. (2007). "Micromechanical finite element framework for predicting viscoelastic properties of asphalt mixtures." *Materials and Structures*, 41(6), 1025-1037.

- Dai, Q., and You, Z. (2008). "Micromechanical Finite Element Models for Micro-Damage and Complex Constitutive Behavior of Asphalt Mixes." *ASCE*, 867-876.
- Dai, Q., You, Z., and Sadd, M. (2006). "A Micromechanical Viscoelasto-Plastic Model for Asphalt Mixture." *Asphalt Concrete*, 12-20.
- Dongré, R., D'Angelo, J., and Copeland, A. (2009). "Refinement of Flow Number as Determined by Asphalt Mixture Performance Tester." *Transportation Research Record: Journal of the Transportation Research Board*, 2127(1), 127-136.
- El-Hakim, M. (2013). "A structural and economic evaluation of perpetual pavements a Canadian perspective." University of Waterloo, Ph.D.
- Elseifi, M. A., Al-Qadi, I. L., Yang, S.-H., and Carpenter, S. H. (2008). "Validity of asphalt binder film thickness concept in hot-mix asphalt." *Transportation Research Record: Journal of the Transportation Research Board*, 2057(1), 37-45.
- Elseifi, M. A., Mohammad, L. N., Kassem, E., Ying, H., and Masad, E. (2011). "Quantification of Damage in the Dynamic Complex Modulus and Flow Number Tests Using X-Ray Computed Tomography." *Journal of Materials in Civil Engineering*, 23(12), 1687-1696.
- Elseifi, M. A., Mohammad, L. N., Ying, H., and Cooper, S. (2012). "Modeling and evaluation of the cracking resistance of asphalt mixtures using the semi-circular bending test at intermediate temperatures." *Road Materials and Pavement Design*, 13(sup1), 124-139.
- Falchetto, A. C. (2011). "Investigation of Low Temperature Properties of Asphalt Mixture Containing Recycled Asphalt Materials." Parma, Gennaio.
- Ghuzlan, K. A., and Carpenter, S. H. (2002). "Traditional fatigue analysis of asphalt concrete mixtures." *Urbana*, 51, 61801.
- Ghuzlan, K. A., and Carpenter, S. H. (2006). "Fatigue damage analysis in asphalt concrete mixtures using the dissipated energy approach." *Canadian Journal of Civil Engineering*, 33(7), 890-901.
- Gonzalez, R. C., Woods, R. E., and Eddins, S. L. (2004). *Digital image processing using MATLAB*, Gatesmark Publishing Knoxville.
- Gopalakrishnan, K., Inanc, F., and Ceylan, H. (2007). "Using X-ray computed tomography to study paving materials." *Proceedings of the ICE - Construction Materials*, 160(1), 15-23.
- Harman, T. (2001). "Using the dynamic modulus test to assess the mix strength of HMA." *Public Roads*, 64(6).

- Harvey, J. T., and Tsai, B.-W. (1996). "Effects of asphalt content and air void content on mix fatigue and stiffness." *Transportation Research Record: Journal of the Transportation Research Board*, 1543(1), 38-45.
- Hassan, N. A., Airey, G. D., and Hainin, M. R. (2014). "Characterisation of micro-structural damage in asphalt mixtures using image analysis." *Construction and Building Materials*, 54, 27-38.
- Hesp, S. A. (2006). "Development of an improved asphalt binder specification testing approach." No. TRB-NCHRP-104. Final Report for Highway IDEA Project 104. Kingston, Ontario
- Hintz, C., Velasquez, R., Johnson, C., and Bahia, H. (2011). "Modification and validation of linear amplitude sweep test for binder fatigue specification." *Transportation Research Record: Journal of the Transportation Research Board*, 2207(1), 99-106.
- Hossain, M. I., and Tarefder, R. A. (2012). "Determination of Adhesive and Cohesive Damages in Asphalt Concrete by Finite Element Method." *International Journal of Civil Engineering and Structures*, 1(1).
- Hu, J., Qian, Z., Liu, Y., and Zhang, M. (2015). "High-temperature failure in asphalt mixtures using micro-structural investigation and image analysis." *Construction and Building Materials*, 84, 136-145.
- Izadi, A., Bhasin, A., and Motamed, A. (2011). "Designing Fine Aggregate Mixtures to Evaluate Fatigue Crack Growth in Asphalt Mixtures." Southwest Region University Transportation Center, Center for Transportation Research, University of Texas at Austin.
- Jeong, M. G., Loulizi, A., and Flintsch, G. W. (2006). "Laboratory Validation of Viscoelastic Interconversion for Hot Mix Asphalt." *Analysis of Asphalt Pavement Materials and Systems: Engineering Methods: Proceedings of the Symposium on the Mechanics of Flexible Pavements*, Boulder, Colorado, ASCE Publications, 87.
- Kanitpong, K., and Bahia, H. (2005). "Relating adhesion and cohesion of asphalts to the effect of moisture on laboratory performance of asphalt mixtures." *Transportation Research Record: Journal of the Transportation Research Board*, 1901(1), 33-43.
- Kim, J., Sholar, G. A., and Kim, S. (2008). "Determination of accurate creep compliance and relaxation modulus at a single temperature for viscoelastic solids." *Journal of Materials in Civil Engineering*, 20(2), 147-156.

- Kuo, C.-Y., and Freeman, R. B. (2000). "Imaging indices for quantification of shape, angularity, and surface texture of aggregates." *Transportation Research Record: Journal of the Transportation Research Board*, 1721(1), 57-65.
- Kutay, M. E., Arambula, E., Gibson, N., and Youtcheff, J. (2010). "Three-dimensional image processing methods to identify and characterise aggregates in compacted asphalt mixtures." *International Journal of Pavement Engineering*, 11(6), 511-528.
- Leng, Z., Ozer, H., Al-Qadi, I. L., and Carpenter, S. H. (2008). "Interface bonding between hot-mix asphalt and various Portland cement concrete surfaces: laboratory assessment." *Transportation Research Record: Journal of the Transportation Research Board*, 2057(1), 46-53.
- Li, Q., Ni, F., Gao, L., Yuan, Q., and Xiao, Y. (2014). "Evaluating the rutting resistance of asphalt mixtures using an advanced repeated load permanent deformation test under field conditions." *Construction and Building Materials*, 61, 241-251.
- Liu, Y., and You, Z. (2009). "Visualization and simulation of asphalt concrete with randomly generated three-dimensional models." *Journal of Computing in Civil Engineering*, 23(6), 340-347.
- Lytton, R. L., Uzan, J., Fernando, E. G., Roque, R., Hiltunen, D., and Stoffels, S. M. (1993). *Development and validation of performance prediction models and specifications for asphalt binders and paving mixes*, Strategic Highway Research Program.
- Masad, E. (2003). "The development of a computer controlled image analysis system for measuring aggregate shape properties." No. NCHRP-IDEA Project 77.
- Masad, E. (2007). *Test methods for characterizing aggregate shape, texture, and angularity*, Transportation Research Board.
- Masad, E., Jandhyala, V., Dasgupta, N., Somadevan, N., and Shashidhar, N. (2002). "Characterization of air void distribution in asphalt mixes using X-ray computed tomography." *Journal of materials in civil engineering*, 14(2), 122-129.
- Masad, E., and Kutay, M. E. (2012). "Characterization of the Internal Structure of Asphalt Mixtures." *Trans. Res. Circ. E-C161, Transportation Research Board, Washington, DC*, 2-16.
- Masad, E., Muhunthan, B., Shashidhar, N., and Harman, T. (1999). "Internal structure characterization of asphalt concrete using image analysis." *Journal of computing in civil engineering*, 13(2), 88-95.
- Masad, E., Muhunthan, B., Shashidhar, N., and Harman, T. (1999). "Quantifying laboratory compaction effects on the internal structure of asphalt concrete." *Transportation Research Record: Journal of the Transportation Research Board*, 1681(1), 179-185.

- Masad, E., Olcott, D., White, T., and Tashman, L. (2001). "Correlation of fine aggregate imaging shape indices with asphalt mixture performance." *Transportation Research Record: Journal of the Transportation Research Board*, 1757(1), 148-156.
- Masad, E., Tashman, L., Little, D., and Zbib, H. (2005). "Viscoplastic modeling of asphalt mixes with the effects of anisotropy, damage and aggregate characteristics." *Mechanics of Materials*, 37(12), 1242-1256.
- Masad, E. A., Little, D. N., Tashman, L., Saadeh, S., Al-Rousan, T., and Sukhwani, R. (2003). "Evaluation of aggregate characteristics affecting HMA concrete performance." Texas Transportation Institute, The Texas A&M University System.
- Meininger, R. C. (1992). *Effects of aggregates and mineral fillers on asphalt mixture performance*, ASTM International.
- Mo, L. T., Hurman, M., Wu, S. P., and Molenaar, A. A. A. (2008). "2D and 3D meso-scale finite element models for ravelling analysis of porous asphalt concrete." *Finite Elements in Analysis and Design*, 44(4), 186-196.
- Moaveni, M., Mahmoud, E., Ortiz, E. M., Tutumluer, E., and Beshears, S. (2014). "Use of Advanced Aggregate Imaging Systems to Evaluate Aggregate Resistance to Breakage, Abrasion, and Polishing." *Transportation Research Record: Journal of the Transportation Research Board*, 2401(1), 1-10.
- Moon, K. H., Falchetto, A. C., Wistuba, M. P., and Jeong, J. H. (2015). "Analyzing Aggregate Size Distribution of Asphalt Mixtures Using Simple 2D Digital Image Processing Techniques." *Arabian Journal for Science and Engineering*, 1-18.
- Muniandy, R., Akhir, N. A. B. C. M., Hassim, S., and Moazami, D. (2014). "Laboratory fatigue evaluation of modified and unmodified asphalt binders in Stone Mastic Asphalt mixtures using a newly developed crack meander technique." *International Journal of Fatigue*, 59, 1-8.
- NCHRP (2002). *Contributions of Pavement Structural layers to Rutting of Hot Mix Asphalt Pavements*, Transportation Research Board, Washington DC, USA.
- NCHRP (2004). *Guide for Mechanistic-Empirical Design of New and Rehabilitated Pavement Structures, Part 3: Design Analysis, Chapter 3: Design of New and Reconstructed Flexible Pavements*, Transportation Research Board, Washington DC, USA.
- NCHRP (2006). *Aggregate Tests for Hot-Mix Asphalt Mixtures Used in Pavements*, Transportation Research Board, Washington DC, USA.

- NCHRP (2011). *A Manual for Design of Hot Mix Asphalt with Commentary*, Transportation Research Board, Washington DC, USA.
- Neto, S. A. D., Farias, F., and Pais, J. C. (2009). "Change in fatigue behavior of asphalt hot mixes produced with asphalt rubber binders." *2nd Workshop on Four Point Bending*, Pais (ed.), University of Minho. ISBN 978-972-8692-42-1.
- Neubauer, O., and Partl, M. N. (2004). "Impact of binder content on selected properties of stone mastic asphalt." Paper No.93, Proceedings of the 3rd Eurasphalt and Eurobitume Congress Held Vienna, p.3-29.
- Olidis, C., and Hein, D. (2004). "Guide for the Mechanistic-Empirical Design of New and Rehabilitated Pavement Structures Materials Characterization: Is Your Agency Ready." *2004 Annual Conference of the Transportation Association of Canada*.
- Onyango, M. A. (2009). "Verification of mechanistic prediction models for permanent deformation in asphalt mixes using accelerated pavement testing."
- OPSS1003 (2013). "Material Specification for Aggregates – Hot Mix Asphalt." Ontario Provincial Standard Specification (OPSS), Ontario Ministry of Transportation, Ontario
- Park, S., and Schapery, R. (1999). "Methods of interconversion between linear viscoelastic material functions. Part I—A numerical method based on Prony series." *International Journal of Solids and Structures*, 36(11), 1653-1675.
- Partl, M. N., Bahia, H. U., Canestrari, F., de la Roche, C., Di Benedetto, H., Piber, H., and Sybilski, D. (2012). *Advances in interlaboratory testing and evaluation of bituminous materials: state-of-the-art report of the RILEM Technical Committee 206-ATB*, Springer Science & Business Media.
- Pellinen, T. K., and Witczak, M. W. (2002). "Use of stiffness of hot-mix asphalt as a simple performance test." *Transportation Research Record: Journal of the Transportation Research Board*, 1789(1), 80-90.
- Prowell, B., et al. (2010). *Validating the Fatigue Endurance Limit for Hot Mix Asphalt*, Final NCHRP Rep. 646, NCHRP 9-38 Project, National Cooperative Highway Research Program, Washington DC, USA.
- Rushing, J. F., and Little, D. N. (2013). "Static Creep and Repeated Load as Rutting Performance Tests for Airport HMA Mix Design." *Journal of Materials in Civil Engineering*.
- Sadd, M. H., Dai, Q., Parameswaran, V., and Shukla, A. (2004). "Microstructural simulation of asphalt materials: Modeling and experimental studies." *Journal of materials in civil engineering*, 16(2), 107-115.

- Sefidmazgi, N. R. (2011). "Defining Effective Aggregate Skeleton in Asphalt Mixture Using Digital Imaging." University of Wisconsin.
- Sefidmazgi, N. R., and Bahia, H. U. (2014). "Effect of compaction conditions on aggregate packing using 2-dimensional image analysis and the relation to performance of HMA." *Materials and Structures*, 47(8), 1313-1324.
- Sefidmazgi, N. R., Tashman, L., and Bahia, H. (2012). "Internal structure characterization of asphalt mixtures for rutting performance using imaging analysis." *Road Materials and Pavement Design*, 13(sup1), 21-37.
- Shen, S., Airey, G. D., Carpenter, S. H., and Huang, H. (2006). "A Dissipated Energy Approach to Fatigue Evaluation." *Road Materials and Pavement Design*, 7(1), 47-69.
- Sun, L., Zhu, H., and Zhu, Y. (2013). "Two-Stage Viscoelastic-Viscoplastic Damage Constitutive Model of Asphalt Mixtures." *Journal of Materials in Civil Engineering*, 25(8), 958-971.
- Sun, W., Wang, L., and Tutumluer, E. (2012). "Image analysis technique for aggregate morphology analysis with two-dimensional Fourier transform method." *Transportation Research Record: Journal of the Transportation Research Board*, 2267(1), 3-13.
- TAC (2013). *Pavement Asset Design and Management Guide*, Prepared by University of Waterloo, Transportation Association of Canada, Ottawa
- Tangella, S. C. S. R., Craus, J., Deacon, J. A., and Monismith, C. L. (1990). "Summary report on fatigue response of asphalt mixtures." SHRPA/IR-90-011, Strategic Highway Research Program (SHRP), National Research Council (US), Washington, D.C.
- Tashman, L., Masad, E., D'Angelo, J., Bukowski, J., and Harman, T. (2002). "X-ray tomography to characterize air void distribution in superpave gyratory compacted specimens." *International Journal of Pavement Engineering*, 3(1), 19-28.
- Tayfur, S., Ozen, H., and Aksoy, A. (2007). "Investigation of rutting performance of asphalt mixtures containing polymer modifiers." *Construction and Building Materials*, 21(2), 328-337.
- TDOT (2011). *Pavement Design Guide*, Texas, USA
- Teymourpour, P., and Bahia, H. U. (2014). "Effects of Binder Modification on Aggregate Structure and Thermovolumetric Properties of Asphalt Mixtures." *Transportation Research Record: Journal of the Transportation Research Board*, 2445(1), 21-28.

- Thyagarajan, S., Tashman, L., Masad, E., and Bayomy, F. (2010). "The heterogeneity and mechanical response of hot mix asphalt laboratory specimens." *International Journal of Pavement Engineering*, 11(2), 107-121.
- Tighe, S. L., Jeffray, A., and Perraton, D. (2007). "Low Temperature Evaluation of Recycled Asphalt Shingles (RAS) Into Base Course Asphalt Mixes." University of Waterloo, P. 4.
- Tsai, B.-W., Harvey, J. T., and Monismith, C. L. (2001). "High temperature fatigue and fatigue damage process of aggregate-asphalt mixes."
- Uzarowski, L. (2006). "The development of asphalt mix creep parameters and finite element modeling of asphalt rutting." University of Waterloo, Waterloo, Ont.
- Uzarowski, L., Tighe, S. L., and Rothenburg, L. (2006). "The development of asphalt mix creep parameters and finite element modeling of asphalt rutting." *Fifty-Second Annual Conference of the Canadian Technical Asphalt Association (CTAA)*.
- VGStudio (2013). *Volume Graphics GmbH, editor. Reference Manual VGStudio Max Release 2.0*; <http://www.volumegraphics.com/en/products/vgstudio-max>.
- Wang, H., Hao, P., and You, Z. (2011). "Characterization of the Viscoelastic Property of Asphalt Mastic." *Reston, VA: ASCE Selected Papers from the 2011 Geohunan International Conference, Hunan, China/ d 20110000*, American Society of Civil Engineers.
- Wang, L. (2008). "Digital specimen and multiple functional digital tester technique for performance evaluation of asphalt mixes."
- Wang, L., Frost, J., and Shashidhar, N. (2001). "Microstructure study of WesTrack mixes from X-ray tomography images." *Transportation Research Record: Journal of the Transportation Research Board*, 1767(1), 85-94.
- Wang, L., Sun, W., Tutumluer, E., and Druta, C. (2013). "Evaluation of Aggregate Imaging Techniques for Quantification of Morphological Characteristics." *Transportation Research Record: Journal of the Transportation Research Board*, 2335(1), 39-49.
- Witczak, M., and Bari, J. (2004). "Development of a master curve (E*) database for lime modified asphaltic mixtures." *Arizona State University Research Report, Tempe (Arizona, USA): Arizona State University*.
- Witczak, M. W. (2007). *Specification criteria for simple performance tests for rutting*, Transportation Research Board.
- Yildirim, Y. (2007). "Polymer modified asphalt binders." *Construction and Building Materials*, 21(1), 66-72.

- Yildirim, Y., Jayawickrama, P. W., Hossain, M. S., Alhabshi, A., Yildirim, C., Smit, A. d. F., and Little, D. (2007). "Hamburg wheel-tracking database analysis." Final Report No. 0-1707-7, Texas Department of Transportation, Austin.
- Yin, A., Yang, X., Yang, S., and Jiang, W. (2011). "Multiscale fracture simulation of three-point bending asphalt mixture beam considering material heterogeneity." *Engineering Fracture Mechanics*, 78(12), 2414-2428.
- You, T., Abu Al-Rub, R., Masad, E., and Little, D. (2013). "Three-Dimensional Microstructural Modeling of Asphalt Concrete by Use of X-Ray Computed Tomography." *Transportation Research Record: Journal of the Transportation Research Board*(2373), 63-70.
- You, T., Abu Al-Rub, R. K., Darabi, M. K., Masad, E. A., and Little, D. N. (2012). "Three-dimensional microstructural modeling of asphalt concrete using a unified viscoelastic–viscoplastic–viscodamage model." *Construction and Building Materials*, 28(1), 531-548.
- You, Z., Adhikari, S., and Dai, Q. (2008a). "Three-dimensional discrete element models for asphalt mixtures." *Journal of engineering mechanics*, 134(12), 1053-1063.
- You, Z., Adhikari, S., Goh, S. W., and Dai, Q. (2008b). "Dynamic Moduli for ME Design of Asphalt Pavements." ASCE, 841-850.
- You, Z., and Buttlar, W. (2004). "Discrete element modeling to predict the modulus of asphalt concrete mixtures." *Journal of Materials in Civil Engineering*, 16(2), 140-146.
- Yue, Z. Q., and Morin, I. (1996). "Digital image processing for aggregate orientation in asphalt concrete mixtures." *Canadian Journal of Civil Engineering*, 23(2), 480-489.
- Zeilew, H. M., and Papagiannakis, A. T. (2007a). "A volumetrics thresholding algorithm for processing asphalt concrete X-ray CT images." *International Journal of Pavement Engineering*, 12(6), 543-551.
- Zeilew, H. M., Papagiannakis, A. T., and Masad, E. (2008). "Application of digital image processing techniques for asphalt concrete mixture images." *The 12th International Conference of International Association for Computer Methods and Advances in Geomechanics (IACMAG)*Goa, India, 119-124.
- Zhang, J., Sabouri, M., Guddati, M. N., and Kim, Y. R. (2013). "Development of a failure criterion for asphalt mixtures under fatigue loading." *Road Materials and Pavement Design*, 14(sup2), 1-15.
- Zhu, X.-y. (2013). "Influence of interfacial zone between asphalt mastic and aggregate on the elastic behavior of asphalt concrete." *Construction and Building Materials*, 49, 797-806.

Zhu, X.-y., Yang, Z.-x., Guo, X.-m., and Chen, W.-q. (2011). "Modulus prediction of asphalt concrete with imperfect bonding between aggregate–asphalt mastic." *Composites Part B: Engineering*, 42(6), 1404-1411.

Appendix A: Experimental Work

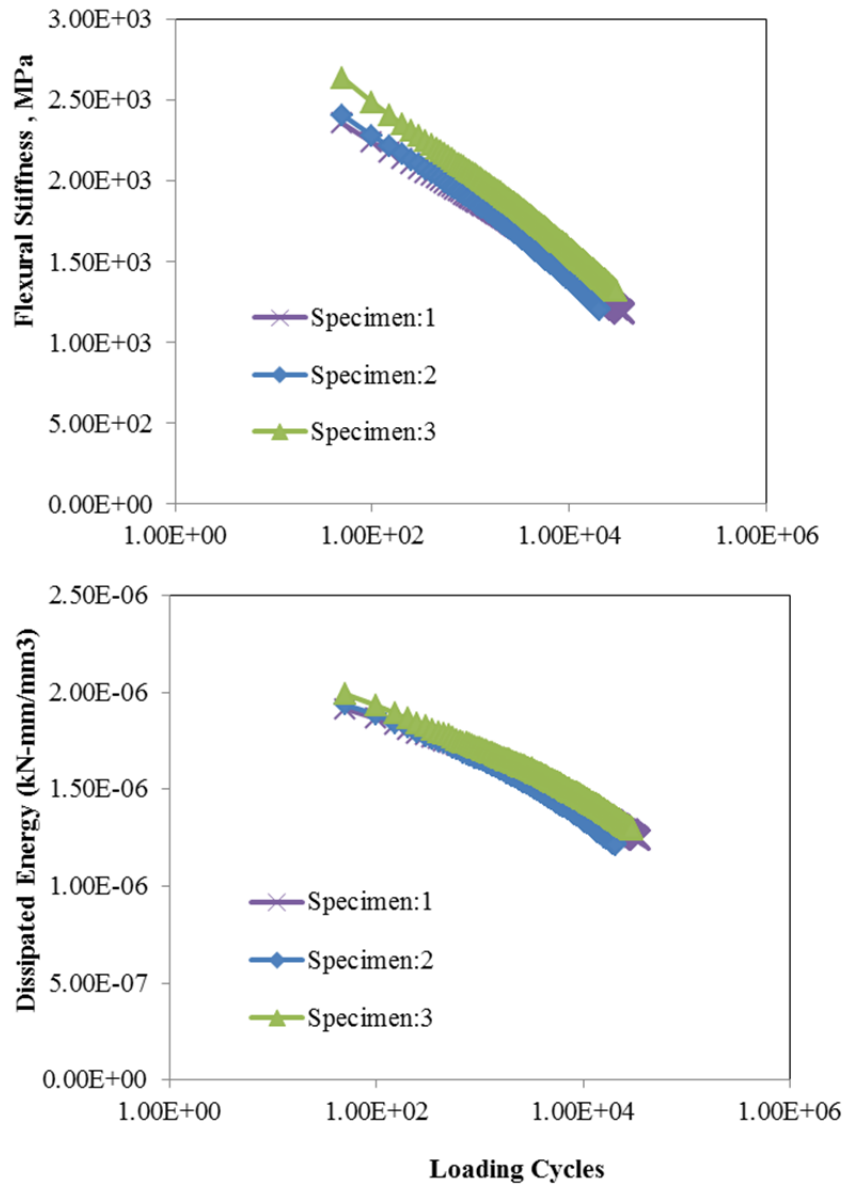


Figure A1 Fatigue test results: SP12.5 64-28 (opt.)

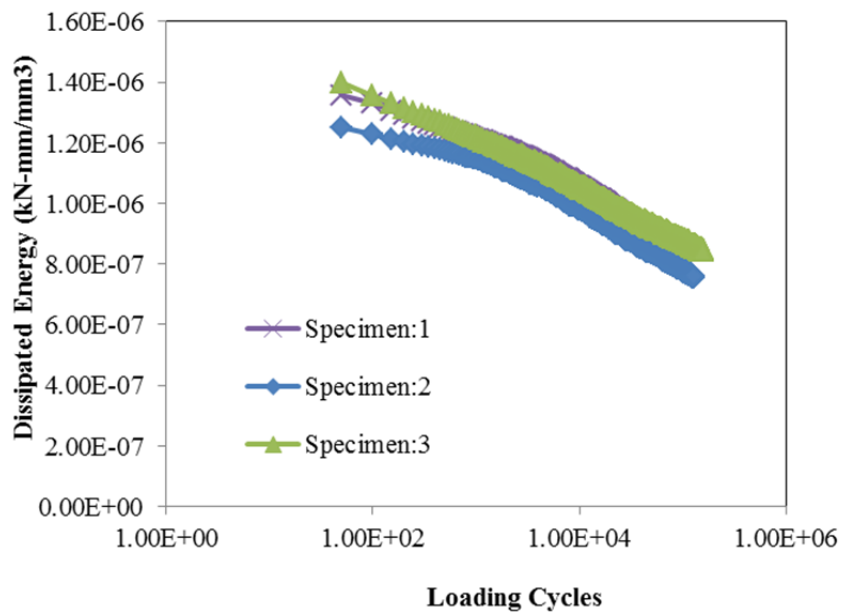
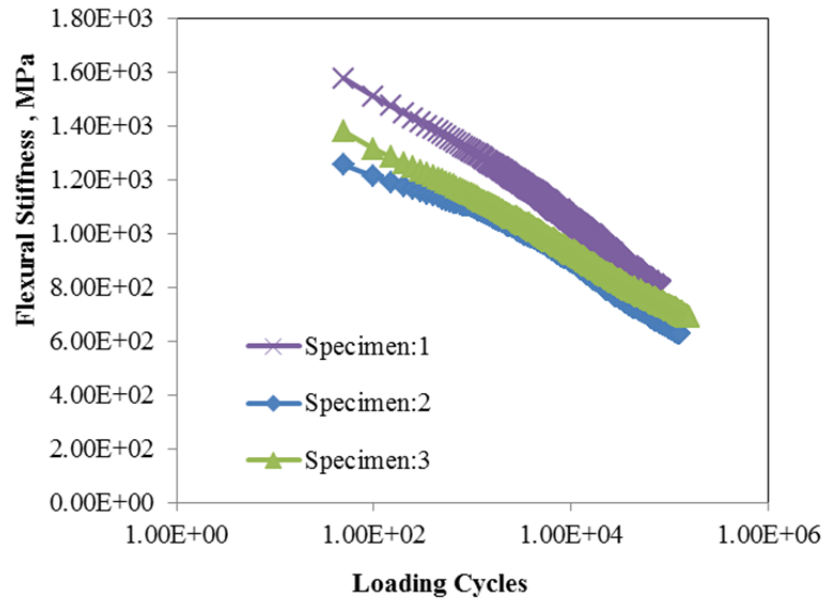


Figure A2 Fatigue test results: SP12.5 64-28 (opt.+0.5)

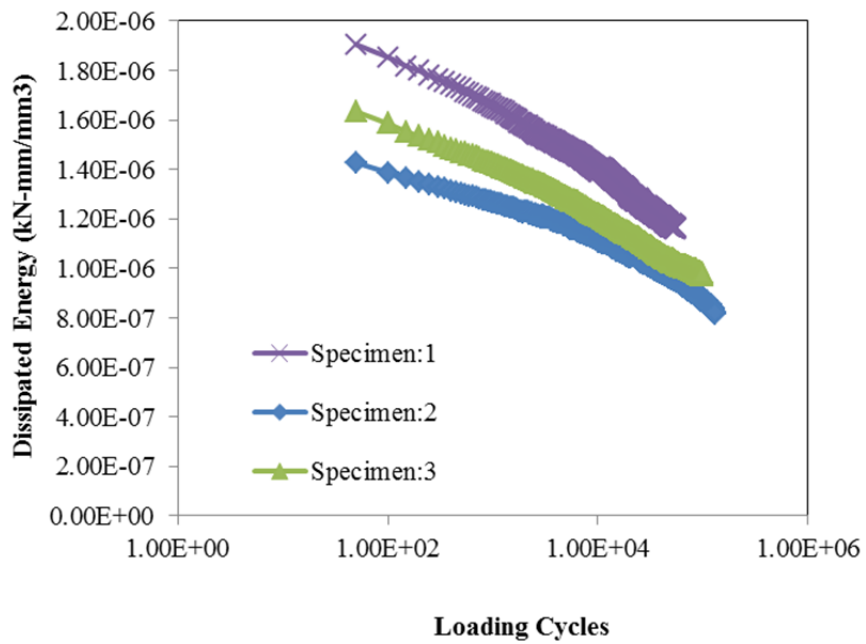
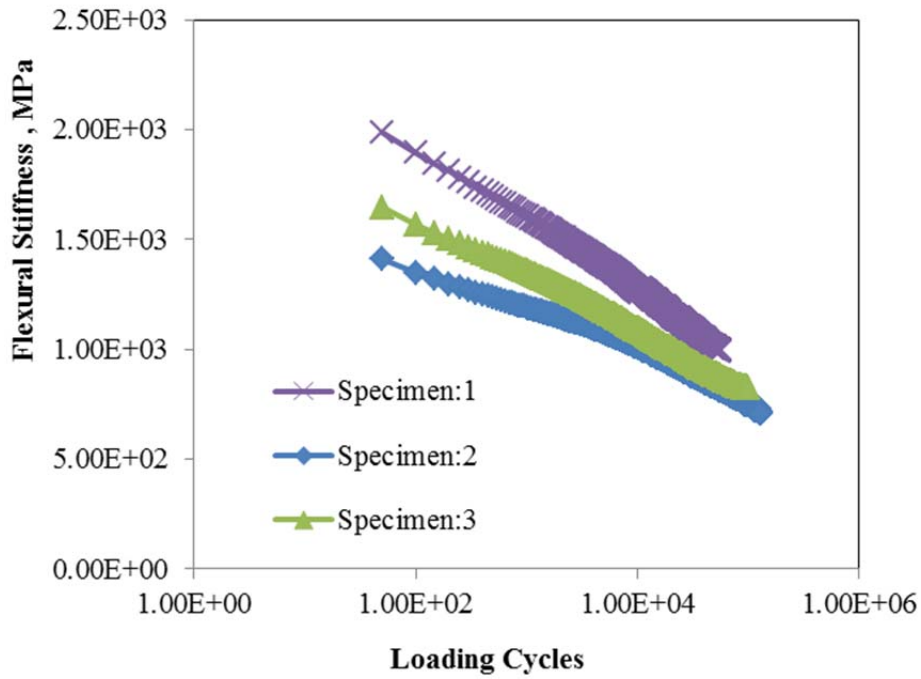


Figure A3 Fatigue test results: SP12.5 64-28 (opt.+0.5)

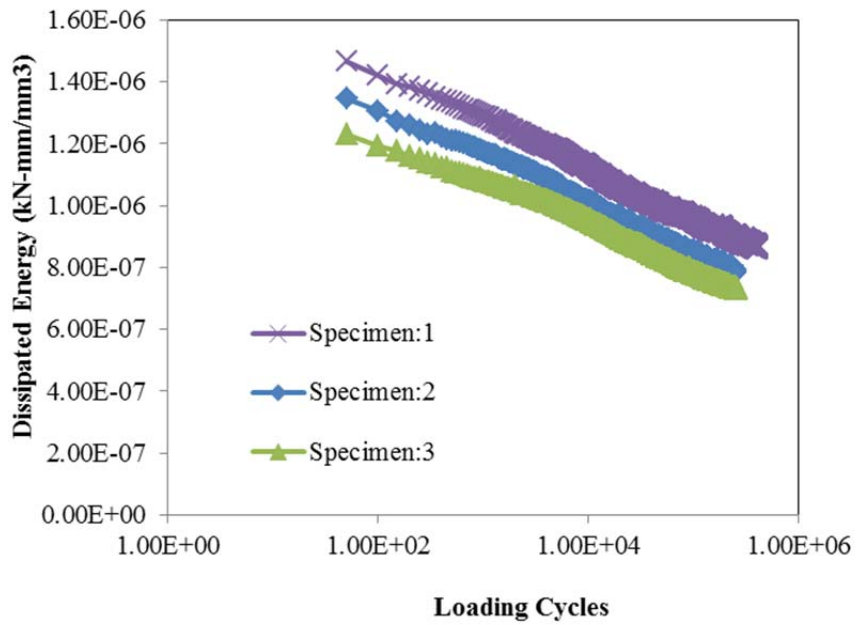
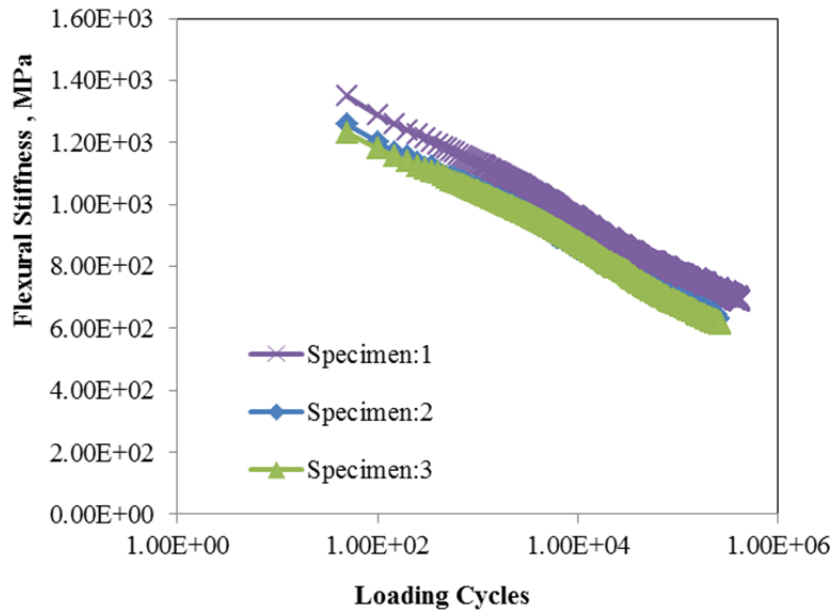


Figure A4 Fatigue test results: SP12.5 64-28 D (opt.+0.5)

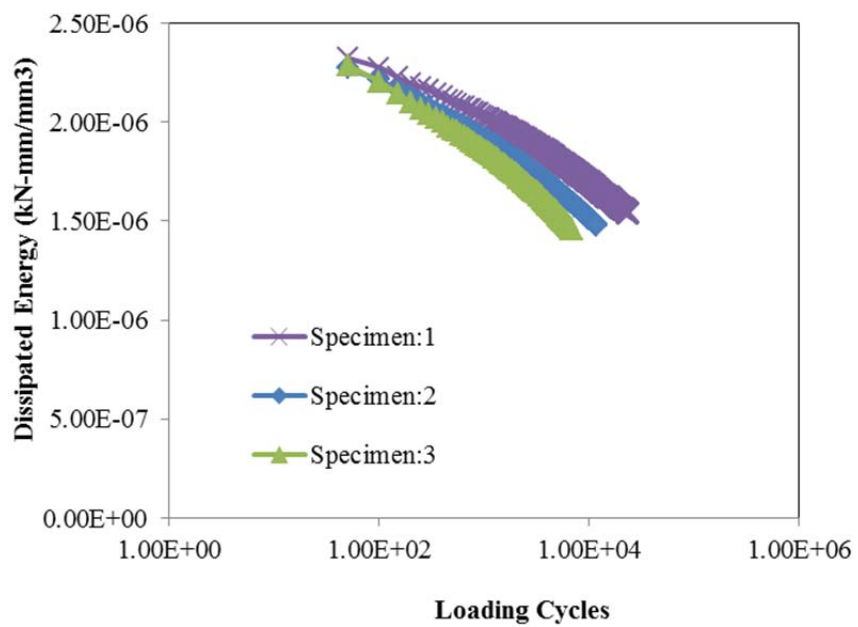
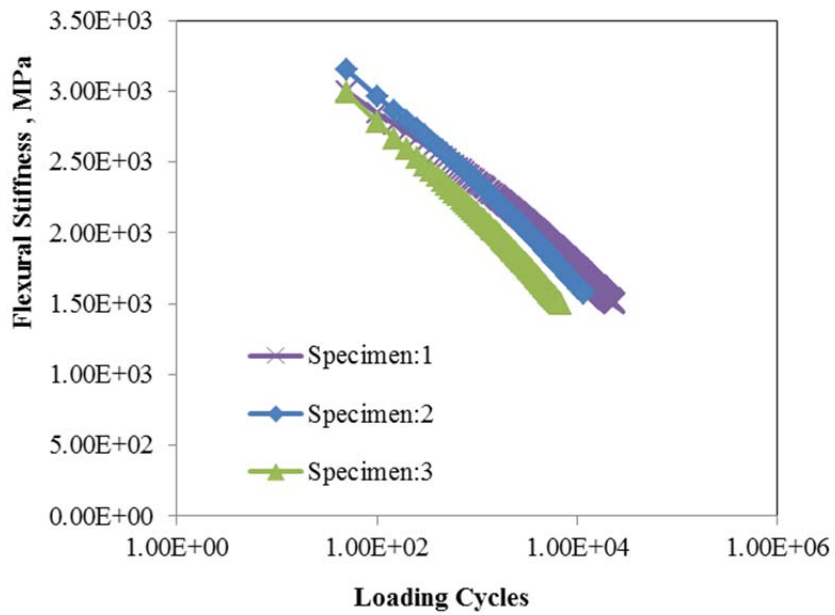


Figure A5 Fatigue test results: SP12.5FC2 64-28 (opt.)

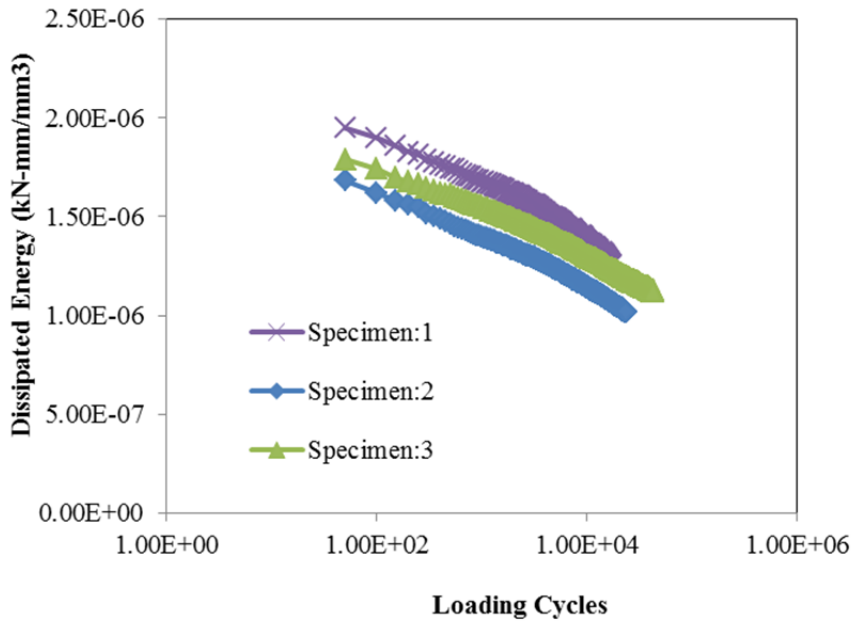
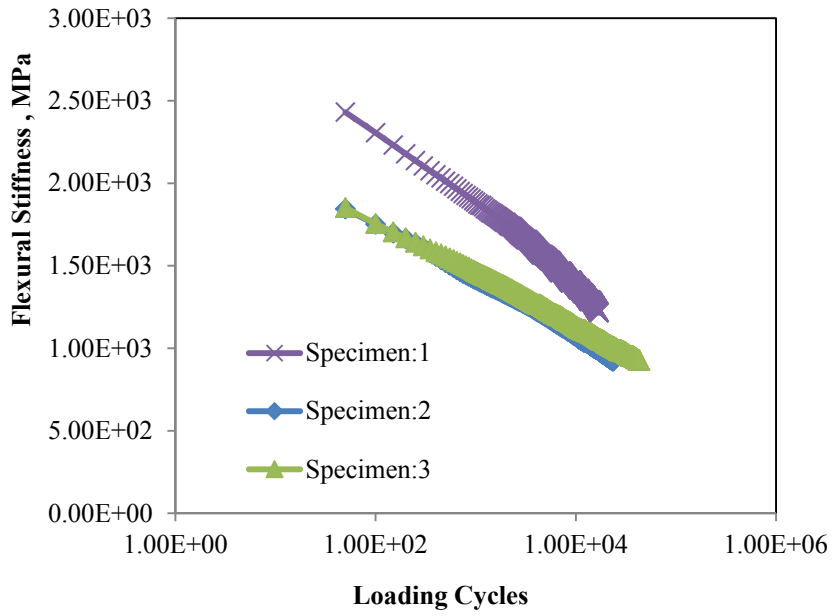


Figure A6 Fatigue test results: SP 12.5FC2 64-28 (opt.+0.5)

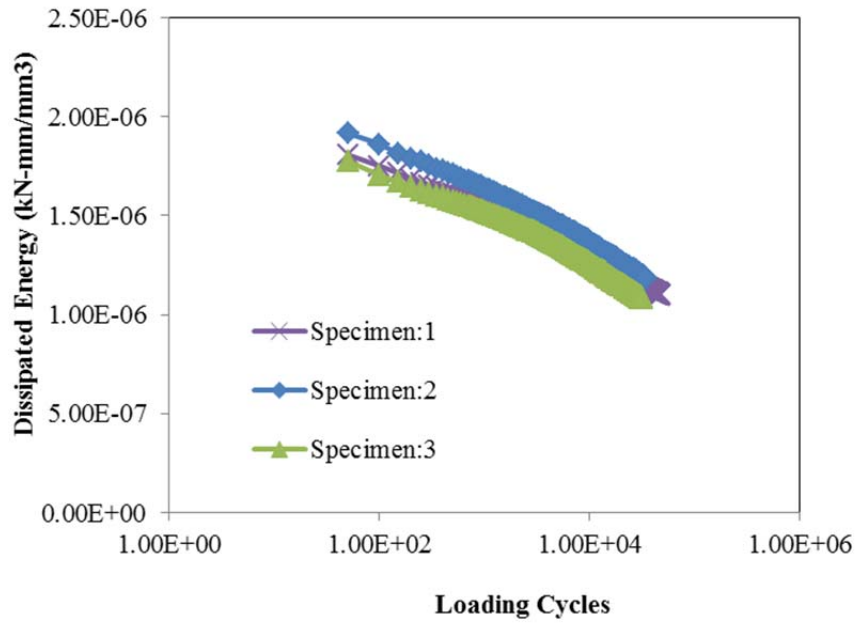
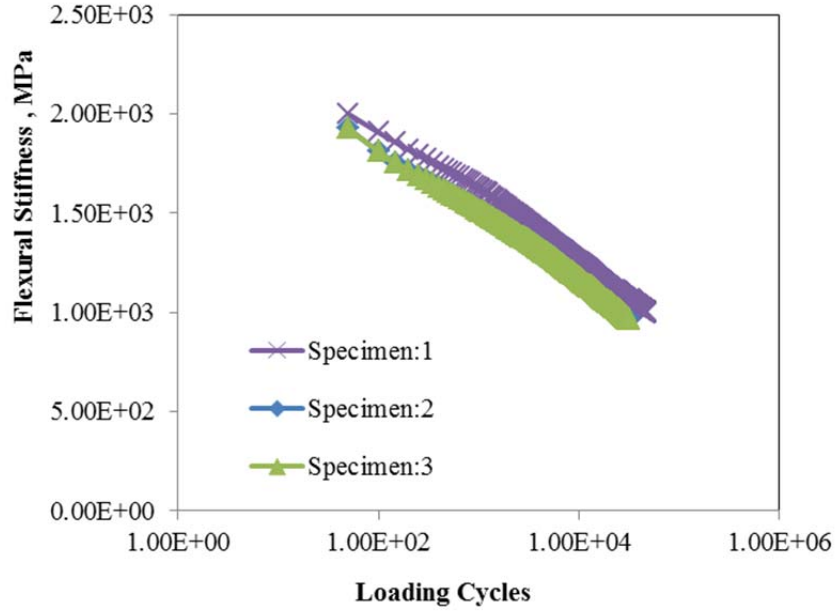


Figure A7 Fatigue test results: SP12.5FC2 64-28 D (opt.)

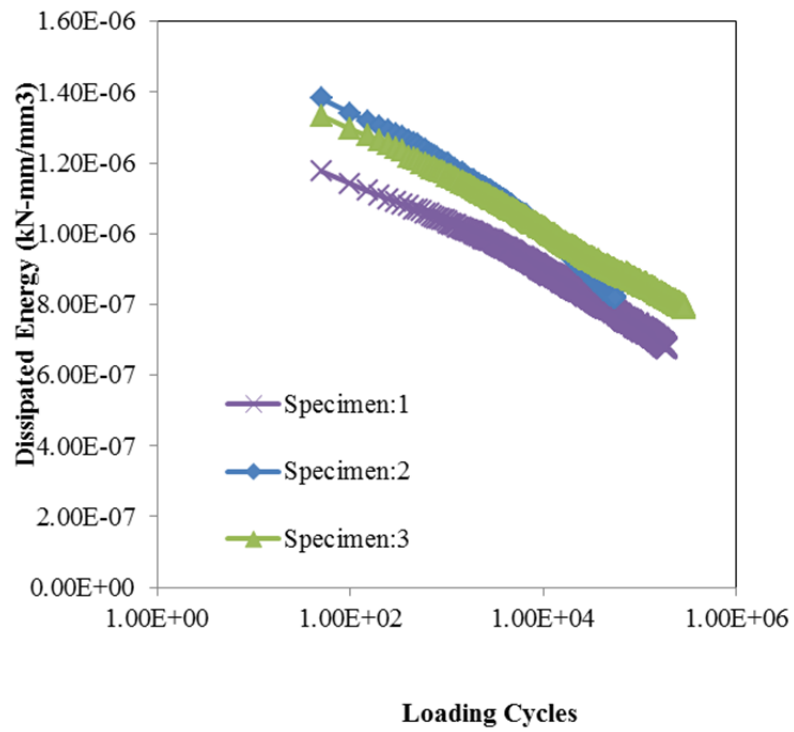
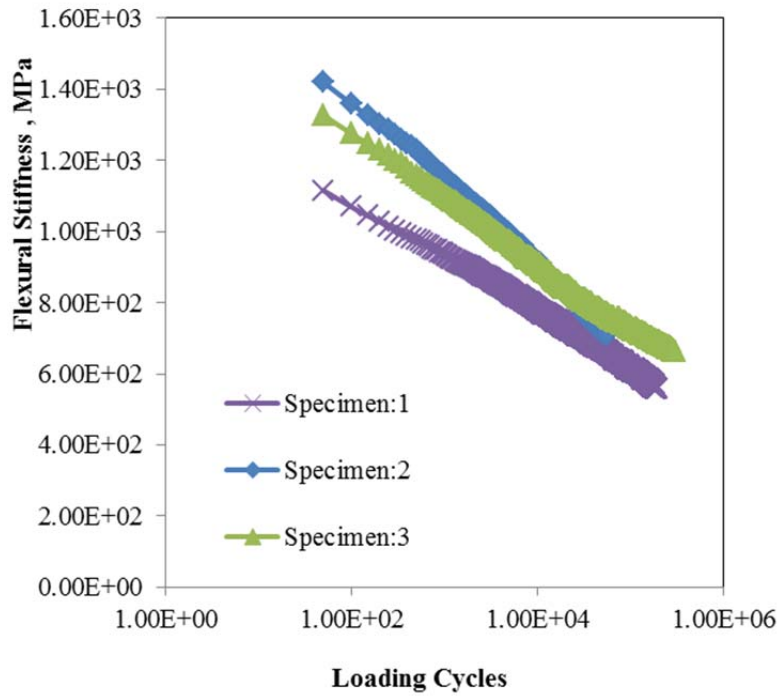
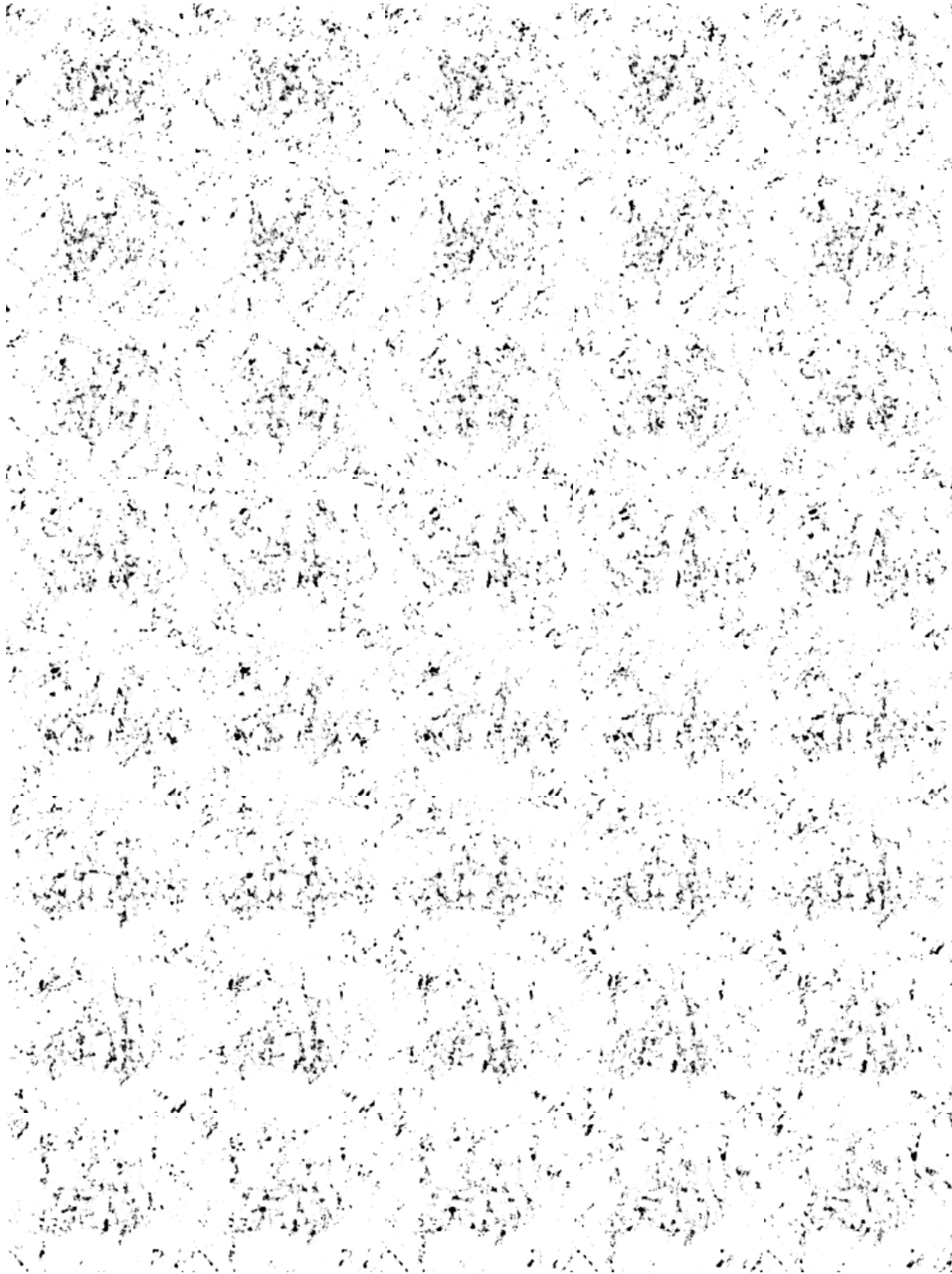


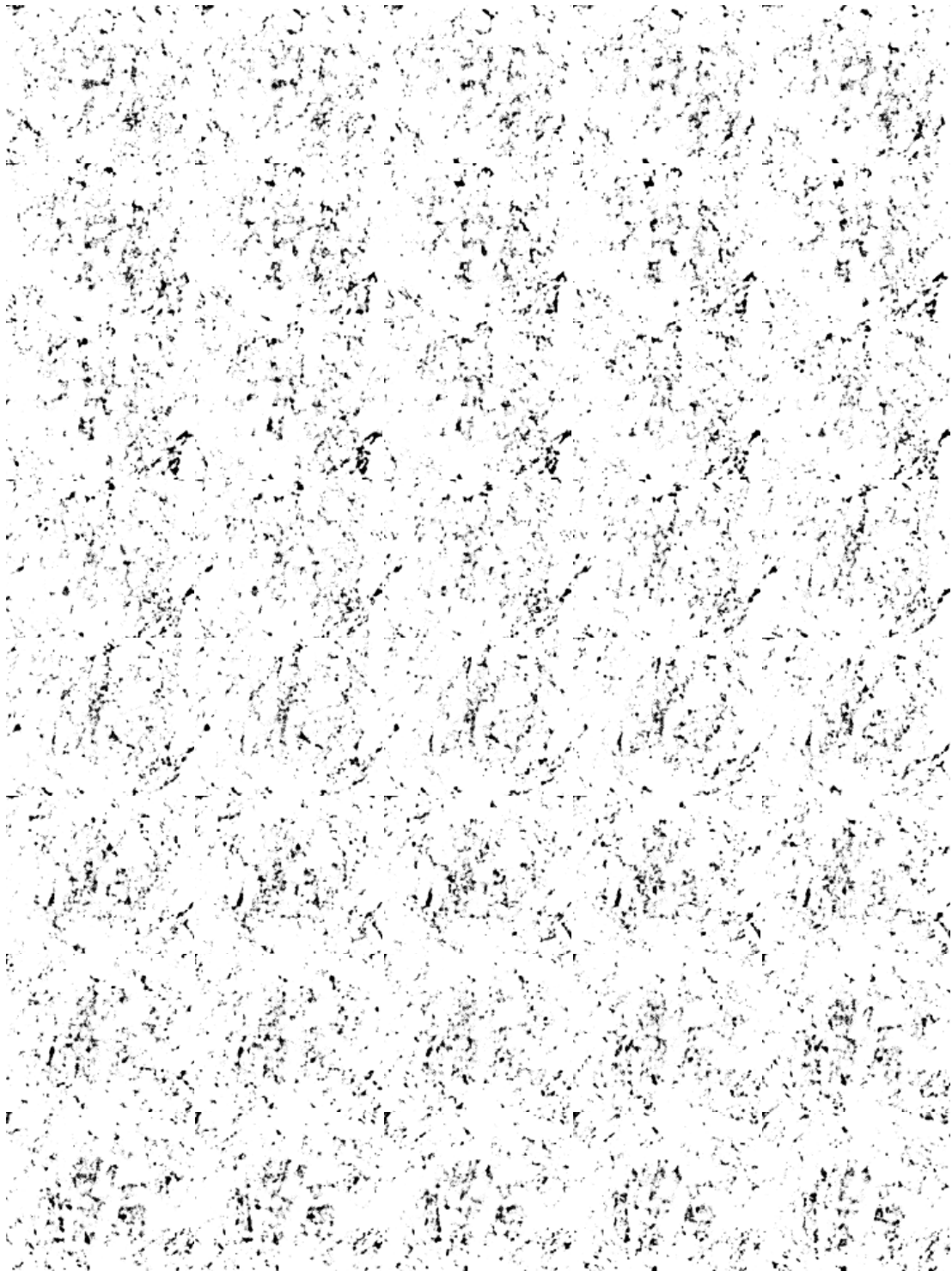
Figure A8 Fatigue test results: SP12.5FC2 64-28 D (opt.+0.5)

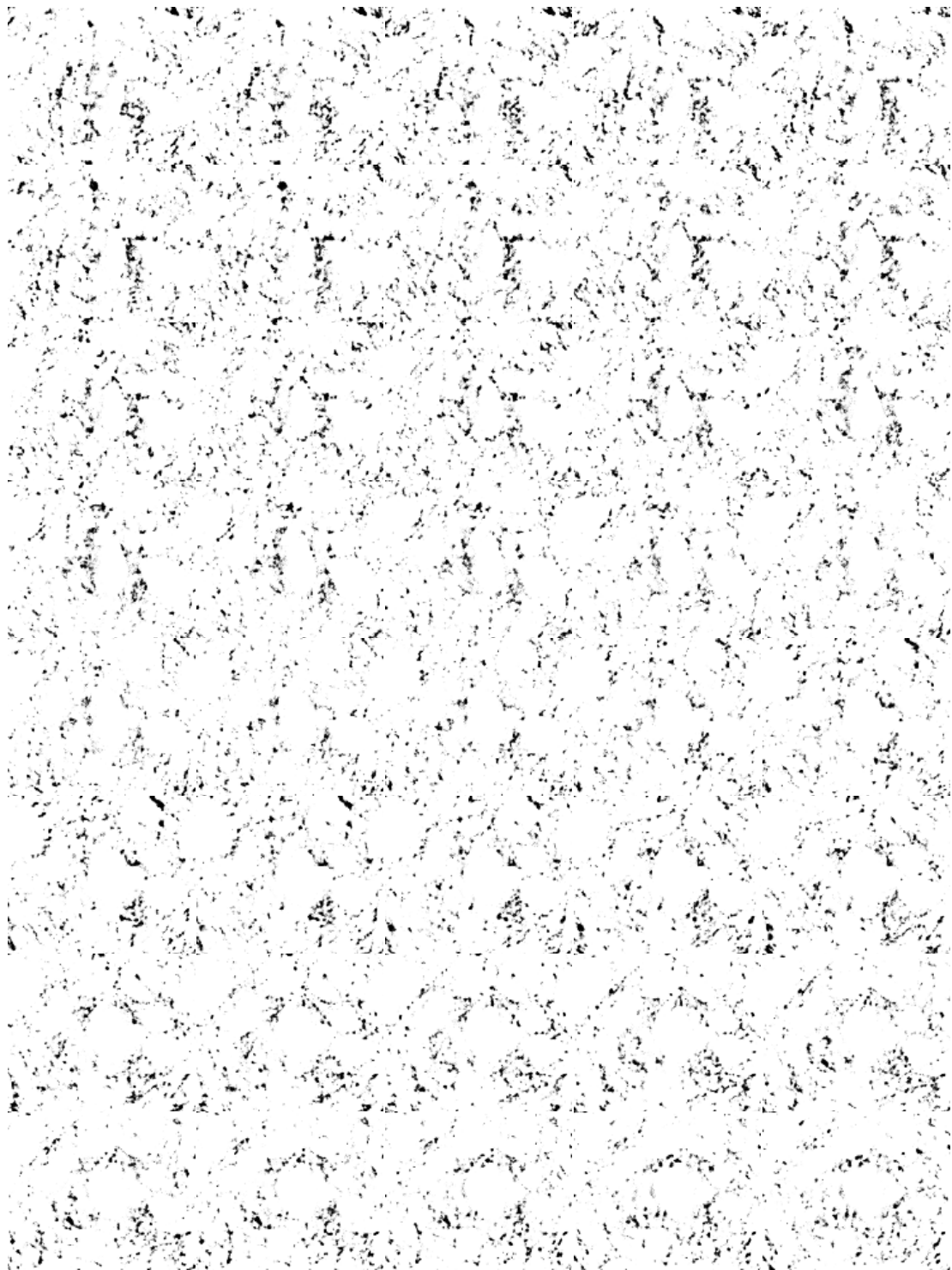
Appendix B: Image-Based Analysis

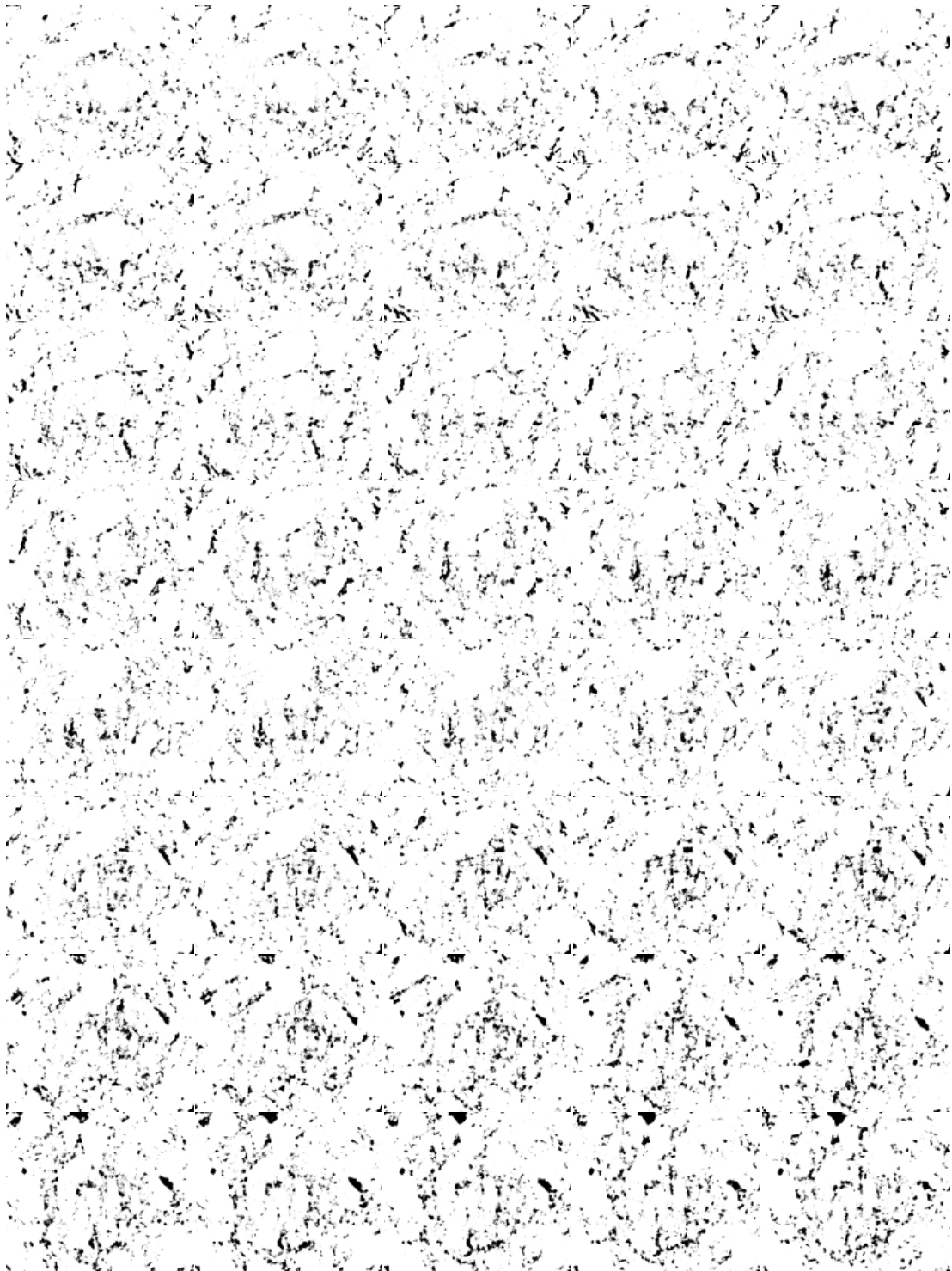
Example of air voids images for cross sections of asphalt beams

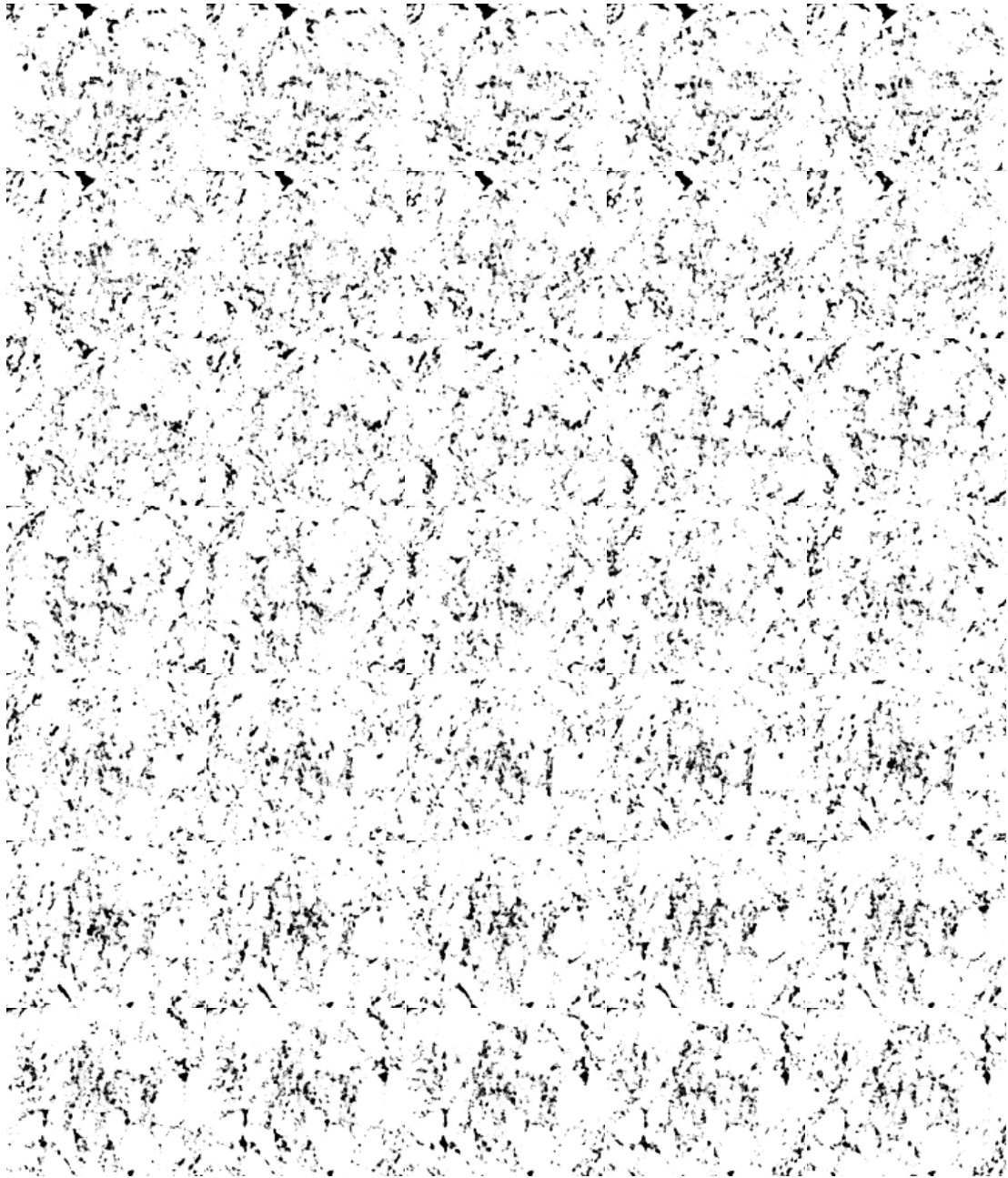












Appendix C: Microstructural FE Modeling

